



Scientific  
Research

# Smart Grid and Renewable Energy

ISSN: 2151-481X Vol.1, No.1, May 2010

ISSN: 2151-481X



[www.scirp.org/journal/sgre](http://www.scirp.org/journal/sgre)

# Journal Editorial Board

ISSN Print: 2151-481X ISSN Online: 2151-4844

<http://www.scirp.org/journal/sgre>

---

## Editors-in-Chief

**Prof. Yuanzhang Sun**  
**Prof. Victor Sreeram**

Wuhan University, China  
University of Western Australia, Australia

## Editorial Advisory Board

**Prof. Qingquan Chen**  
**Dr. Yusheng Xue**  
**Prof. Ryuichi Yokoyama**  
**Dr. Xiaoxin Zhou**

University of Hong Kong, China  
State Power Corporation, China  
Tokyo Metropolitan University, Japan  
Chinese Society of Electrical Engineering, China

## Editorial Board

**Dr. Cheung Kwai Chung**  
**Prof. Ho Chang**  
**Prof. Volkmar Dierolf**  
**Prof. Kalyanmoy Deb**  
**Prof. Igor Yu. Denisyuk**  
**Dr. Daniel Garraín**  
**Dr. Gholam Hossein**  
**Dr. Seongsoo Hong**  
**Dr. Katerina Ioakeimidi**  
**Dr. Herbert Iu**  
**Prof. David Keyson**  
**Dr. Ruomei Li**  
**Prof. Chunxiang Li**  
**Dr. Kaipei Liu**  
**Dr. Junyong Liu**  
**Prof. Jaekeun Lee**  
**Prof. Maode Ma**  
**Prof. Bouzid Mena**  
**Prof. Satyesh Chandra Roy**  
**Dr. Pierluigi Siano**  
**Dr. Peter Simon Sapaty**  
**Prof. Igor I. Strakovsky**  
**Dr. Yang Shi**  
**Prof. Huiming Wee**  
**Prof. Daniele De Wrachien**  
**Prof. Bingru Yang**  
**Dr. Fuqian Yang**  
**Prof. Changhui Ye**

Hong Kong Baptist University, China  
National Taipei University of Technology, China  
Lehigh University, USA  
Indian Institute of Technology, India  
Saint-Petersburg State University of Information Technologies, Russia  
Spanish Ministry of Science and Innovation, Spain  
Research Institute for Astronomy and Astrophysics of Maragha, Iran  
Seoul National University, Korea (South)  
Stanford University, USA  
The University of Western Australia, Australia  
Delft University of Technology, Netherlands  
Chinese Society for Electrical Engineering, China  
Shanghai University, China  
Wuhan University, China  
Sichuan University, China  
Pusan National University, Korea (South)  
Nanyang Technological University, Singapore  
Fluorotronics, Inc., USA  
Calcutta University, India  
University of Salerno, Italy  
National Academy of Sciences of Ukraine, Ukraine  
The George Washington University, USA  
University of Victoria, Australia  
Chung Yuan Christian University, Taiwan (China)  
State University of Milan, Italy  
University of Science and Technology Beijing, China  
University of Kentucky, USA  
Chinese Academy of Sciences, China

---

## Editorial Assistant

**Tian Huang**

Scientific Research Publishing, USA. Email: [sgre@scirp.org](mailto:sgre@scirp.org)

## TABLE OF CONTENTS

**Volume 1    Number 1**

**May 2010**

<b>Design of a Photo-Voltaic System to Enhance Network Dynamic Stability</b> G. J. Li, Y. Z. Sun, Q. Wang, S. S. Choi, S. Y. Ruan.....	1
<b>Control System Design of CSI Applied in the Battery Pack Testing System</b> L. X. Zhang, W. Kang, R. G. Wang.....	7
<b>Performance Analysis of Low Head Hydraulic Air Compressor</b> W. A. Aissa, S. Abdel-Hady, K. A. Ahmed.....	15
<b>Modeling of Work of Filling Granular Filter with Active Cooling</b> A. D. Rychkov.....	25
<b>Green Environment: Decision-Making and Power Utility Optimization towards Smart-Grid Options</b> D. DeGroff.....	32
<b>A Qualitative Perpective on Idempotency Defect of Two Level System Interacting with Laser and Quantized Field</b> S. Abdel-Khalek, M. M. A. Ahmed, W. N. A. Razek, A. S. F. Obada.....	40
<b>Critical Factors that Affecting Efficiency of Solar Cells</b> F. Dinçer, M. Emin Meral.....	47
<b>Development and Installation of High Pressure Boilers for Co-Generation Plant in Sugar Industries</b> K. S. Venkatesh, A. S. Roy.....	51
<b>A MPCC-NLP Approach for an Electric Power Market Problem</b> H. S. Rodrigues, M. T. T. Monteiro, I. Vaz.....	54

# Smart Grid and Renewable Energy (SGRE)

## Journal Information

### SUBSCRIPTIONS

The *Smart Grid and Renewable Energy* (Online at Scientific Research Publishing, [www.SciRP.org](http://www.SciRP.org)) is published quarterly by Scientific Research Publishing, Inc., USA.

#### Subscription rates:

Print: \$50 per issue.

To subscribe, please contact Journals Subscriptions Department, E-mail: [sub@scirp.org](mailto:sub@scirp.org)

### SERVICES

#### Advertisements

Advertisement Sales Department, E-mail: [service@scirp.org](mailto:service@scirp.org)

#### Reprints (minimum quantity 100 copies)

Reprints Co-ordinator, Scientific Research Publishing, Inc., USA.

E-mail: [sub@scirp.org](mailto:sub@scirp.org)

### COPYRIGHT

Copyright©2010 Scientific Research Publishing, Inc.

All Rights Reserved. No part of this publication may be reproduced, stored in a retrieval system, or transmitted, in any form or by any means, electronic, mechanical, photocopying, recording, scanning or otherwise, except as described below, without the permission in writing of the Publisher.

Copying of articles is not permitted except for personal and internal use, to the extent permitted by national copyright law, or under the terms of a license issued by the national Reproduction Rights Organization.

Requests for permission for other kinds of copying, such as copying for general distribution, for advertising or promotional purposes, for creating new collective works or for resale, and other enquiries should be addressed to the Publisher.

Statements and opinions expressed in the articles and communications are those of the individual contributors and not the statements and opinion of Scientific Research Publishing, Inc. We assume no responsibility or liability for any damage or injury to persons or property arising out of the use of any materials, instructions, methods or ideas contained herein. We expressly disclaim any implied warranties of merchantability or fitness for a particular purpose. If expert assistance is required, the services of a competent professional person should be sought.

### PRODUCTION INFORMATION

For manuscripts that have been accepted for publication, please contact:

E-mail: [sgre@scirp.org](mailto:sgre@scirp.org)

# Design of a Photo-Voltaic System to Enhance Network Dynamic Stability\*

Guojie Li<sup>1</sup>, Yuanzhang Sun<sup>2</sup>, Qi Wang<sup>3</sup>, San-Shing Choi<sup>4</sup>, Si-Ye Ruan<sup>5</sup>

<sup>1</sup>Department of Electrical Engineering, Shanghai Jiao Tong University, Shanghai, China; <sup>2</sup>The School of Electrical Engineering, Wuhan University, Wuhan, China; <sup>3</sup>Power System Department, China Electrical Power Research Institute, Beijing, China; <sup>4</sup>School of Electrical and Electronic Engineering, Nanyang Technological University, Singapore; <sup>5</sup>State Grid Operation Company Ltd, Beijing, China.

Email: [liguojie2000@126.com](mailto:liguojie2000@126.com), [wangqi@epri.ac.cn](mailto:wangqi@epri.ac.cn), [ESSCHOI@ntu.edu.sg](mailto:ESSCHOI@ntu.edu.sg)

Received April 26<sup>th</sup>, 2010; revised May 6<sup>th</sup>, 2010; accepted May 7<sup>th</sup>, 2010.

## ABSTRACT

*Due to the increasing amount of photovoltaic (PV)-based power generation being connected to power systems, issues pertaining to the integration of the PV-based generators have attracted intense attention. In this connection, the design of a PV-based stabilizer for enhancing power system dynamic stability is examined. The damping action is achieved through the independent control of real power flow from the stabilizer and voltage at the point of common coupling between the stabilizer and grid system. The stabilizer system is designed based on classical frequency response technique. Robustness of the proposed control strategy in enhancing network dynamic stability is demonstrated through computer simulation.*

**Keywords:** PV Damping System, Power Oscillations, Damping Ratio

## 1. Introduction

Due to the increasing energy consumption, diminishing fossil fuel-based energy reserve and the concern for the environment, development for renewable energy sources has progressed at ever greater pace in recent years. In this regard, harnessing the energy from the sun using photo-voltaic (PV) system has received much support [1,2]. Normally, the PV generation system operates under the maximum power point tracking (MPPT) mode so as to extract the maximum amount of energy from the sun [3-8]. Unfortunately, thus far the relatively high cost of the PV generation system has acted as a barrier to large-scale application of the renewable technology. In order to enhance the attractiveness of PV system, one possible way would be to extent its functionality so that it can be used to serve additional utility functions.

In pursuing this possibility, one notes that a most fundamental challenge to power system control is to suppress undesirable system oscillations initiated (for example) due to some network switching actions. The scale of the oscillating power component is often small initially, compared to the level of the transferred power. However, if no appropri-

ate control action is taken, the undamped oscillations can endanger the operation of the network. Networks which contain weakly coupled transmission links operating under heavy load transfer conditions are particularly prone to this type of problem [9-12]. In this regard, the proposed PV system to be considered in this paper is intended for providing the ability to enhance network dynamic stability. It will be shown through detailed analysis that the inverter within the PV-based stabilizer system can exercise independent real and reactive power flow controls which will lead to enhanced system damping.

The paper is organized in the following manner. In Section 2, a description of the PV damping system is given. The analysis of the PV damping action is described and the design of the control system shown in Section 3. Digital simulation results, based on PSCAD/EMTDC, are presented in Section 4 to illustrate the efficacy of the scheme.

## 2. Description of the PV Damping System

Similar in structure to the conventional photo-voltaic generator as described in e.g. [5,6], the main hardware components of the PV-based stabilizer system includes the PV panel, inverter system, filtering reactor, and step-up transformer for grid connection. The schematic of the PV-based grid-connected stabilizer system is shown in **Figure 1**. The PV panel converts the harnessed solar

\*This work was supported in part by National Natural Science Foundation of China under Grant 50977050 and 50823001 and BP Alternative Energy Ltd.

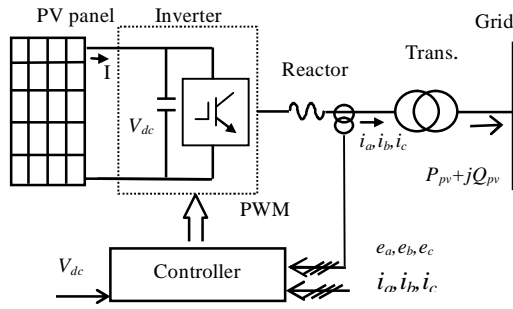


**Figure 1. Schematic of the PV-based grid-connected stabilizer system**

energy directly to electrical power and the outputs DC voltage  $V_{dc}$  is converted to AC voltage through the inverter system. The inverter system consists of fast switching IGBT, usually operating under PWM scheme. The switching pattern of the PWM is governed by a controller acting on the input three-phase AC voltages  $e_a, e_b, e_c$  and currents  $i_a, i_b, i_c$ , as shown in the figure.

The inverter of the PV damping system acts as a voltage source converter (VSC). As in a standard VSC, by adjusting its modulation index and the phase of the VSC terminal voltage with respect to the grid-side voltages, real and reactive power outputs of the VSC can be independently controlled [13,14].

The typical V/I characteristics of a solar cell and that relating its output power  $P_{PV}$  with  $V_{dc}$  are as shown in **Figure 2** [3,4,6]. The figure shows that there is a maximum output power ( $P_{pvmax}$ ) operating point. Based on the  $P_{PV} - V_{dc}$  characteristics, it will be necessary to operate the PV damper with its output voltage  $V_{dc}$  within the range  $V_m \sim V_{oc}$ . In this way,  $V_{dc}$  will then undergo a much smaller change when the PV output power  $P_{PV}$  changes. This is necessary as the PWM converter can only operate effectively within a limited  $V_{dc}$  range. The capacitor shown in **Figure 1** and connected across the DC-link acts as an energy storage device so that the voltage  $V_{dc}$  can be maintained the range. Furthermore, when the PV damper acts to suppress network oscillations, the excursions in  $P_{PV}$  would be equally likely to move to either side of its steady state value. Hence, it is proposed that the PV damper is to operate with its steady-state  $V_{dc}$  set to produce an output power  $P_{pv0} = 0.5P_{pvmax}$ . In this manner, while  $P_{pv0}$  is only at half of the maximum possible, this operating state is nevertheless accompanied by an attractive  $P_{PV}$  swing range which can be used to advantage in enhancing network stability, as will be shown next.

### 3. Analysis of the PV Damping Action

The damping characteristics offered by the PV system can be illustrated using the classical lossless single-machine-infinite bus (SMIB) power system shown in **Figure 3**. The

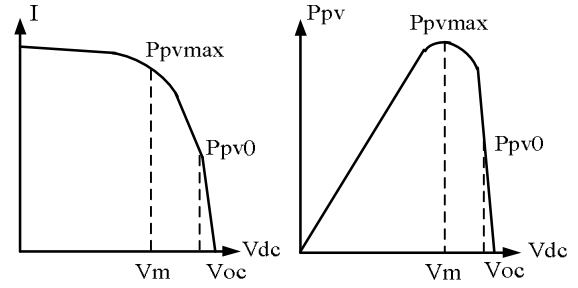


**Figure 2. Typical PV current-voltage, voltage-power characteristics and the regulated operating range of the damping system**

corresponding equivalent circuit is shown in **Figure 4**. The use of SMIB example is to facilitate analysis and to demonstrate the beneficial effects of the PV damping system, without having to resort to complicated mathematical analysis. Note that the PV is connected at an intermediate bus  $M$ , which divides the transmission link between the generator and the infinite bus into two sections. It is assumed that the PV-based stabilizer system contributes toward meeting only a small part of the load demand at the infinite bus. This is a realistic assumption as one would not expect the PV system is the major source to meet the power demand at the infinite bus. Instead, it will be more meaningful to examine how the PV system would enhance network stability, when the power system is subjected to small disturbances. The stabilization function is thus an additional benefit that can be extracted from the PV system.

In **Figure 4**,  $\delta$  denotes the rotor angle of the generator with respect to the infinite bus, and  $E'_q$  represents the generator EMF behind the machine transient  $d$ -axis reactance  $x'_d$ . Hence  $x_l$  would be the sum of  $x'_d$  and the line reactance between the generator terminal and bus  $M$ .  $\phi$  is the phase difference between bus  $M$  voltage  $V_m$  and that of  $E'_q$ .  $P_e + jQ_e$ ,  $P_{pv} + jQ_{pv}$  and  $P_s + jQ_s$  are the respective real and reactive power flows at the generator, PV and infinite-bus terminals. The PV-based stabilizer is represented by the inverter which has the output voltage  $v_s \angle (\delta - j + \beta)$ .  $V_s$  is the voltage of the infinite system bus.

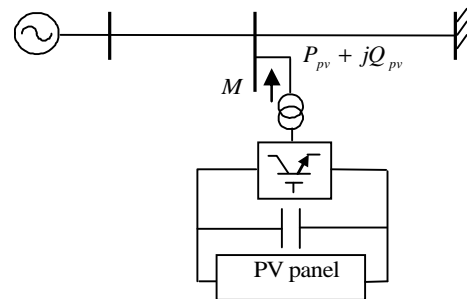


**Figure 3. A SMIB system incorporated with a PV damping system**

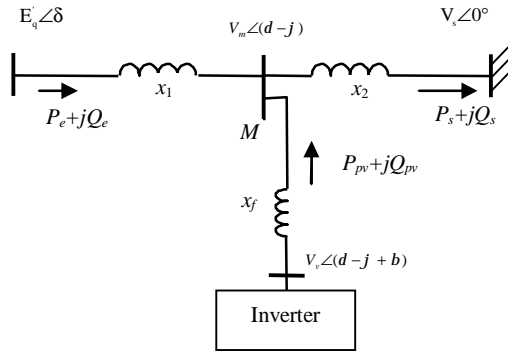


**Figure 4. Equivalent circuit of the SMIB system with the PV-based stabilizer**

A simplified 2<sup>nd</sup>-order linearized model of the power system is used in which the generator excitation and governor control actions are neglected [9], viz.:

$$\frac{d}{dt}\Delta\delta = w_0\Delta w \quad (1)$$

$$\frac{d}{dt}\Delta w = \frac{1}{2H}(-K_D\Delta w - \Delta P_e) \quad (2)$$

where  $\Delta\delta$  and  $\Delta w$  denote the generator rotor angle and speed deviations respectively,  $H$  is the generator inertia constant,  $\Delta P_e$  is the deviation of the generator electrical output power,  $K_D$  is the machine damping torque coefficient and  $w_0$  is the synchronous speed. From the network equation,  $P_e$  is given by

$$P_e = \frac{E'_q V_m}{x_1} \sin f \quad (3)$$

Laplace transform (1) and (2) with the operator  $s$ , one obtains

$$s^2(\Delta d) + \frac{K_D}{2H}s(\Delta d) + \frac{w_0}{2H}\Delta P_e = 0 \quad (4)$$

Also apply power balance at bus  $M$ ,

$$\frac{E'_q V_m}{x_1} \sin f + P_{pv} = \frac{V_m V_s}{x_2} \sin(d-f) \quad (5)$$

As the focus of the analysis is on the small-signal response of the power system, one could make use of the linearized version of (3) and (5) around the nominal operating point to obtain

$$\Delta P_e = \frac{E'_q V_{m0}}{x_1} \cos f_0 \Delta f + \frac{E'_q}{x_1} \sin f_0 \Delta V_m \quad (6)$$

$$\begin{aligned} & \frac{E'_q V_{m0}}{x_1} \cos f_0 \Delta f + \frac{E'_q}{x_1} \sin f_0 \Delta V_m + \Delta P_{pv} \\ & = \frac{V_{m0} V_s}{x_2} \cos(d_0 - f_0) (\Delta d - \Delta f) + \frac{V_s}{x_2} \sin(d_0 - f_0) \Delta V_m \end{aligned} \quad (7)$$

Note that in (6) and (7), symbols with the subscript “0” denote the nominal operating states of the variables. From (6),  $\Delta\varphi$  can be expressed in terms of  $\Delta P_e$  and  $\Delta V_m$ ,

$$\Delta f = \frac{x_1}{E'_q V_{m0} \cos f_0} \Delta P_e - \frac{\sin f_0}{V_{m0} \cos f_0} \Delta V_m \quad (8)$$

Substitute (8) into (7), (7) can be rewritten into the form

$$\Delta P_e = -C_a \Delta P_{pv} + C_b \Delta V_m + C_c \Delta d \quad (9)$$

where

$$C_a = \frac{x_2 E'_q \cos f_0}{x_2 E'_q \cos f_0 + x_1 V_s \cos(d_0 - f_0)},$$

$$C_b = \frac{E'_q V_s \sin d_0}{x_2 E'_q \cos f_0 + x_1 V_s \cos(d_0 - f_0)},$$

$$C_c = \frac{V_{m0} V_s E'_q \cos f_0 \cos(d_0 - f_0)}{x_2 E'_q \cos f_0 + x_1 V_s \cos(d_0 - f_0)},$$

Equations (1),(2) and (9) can be represented by the block diagram shown in **Figure 5**. In adopting this model,  $C_a$ ,  $C_b$  and  $C_c$  are constant for a given network condition. To improve on the overall dynamic performance of the power system, the next task is to design the PI feedback control systems to achieve specified objectives through the judicious selection of parameters  $k_1$ - $k_4$ , as follows.

### 3.1 Design of the $V_m$ Feedback Controller

In terms of design procedure, one should design the  $V_m$  feedback loop first because it corresponds to the case when  $P_{pv} = 0$  (case of no solar power input). The design problem is therefore to determine the values of  $k_2$  and  $k_4$  shown in **Figure 5** such that the closed-loop system is well-damped. Firstly examine the open loop transfer function  $\Delta\delta/\Delta V_m$ . The method is based on the well-known frequency response technique. Consider the case when the  $V_m$  control loop in **Figure 5** is opened, as shown in **Figure 6**.

From **Figure 6**, the open loop transfer function of  $\Delta d$  referring to  $\Delta V_m$  is:

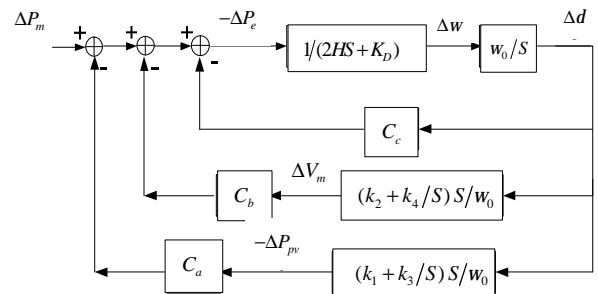


**Figure 5. The block diagram of the power system model**

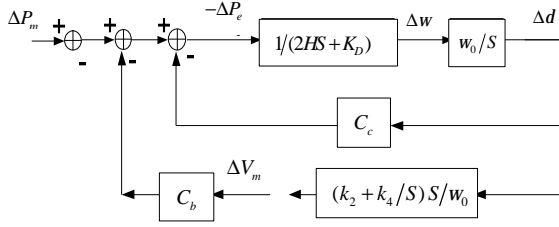


Figure 6. Open-loop transfer function  $Dd/DV_m$

$$\frac{\Delta d}{\Delta V_m} = \frac{C_b w_0}{2HS^2 + K_D S + C_c w_0} \quad (10)$$

For convenience, denote  $\Delta d/\Delta V_m$  as  $G(s)$ . According to the basic frequency response technique, after adding the  $V_m$  feedback controller, at the cross-over point  $S = j\omega_c$ , the desired system open-loop gain should be  $(k_2 + \frac{k_4}{S}) \frac{S}{w_0} G(s) = 1$  and the phase angle should be  $(-180^\circ + PM)$ , where  $PM$  is the desired phase margin at the cross-over point. Thus,

$$\left(k_2 + \frac{k_4}{S}\right) \frac{S}{w_0} M_G e^{jq_G} = 1e^{j(-180^\circ + PM)} \quad (11)$$

$M_G$  and  $\theta_G$  are the gain and phase angle of  $G(s)$  at the frequency  $\omega = \omega_c$ . Therefore (11) can be written as

$$\begin{aligned} \left(k_2 + \frac{k_4}{j\omega_c}\right) \frac{j\omega_c}{w_0} M_G (\cos q_G + j \sin q_G) \\ = \cos(-180^\circ + PM) + j \sin(-180^\circ + PM) \end{aligned}$$

Separate the last equation into its real and imaginary parts,  $k_2$  and  $k_4$  can be derived

$$k_2 = \frac{w_0 \sin(q_G - PM)}{w_c M_G}, \quad k_4 = \frac{-w_0 \cos(q_G - PM)}{M_G} \quad (12)$$

Generally, a good damping factor  $x$  of closed-loop system is 0.707, the necessary phase margin  $PM$  should be approximately  $70^\circ$ . To obtain the desired phase margin, it is usual to make the targeted phase margin a few degrees higher (say by  $5^\circ$ ). This is because the  $V_m$  feedback control introduces an additional zero to the system. The zero will make the final cross-over frequency  $w_c$  slightly higher. The recommended  $PM$  is therefore  $75^\circ$ .

Once knowing  $w_c$ ,  $M_G$  and  $q_G$ , (12) permits  $k_2$  and  $k_4$  to be readily determined.

### 3.2 Design of $P_{pv}$ Feedback Controller

Suppose the  $V_m$  feedback controller has already been designed and is in service. Consider the case when the  $P_{pv}$  control loop in Figure 5 is opened, as shown in Figure 7.

From Figure 7, the open loop transfer function of  $\Delta d$

referring to  $-\Delta P_{pv}$  is:

$$\frac{\Delta d}{-\Delta P_{pv}} = \frac{C_a w_0}{2HS^2 + (K_D + C_b k_2)S + C_c w_0 + C_b k_4} \quad (13)$$

For convenience, denote  $\Delta d/(-\Delta P_{pv})$  as  $G'(s)$ . Using the same reasoning as before, after adding the  $P_{pv}$  feedback controller and at the cross-over point  $S = jw'_c$ , the desired system open-loop gain should be  $(k_1 + \frac{k_3}{S}) \frac{S}{w'_0}$

$G'(s) = 1$  and the phase angle should be  $(-180^\circ + PM)$  where  $PM$  is the desired phase margin at the cross-over point. Thus,

$$\left(k_1 + \frac{k_3}{S}\right) \frac{S}{w'_0} M'_G e^{jq'_G} = 1e^{j(-180^\circ + PM)} \quad (14)$$

$M'_G$  and  $q'_G$  are the gain and phase angle of  $G'(s)$  at the point  $w = w'_c$ . Separate the above equation into its real and imaginary parts,  $k_1$  and  $k_3$  can be derived

$$k_1 = \frac{w'_0 \sin(q'_G - PM)}{w'_c M'_G}, \quad k_3 = \frac{-w'_0 \cos(q'_G - PM)}{M'_G} \quad (15)$$

Based on similar design consideration as that in Subsection 3.1, with known  $w'_c$ ,  $M'_G$  and  $q'_G$ , (15) permits  $k_1$  and  $k_3$  to be evaluated.

## 4. Illustrative Examples: Response under Small Disturbances

In order to assess the controller design shown in the previous section, simulation studies have been carried out.

Extensive study has been carried out using the SMIB example but in this paper, only the results of a small disturbance is simulated by introducing a 0.05 p.u. step increase of the input mechanical power of the generator at 1s will be presented. The time response will be studied under two modes: 1) Mode 1 corresponds to the case with only  $V_m$  feedback control loop; 2) Mode 2 represents the case with both  $V_m$  and  $P_{pv}$  feedback control loops. The study will be carried out for the following operating con-

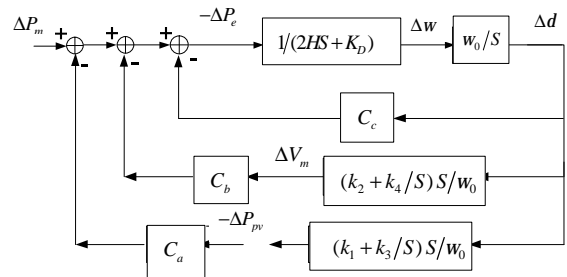
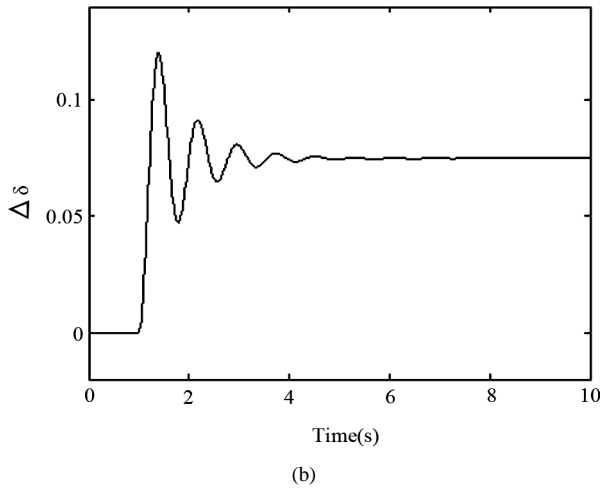
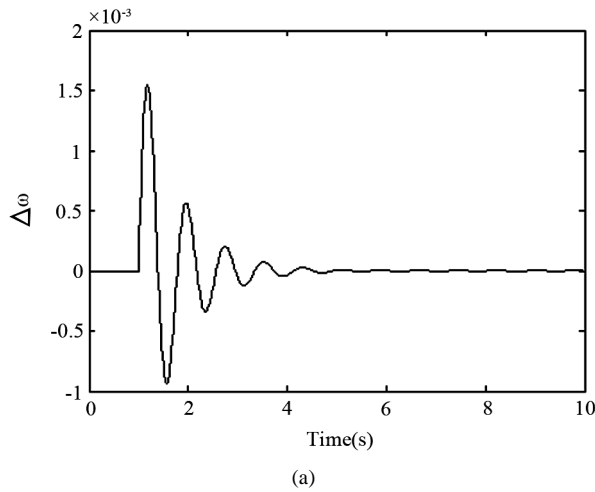


Figure 7. Open-loop transfer function  $\Delta d/(-\Delta P_{pv})$ , with  $V_m$  control loop closed



**Figure 8. Power system response following a step change of the generator mechanical power with  $V_m$  feedback control**

dition:  $P_{e0} = 0.32$  for all 2 modes.  $P_{pv0} = 0$  for mode 1  $P_{pv0} = 0.24$  for Mode 2.

Time response plots of rotor speed variation  $\Delta\omega$  and angle variation  $\Delta\delta$  following the disturbance are as shown in **Figures 8** and **9**, corresponding to the system operating under Modes 1 and 2 respectively.

From the results of **Figure 8**, it is shown that the generator rotor oscillations following the power increase disturbance have been suppressed when only  $V_m$  is controlled under Mode 1, *i.e.* via the control scheme described in Section 3 via (9). This means that the system damping is effective even when there is no sunlight, and the PV system acts as a conventional STATCOM. Oscillations are damped out even more quickly and effectively when both  $P_{pv}$  and  $V_m$  are controlled through the feedback strategies described in Section 3 via (9) (Mode 2). Thus it confirms the PV damping system with the proposed control strategy is effective in suppressing power system

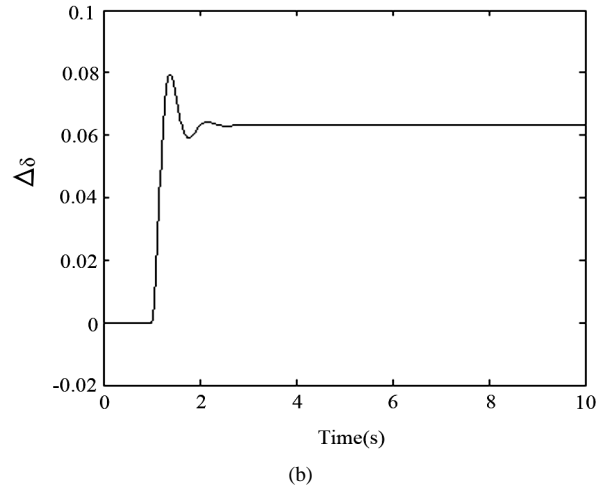
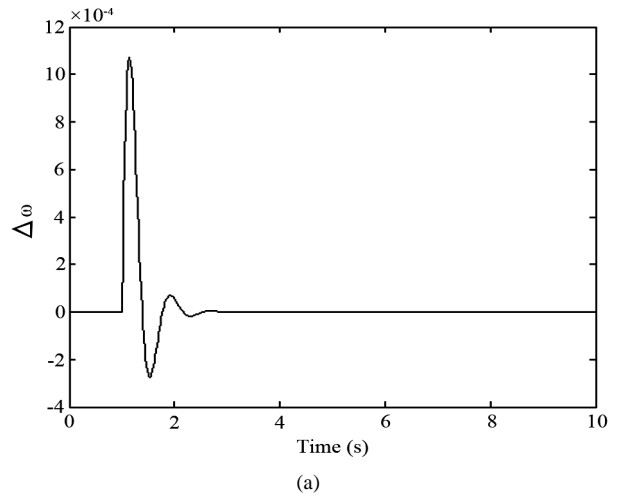


**Figure 9. Power system response following a step change of the generator mechanical power with both  $V_m$  and  $P_{pv}$  feedback control**

oscillations.

## 5. Conclusions

Unlike the conventional PV generation system which is only intended to harness energy from the sun, the proposed PV scheme has the added advantage for it is designed to provide damping control following disturbance. A theoretical analysis is provided in showing how improved damping is achieved. The proposed PV-based stabilizer system includes real power feedback and the voltage control strategy and is shown to be effective in enhancing network dynamic stability.

## REFERENCES

- [1] T. M. Razykov, "Photovoltaic Solar Electricity: State of the Art and Future Prospects," *Proceedings of 6th International Conference on Electrical Machines and Systems*, Vol. 1, 9-11 November 2003, pp. 297-301.

- [2] C. Rodriguez and G. A. J. Amaratunga, "Dynamic Maximum Power Injection Control of AC Photovoltaic Modules Using Current-Mode Control," *IEE Proceedings – Electric Power Applications*, Vol. 153, No. 1, January 2006, pp. 83-87.
- [3] M. W. Park and I. K. Yu, "A Novel Real-Time Simulation Technique of Photovoltaic Generation Systems Using RTDS," *IEEE Transactions on Energy Conversion*, Vol. 19, No. 4, March 2004, pp. 164-169.
- [4] L. Zhang, A. A. Amoudi and Y. F. Bai, "Real-Time Maximum Power Point Tracking for Grid-Connected Photovoltaic Systems," *Proceedings of IEE 8th International Conference on Power Electronics and Variable Speed Drives*, 18-19 September 2000, pp. 124-129.
- [5] U. Boke, "A Simple Model of Photovoltaic Module Electric Characteristics," *Proceedings of European Conference on Power Electronics and Applications*, 2-5 September 2007, pp. 1-8.
- [6] T. Shimizu, O. Hashimoto and G. Kimura, "A Novel High-Performance Utility-Interactive Photovoltaic Inverter System," *IEEE Transactions on Power Electronics*, Vol. 18, No. 2, March 2003, pp. 704-711.
- [7] P. Sanchis, J. López, A. Ursúa and L. Marroyo, "Electronic Controlled Device for the Analysis and Design of Photovoltaic Systems," *IEEE Power Electronics Letters*, Vol. 3, No. 2, June 2005, pp. 57-62.
- [8] T. Shimizu, M. Hirakata, T. Kamezawa *et al.*, "Generation Control Circuit for Photovoltaic Modules," *IEEE Transactions on Power Electronics*, Vol. 16, No. 3, May 2001, pp. 293-300.
- [9] P. Kundur, "Power System Stability and Control," McGraw-Hill, New York, 1994.
- [10] M. Joorabian, M. Razzaz, M. Ebadi and M. Moghaddasian, "Employing Fuzzy Logic in Damping Power System Oscillations using SVC," *Proceedings of 2nd International Conference on Electrical Engineering*, 25-26 March 2008, pp. 1-5.
- [11] M. Sedighzadeh, M. S. Toulabi, A. Rezazadeh, M. Khatibi and B. Allahverdi-Charandabi, "Damping Improvement by SSSC and STATCOM in a Part of Iran Electrical Network," *Proceedings of 43rd International Universities Power Engineering Conference*, 1-4 September 2008, pp. 1-5.
- [12] G. J. Li, T. T. Lie, G. B. Shrestha and K. L. Lo, "Implementation of Coordinated Multiple FACTS Controllers for Damping Oscillations," *International Journal of Electrical Power and Energy Systems*, Vol. 22, No. 2, February 2000, pp. 79-92.
- [13] B. R. Andersen, L. Xu, P. J. Horton and P. Cartwright, "Topologies for VSC Transmission," *Power Engineering Journal*, Vol. 16, June 2002, pp. 142-150.
- [14] Y. Jiang-Hafner, H. Duchon, K. Linden, *et al.*, "Improvement of Sub-Synchronous Torsional Damping Using VSC HVDC," *International Conference on Power System Technology 2002 Proceedings*, Kunming, Vol. 2, October 2002, pp. 998-1003.

# Control System Design of CSI Applied in the Battery Pack Testing System

Lixia Zhang<sup>1</sup>, Wei Kang<sup>1</sup>, Rugang Wang<sup>2</sup>

<sup>1</sup>College of Information and Control Engineering, China University of Petroleum (UPC), Dongying, China; <sup>2</sup>Shenzhen Pite Electric Power and Electronics Company, Shenzhen, China.  
Email: hdzlx@163.com, zhanglixiaa@hotmail.com

Received April 22<sup>th</sup>, 2010; revised May 9<sup>th</sup>, 2010; accepted May 11<sup>th</sup>, 2010.

## ABSTRACT

*This paper designed the loop-locked SVPWM control system of current source inverter (CSI) in the battery pack charging/discharging system. The battery pack is sensitive to the charging/discharging current ripple and orders the current possess fast transform speed. Because the battery pack has tiny inner resistance, back electromotive force and it acted as a comparative load. This made the system hard to design. The control system aimed at the specialty of the battery pack load and put forward a loop-locked control method based on dq coordinate conversion in SVPWM converters. It increases the transform efficiency by SVPWM and gets high power factor and high dynamic response quality by dq coordinate conversion.*

**Keywords:** CSI, SVPWM, Dq Coordinate Conversion, Battery Charging, Battery Discharging

## 1. Introduction

When the battery pack is tested, it needed to be charged and discharged by its testing system converters. There are special requirements to the converter when the battery pack is tested. First, the battery pack is a sensitive load to the converters. When it is charged/discharged, it requires the converter of its testing system to output low-ripple current which has fast response speed. Second, the power grid ordered the converter to be a green grid that validates the properties of high power factor and high conversion efficiency [1,2].

But the inner resistance of the battery pack is very small and it has back electromotive force, when the converter's output voltage is applied on the battery pack, even if the voltage has very little ripples, the current through the battery will be large. Researches showed that both the phased-inverter and the PWM inverter have the problem of outstand current ripple when they are used in battery pack testing [3]. In order to output the regular testing current, traditional way is to use linear regulator converter [4]. But the linear regulator has many disadvantages, such as the low power factor, large power cost *et al.* With the development of battery's pack-making technique and its specific energy, the battery testing system is requested to be of high-capacity. Traditional linear regulator mode system can't satisfy the request of the convert-technique.

This paper bring forward a current source PWM con-

verter structure which suits for charging/discharging of battery pack, demonstrating the control strategy of current source PWM converter based on dq transformation. It can satisfy the request that the battery pack testing ask for convert technology.

## 2. Converter Structure and Work Theory

For a long time, the study on CSI is much more less than the voltage source inverter (VSI). Most important reasons are that the circuit structure needs big inductance for energy storage and control mode of CSI is more complexity. But when we test the battery pack, converter's output voltage is demanded to accommodate the battery pack in a range of  $0-U_N$ , the voltage source PWM rectifier can offer a fixed DC voltage which is higher than the voltage of power grid. In some conditions that request output DC voltage be lower than power supply, we need a Buck-typed circuit. Or else it's difficult to realize the design of rectifier [5]. CSI offers a steady DC current. Its voltage can be lower than the voltage of power grid. It also has rapid dynamic response when used as DC power, and is convenient for running in four quadrants [6]. It shows that the CSI is more suitable to the design of the rectifier in the battery pack testing system than voltage source PWM rectifier.

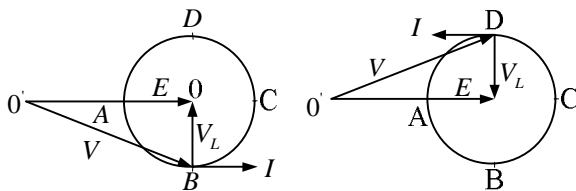
According to steady vector connection of AC side of voltage source PWM rectifier, if battery is charged through

rectifier, the power grid voltage is parallel to the current vector and reverse. At this time, power grid side of rectifier show a negative resistance, power grid absorb positive power, realize the high power factor of battery power to feedback to network [7], (see **Figure 1.**) The CSI can change the output voltage polarity, but can't change the flow direction of output current. So it can't discharge battery directly through changing the direction of current as voltage source PWM rectifier does. From the above, this paper brings forward a current source PWM converter structure which suits to charge/discharge battery pack, such as **Figure 2.**  $CT_1 \sim CT_4$  are thyristors which are used to realize the battery polarity conversion between charging and discharging. In this way, when the battery pack is tested, the double-flow of energy is realized. When dictate current of space current vector and voltage of AC side are in-phase, PWM rectifier is in state of rectification,  $CT_1$  and  $CT_4$  are cut over and the battery are charged. When dictated current of space current vector and voltage of alternating side are in reverse phase, PWM rectifier is in state of active conversion,  $CT_1$  and  $CT_3$  conduction are cut over and the battery are discharged. In this time, current and voltage of alternating side of convertor are in reverse phase, network absorb positive power, battery power is feedback to network of high power factor.

Conventional current space vector distribution is showed in **Figure 3.**

The three phase current space vector can be described as

$$I_k = \begin{cases} \frac{2}{\sqrt{3}} i_{dc} e^{j(\frac{kp}{3} - \frac{p}{6})} & (k=1 \sim 6) \\ 0 & (k=7,8,9) \end{cases}$$



(a) operate as positive impedance; (b) operate as negative impedance

**Figure 1. PWM converter stable vector relation of AC side**

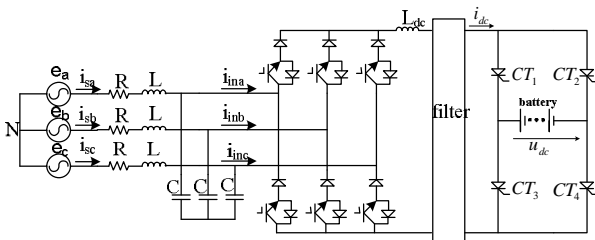


**Figure 2. Converter topology of battery pack testing system**

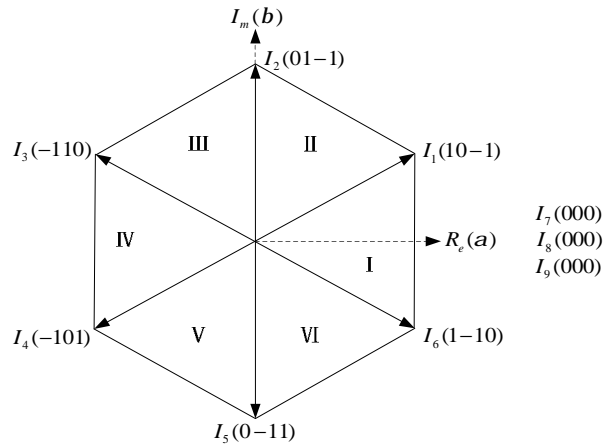


**Figure 3. Current space vector distribution**

Three phase CSI current space vector modulation equate the composite vector to reference current by appropriate current space vector  $I_k$  ( $k = 1 \sim 9$ ). All of the reference current  $I^*$  in arbitrary sector can be composed by current space vector on the side of the sector.

### 3. Design of Control System

The primary control purpose of the battery pack testing system is that: first, regulate current of DC side to fix the tracking parameter; second, gain a demanded power factor and low harmonic content current. Indirect control arithmetic rely on the parameter of CSI main circuit, once the parameter change, the control performance of the current of AC side must be influenced. Direct control of the three-phase CSI current of AC side is through network side current's track trajectory closed loop control. Then operate the alternating current input dictation current number and bring in alternating current feed back to follow dictation current through direct control of alternating current. As the closed loop control also have a suppression to the disturbance in the control loop, to the in DC control, current control of alternating side improved the function of dynamic state and static state by using DC control.

This paper used DC control method which based on the three-phase SCR three-valued logic PWM control. PWM rectifier adopts the SVPWM control mode, because it have a high current efficiency and fast response. Main circle and control structure which based on dq coordinate conversion to SVPWM converters in the battery pack testing system as **Figure 4.**

The outer loop is DC current control loop. The output  $i_q^*$  of outer control loop is positive current dictate of inner loop. The meaning of  $i'_a, i'_b, i'_c$  is the Per Unit System of AC side. Current  $i_a, i_b, i_c$  which is in three-phase staticsymmetric coordinate system. If we take abc-dq0

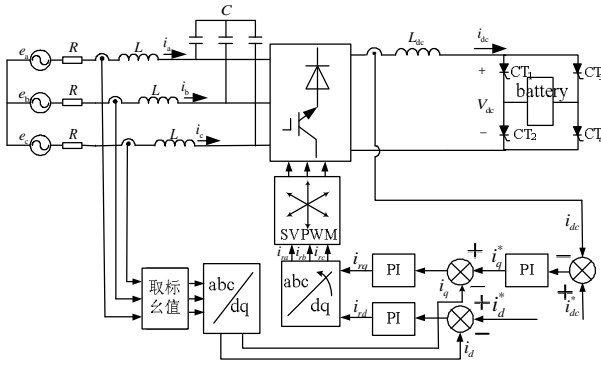


**Figure 4. Control structure of current source PWM converter for the battery pack testing system**

transform to them, we gain the  $i_d'$  and  $i_a'$  in synchronous revolution coordinate system. Comparing the  $i_d'$  to reactive power component dictate  $i_d^*$ ,  $i_q'$  to active power component, we will gain the active power component and reactive power component dictate through regulator.

When rectifier worked in a unit power factor, the reactive power component dictate is zero, active power component output by outer control loop. The order of outer control loop is to fix the DC side current  $i_{dc}$ . The order of inner control loop is to ask the current  $i_d$  and  $i_q$  to keep up with  $i_d^*$  and  $i_q^*$  and to realize the unit power factor and low harmonic current control.

Now we research the structure of three-phase CSI main circuit, for short, we take one phase for example, circuit structure is showed in **Figure 4** [8,9].

According the literature [5], we know network side current is formed of two part, one is response to power grid voltage  $E_s(s)$ , the other is response to AC side current. Commonly, PWM equipment can be seen as a self-tuning one-order inertial segment.  $W_{PWM}(s) \approx$

$\frac{K_{PWM}}{T_{PWM}s + 1}$ , when  $T_s$  is small enough, i.e.  $T_s w \ll 1$ , the

PWM equipment can be seen as a proportional component that gain is  $K_{PWM}$ .

When the switch frequency is outclass the fundamental wave frequency in single-phase CSI network, neglect the harmonic in AC side current  $I_t(s)$ . only take fundamental wave into account. System transfer function

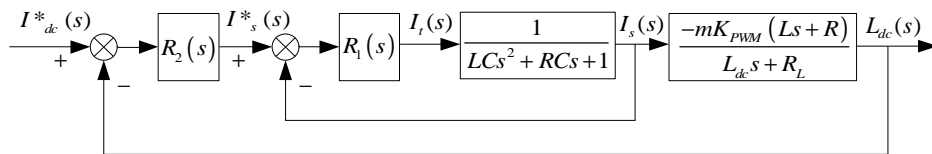


**Figure 6. Simplified system two-ring deliver fabric**

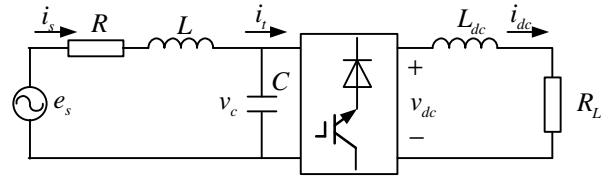


**Figure 5. Single-phase CSI circuit transfer structure**

is single-variable input and single-variable output. When the power grid voltage fixed, we can neglect the influence that it's ripple produced to the control system. The simplified system two-ring deliver fabric is showed in **Figure 6**.

### 3.1 The Design of Current Inner Control Loop

For the three-phase CSI control system, consider the relation between the variable of single-phase. From **Figure 4**, because there are two energy store element  $L$ ,  $C$ , the inherent transfer function of the inner loop is [10,11]:

$$W_1(s) = \frac{1}{LCs^2 + RCs + 1} = \frac{1}{(t_1s + 1)(t_2s + 1)} \quad (1)$$

So the inherent transfer function of the inner loop is a 2-order system. The damping ratio  $x$  and oscillating angular frequency  $w_n$  are,

$$x = \frac{R}{2} \sqrt{\frac{C}{L}} \quad (2)$$

$$w_n = \sqrt{\frac{1}{LC}} \quad (3)$$

To design a three-phase CSI control system, first consider one phase. As there are two Energy-Storage component in **Figure 4**, the AC side current inner loop system's static transfer function is

$$W_1(s) = \frac{1}{LCs^2 + RCs + 1} = \frac{1}{(t_1s + 1)(t_2s + 1)} \quad (1)$$

The inner loop system's inherent transfer function is a second-order system, it's resistance ratio and oscillation angular frequency are:

$$x = \frac{R}{2} \sqrt{\frac{C}{L}} \quad (2)$$

$$w_n = \sqrt{\frac{1}{LC}} \quad (3)$$

Bring the battery's data to Formula (2), then  $0 < x < 1$ . So this 2-order system is a periodic damping system. Its two characteristic roots are,

$$\begin{aligned} s_{1,2} &= -xw_n \pm jw_n\sqrt{1-x^2} = -xw_n \pm jw_d \\ &= a + jb = Ae^{-at} \sin(bt + j_0) \end{aligned} \quad (4)$$

where  $w_d = \sqrt{1-x^2}w_n$  is the damped oscillation frequency.

where  $t$  is little,  $b$  is little, so  $\sin bt \ll w_n$ , then the imaginary part of the characteristic root can be ignored. Only consider the real part, so

$$t_{1,2} \approx \frac{RC}{2} \quad (5)$$

Then the inner loop system's inherent transfer function is simplified as

$$W_1(s) = \frac{1}{(t_1s+1)^2} \quad (t_1 = t_2 = RC/2) \quad (6)$$

In order to attain a good current follow-up control performance for current inner loop, we can set the current inner loop control system with simple model 1. Aimed at simplified inner loop control system transfer function's inherent bi-inertial sector, inner loop control  $R_1(s)$  can use PI regulator.

$$R_1(s) = W_{pi}(s) = \frac{K'_{pi}(t_{pi}s+1)}{t_{pi}s} \quad (7)$$

Then the open loop transfer function of inner current control loop is

$$W_{1o}(s) = W_{pi}(s) \cdot W_1(s) = \frac{K'_{pi}(t_{pi}s+1)}{t_{pi}s} \cdot \frac{1}{(t_1s+1)^2}$$

According to the optimal correction method set it to be a typical I system. The corrected open loop transfer function of inner current control loop is

$$W_{1o}(s) = \frac{1}{s(t_1s+1)} \quad (8)$$

The parameter of inner loop PI controller is

$$t_{pi} = K_{pi} = t_1 \quad (9)$$

The transfer function of inner loop is

$$W_{1c}(s) = \frac{1}{t_1s^2 + s + 1} \quad (10)$$

In the literature [5], the inherent transfer sector of inner loop system can be thought to inertia sector. In order to set inner loop system to 1 system, we regulate the inner loop by integrating device. But if the parameter of integrating device is big, the response will be slow; if use PI of PID

rectifier, can reduce the static deviation and have a fast response. So in this paper, we adopt the PI rectifier.

### 3.2 Design of Current Outer Loop Rectifier

According to the transfer function of the inner current loop, because the resistance  $R$  of AC side is tiny, so  $\tau_1\omega_{c2}^2 \ll 1$ . where  $\omega_{c2}$  is the stop frequency of outer current loop. The transfer function of the inner current loop can be simplified as:

$$W_{1c}(s) = \frac{1}{s+1} \quad (11)$$

when the power grid voltage is steady, the disturbance of power grid voltage  $E_s(s)$  and DC current  $E_L(s)$  can be neglected. The transfer function from  $i_s$  to  $i_{dc}$  is  $\frac{-mK_{PWM}(Ls+R)}{L_{dc}s+R_{dc}}$ , The transfer function of the inner current loop is,

$$W_{2o}(s) = R_2(s) \cdot \frac{1}{s+1} \cdot \frac{-mK_{PWM}(Ls+R)}{L_{dc}s+R_{dc}} \quad (12)$$

where  $R_2(s)$  outer current PI transfer function,  $m$  is the modulation ratio.

The outer current control system is set as a typical II system.  $R_2(s)$  is designed by PI controller, its transfer function is,

$$R_2(s) = W_{pi}(s) = \frac{K'_{pi}(\tau'_{pi}s+1)}{\tau'_{pi}s} \quad (13)$$

where  $K'_{pi}$  is the proportional gain  $\tau'_{pi}$  is the leading time constant of PI regulator

The adjusted transfer function of outer current loop is,

$$W_{2o}(s) = \frac{K'_{pi}(\tau'_{pi}s+1)}{\tau'_{pi}s} \cdot \frac{1}{s+1} \cdot \frac{-mK_{PWM}R(\frac{L}{R}s+1)}{R_{dc}(\frac{L_{dc}}{R_{dc}}s+1)} \quad (14)$$

when  $(L_{dc}/R_{dc})\omega \ll 1$ ,

$$W_{2o}(s) = \frac{K'_{pi}(\tau'_{pi}s+1)}{\tau'_{pi}s} \cdot \frac{1}{s+1} \cdot \frac{-mK_{PWM}R(\frac{L}{R}s+1)}{R_{dc}(\frac{L_{dc}}{R_{dc}}s+1)} \quad (15)$$

when  $\frac{L}{R}$  is little, simplify the system by merging little time constant. The transfer function of outer current loop is,

$$W_{2o}(s) \approx \frac{-mK_{PWM}RK'_{pi}(\tau'_{pi} + \frac{L}{R})s+1}{\tau'_{pi}L_{dc}s^2(s+1)} \quad (16)$$

Design the outer current loop by typical II system. The frequency factor  $h = 5$ , then  $h = 5$ , the transfer function of outer current loop is,

$$\begin{cases} \tau'_{pi} = 5 - \frac{L}{R} \\ K'_{pi} = -\frac{L_{dc}}{mK_{PWM}R} \left(5 - \frac{L}{R}\right) \end{cases} \quad (17)$$

#### 4. Research of Emulation

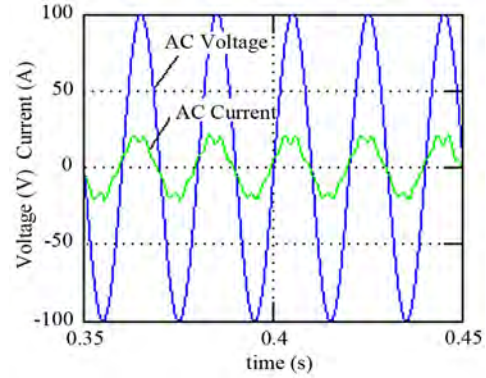
The testing system charges/discharges the battery pack by control of double closed loop emulation designed from **Figure 4**. Parameter of emulation as follows. The phase force is 70.7 V. The terminal voltage of the battery is 32 V. The energy storage inductance is 3mh. The filter parameter is designed by  $\omega = 150\pi$ ,  $A_p = 0.05$ . the inner resistance of the battery is  $R = 0.3$  ohm. the designed filter parameter is  $L_1 = 1.2$  mH,  $C = 8800 \mu\text{F}$ ,  $L_2 = 0.9$  mH, the AC side filter parameter  $L = 0.3$  mH,  $C = 880 \mu\text{F}$ , the step length is 1/51200/20. The PI parameter of inner current loop is  $\tau_{pi} = 0.11$ ,  $K_{pi} = 30$ . The PI parameter of outer current loop is  $\tau'_{pi} = 0.1$ ,  $K'_{pi} = 0.1$ . When the instruct current inversed, the polarity of battery inverse, and the current source PWM converter worked at AC inversion state. The battery is discharged and its energy feed back to the power grid. The PI parameter of outer current loop is  $\tau_{pi} = 0.1$ ,  $K_{pi} = 0.08$ . The PI parameter of inner current loop is  $\tau'_{pi1} = 0.4$ ,  $K'_{pi1} = 65$ ,  $\tau'_{pi2} = 0.4$ ,  $K'_{pi2} = 65$ . The terminal voltage of the battery is 80V, and the other parameter is the same with when the battery is charged.

From the emulation, we can see that whether DC side is charging or discharging, there is a low ripple and fast response. Through spectrum analysis of testing current, we know that the harmonic percent of charging current is 0.1%, discharging current is 0.05% and this fulfill the request of testing current ripple. If network side voltage and current are in-phase when charging, network side of rectifier show a negative resistance, network absorb positive power, realize the high power factor of battery power to feedback to network.

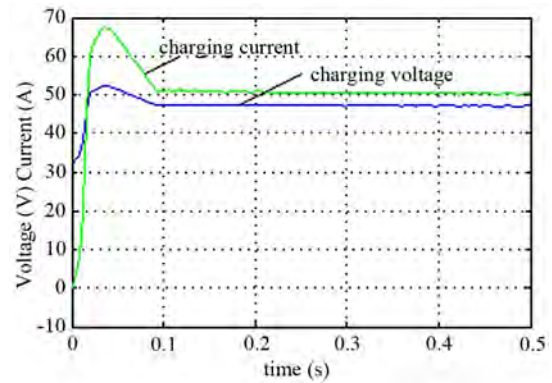
### 5. Experimental Procedure and Discution

#### 5.1 Experimental Procedure

In order to validate the correctness of structure and control method, this paper have done a sample of current source SVPWM convertor based on dq transformation and experienced with VRLA piles. Main circuit and structure is showed in **Figure 3**. This system used the TMS320F2812 of TI company as main control CMOS chip and switch frequency is 1.6 kHz. The parameter of DC side filter



(a)



(b)

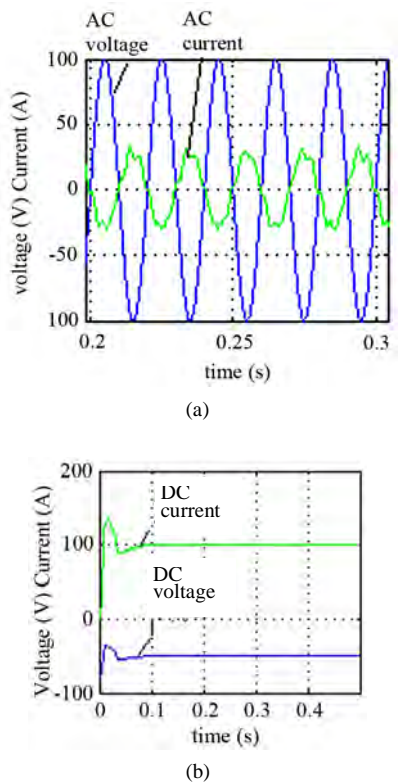
(a) the current and the voltage of the AC side; (b) the current and the voltage of the DC side

**Figure 7. Simulation result when the charging current  $I_{dc}^* = 50\text{A}$**

is same to the emulation parameter. The sample uses a 9 kW booster to supply voltage. The voltage of piles is 12.8 V and output voltage of transformer 23.8 V when experiencing. It takes use of DL1600 digital oscilloscope to observation the result of the experience and copy waveform, which was produced by Japanese YOKOGAWA Company. The waveform is saved as a \*.csv file and disposed in MATLAB. The data is analyzed by FFT to certify the output performance of the filtering result.

After filtering, the current harmonic of power gride side and DC side are all low, for example, if DC side's current harmonic is beyond 0.5%, corresponding, DC near to 100%. If we put DC and other harmonic current in the same histogram, those whose content is lower than 1% will be dimness and difficult to see. So DC's spectrum analysis output neglect the DC  $I_0$  which as a consult as to observe the other harmonic's spectrum distribution.

From the double closed loop charging test, we can see that AC side voltage and current are in-phase when charging; DC side output a current who has low ripple and fast response. When discharging the voltage and the cur-



(a) the current and the voltage of the AC side; (b) the current and the voltage of the DC side

**Figure 8. Simulation result when the discharging current  $I_{dc}^* = 100A$**

rent out phase, the battery’s energy feed back to the power grid with a high power factor.

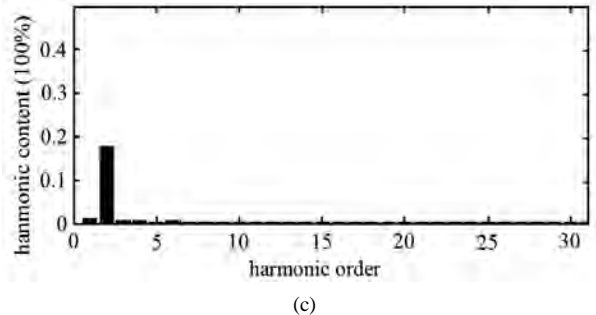
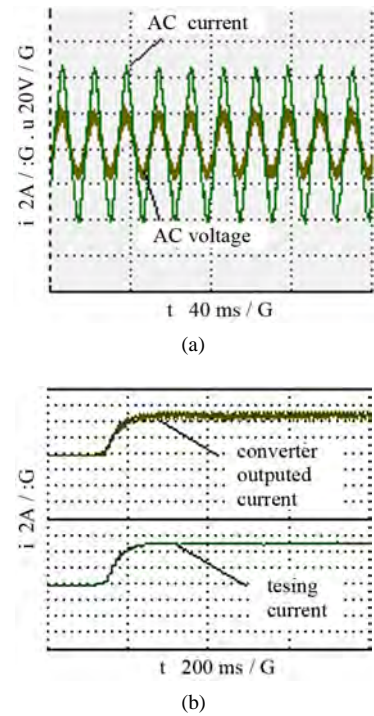
**5.2 Discussion: Analyze of Error**

Analyzing the experiment, there are two main influence, inner resistance of filtering inductance and three-phase voltage unbalance.

1) To measure the inductance in this experiment by two-bridge method, it’s resistance is 0.1 ohm. Those elements who have wastage will make the transmitted function pole of filter move left, so influence the propagation properties. As the literature [6] validate, the wastage of inductance will influence the filtering performance of filter. This is one of the important reason that make deviation between the experiment result and emulation.

But battery pack testing system need a 500A output current of rectifier. We need an inductance with thick diameter, a DC with small resistance and the influence of transmitted performance to transformer can be neglected. So the filter designed in this paper which has small wastage, fast response can satisfy the request of battery pack testing system.

2) There are a lot of 2-order harmonics in the spectrum of steady State current. Though the experiment realized



(a)voltage and current of the power grid side; (b)the test current and the converter outputted current; (c)spectrum analysis for the charging current

**Figure 9. 5A battery charging test by current source SVPWM converter controlled by 2-closed loop**

to make voltage and current in same phase, the current waveform of AC side is not perfect sine wave. Through measure the three-phase voltage of power, we find a phenomenon that the power in experiment is Three-Phase Unbalance and the three-phase voltage have thrice harmonic. All this will influence the result of the experiment result.

Some research [7,8] show that three-phase CSI direct voltage will produce 6,12,18 characteristic harmonic and 2,4,8,10 Non-characteristic Harmonic when three-phase unbalance. Direct voltage harmonic lead rectifier to produce DC current harmonic, in reverse, the DC current harmonic influence the waveform of alternating current. That’s to say, after PWM control, three-phaseCSI DC side’s harmonic current will produce  $n + 1$  harmonic current in AC side of rectifier.

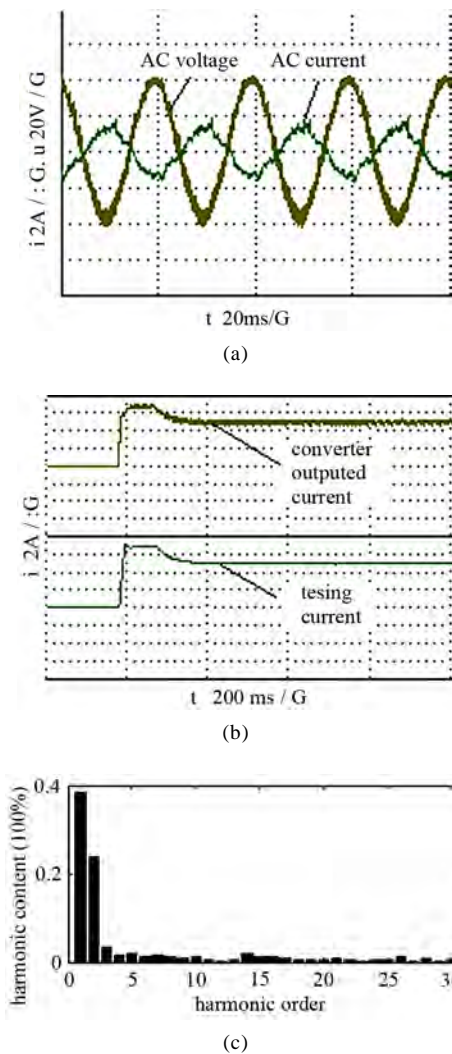


**Figure 10.** 5A battery discharging test by current source SVPWM converter controlled by 2-closed loop: (a) voltage and current of the power grid side; (b) the test current and the converter outputted current; (c) spectrum analysis for the charging current

From the result of experiment, after filtering, there are very little harmonic after 5 in current spectrums analyze. This is because that the design of filter's stop band frequency is 6 order harmonic. The decay to the harmonics that the order is bigger than 6 is 6n dB larger per sound interval than the 6-order harmonics. So the harmonic after 5 will be suppressed, also, harmonic in pass band will be suppressed too such as 2 harmonic just because of the DC filter we designed have enactment to the minimum attenuation.

When network's voltage is unbalanced, we can suppress the 2-order harmonic through proper control of three-phase CSI. Now there already have some research about the suppression of 2 harmonic in voltage source PWM DC side [9,10]. This method should be brought

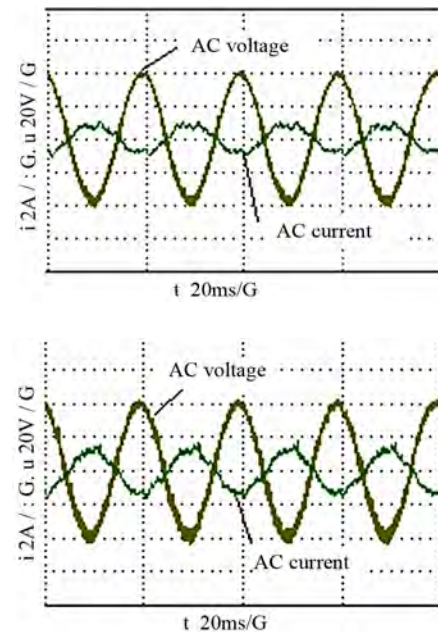


**Figure 11.** The voltage and current of power grid in 2A, 4A SVPWM discharging test

into the CSI. This paper will make this problem as the latter research and discuss deeply.

3) When discharging, the resistance changed and the equivalent resistance of charging/discharging is not the same [12]. Though this paper realize the double closed control in battery pack, there are some different between experiment result and emulation result when discharging, for example, a long time for system to Response, response speed slower than charging experiment. This is because the program is not perfect. So, the parameter of double closed loop control should be regulated according to resistance when charging.

## 5. Conclusions

CSI assisted with polar switch circuit can realize regulation of output voltage and current, attain the double-flow of energy; Double closed loop control system based on dq coordinate conversion to SVPWM converters used in the battery pack testing system. It's advantage of "fast response, high efficiency of energy conversion, bidirectional converting, high power factor of power grid side.

## 6. Acknowledgements

This research is supported by doctorate found of China University of Petroleum.

## REFERENCES

- [1] J. Bauman and M. A. Kazerani, "Comparative Study of Fuel Cell-Battery, Fuel Cell-Ultracapacitor, and Fuel Cell-Battery-Ultracapacitor Vehicles," *Vehicular Technology, IEEE Transactions on*, Vol. 57, No. 2, 2008, pp. 760-769.

- [2] L. X. Zhang, X. W. Yan, H. Li, *et al.*, "Design and Simulation of Fast-Response Filter Based on Locomotive Battery Testing System," *Proceedings of 12th International Power Electronics and Motion Control Conference EPE-PEMC'06*, Portoroz, 30 August-1 September, 2006.
- [3] L. X. Zhang, X. W. Yan, H. Li, *et al.*, "Design Method of Low Loss and Fast Response LC Filters Based on Locomotive Battery Testing System," *EPE Journal*, Vol. 18, No. 1, 2008.
- [4] L. X. Zhang, K. Wei and J. Li, "Control of Bidirectional Current Source SVPWM Converter in the Power Accumulator Battery Testing System," *Proceedings of Asia-Pacific Power and Energy Engineering Conference*, Chengdu, 2010.
- [5] B. Bhargava and G. Dishaw, "Application of an Energy Source Power System Stabilizer on the 10 MW Battery Energy Storage System at Chino Substation," *Power Systems*, Vol. 13, No. 1, 1998, pp. 145-151.
- [6] A. Davis, Z. M. Salameh and S. S. Eaves, "Comparison of a Synergetic Battery Pack Drive System to a Pulse Width Modulated AC Induction Motor Drive for an Electric Vehicle," *Energy Conversion*, Vol. 14, No. 2, 1999, pp. 245-250.
- [7] S.-H. Lee, S.-G. Song, S.-J. Park, *et al.*, "Grid-Connected Photovoltaic System Using Current-Source Inverter," *Solar Energy*, Vol. 82, No. 5, May 2008, pp. 411-419.
- [8] H. F. Ding, S. Y. Shu, X. Z. Duan, *et al.*, "A Novel Dynamic Voltage Restorer and its Unbalanced Control Strategy Based on Space Vector PWM," *International Journal of Electrical Power & Energy Systems*, Vol. 24, No. 9, November 2002, pp. 693-699.
- [9] X. Zhang, J.-Q. Ji, C.-W. Zhang, *et al.*, "Study of Internal Model Control Based Three-Phase PWM Rectifier under Unbalanced Input Voltage Condition," *Proceedings of the CSEE*, Vol. 25, No. 13, 2005, pp. 51-56.
- [10] J.-B. Xu, D.-X. He, J. Zhao, *et al.*, "A New Power Analysis Method of PWM Rectifier with Unbalanced Voltage Condition," *Proceedings of the CSEE*, Vol. 26 No. 16, 2006, pp. 80-85.
- [11] K.-G. Zhao, F. Pei, X.-D. Huang, Y.-T. Luo, *et al.*, "Variable Current dischargeable Characteristics and SOC Estimation of EV/HEV Battery[J]," *Proceedings of the CSEE*, Vol. 25, No. 9, 2005, pp. 164-168.
- [12] J.-P. Randin, "Reliability of Commercial Lithium Button Cells II. Effect of The State-of-Discharge and Environment on the Passivation Resistance," *Journal of Power Sources*, Vol. 25, No. 1, January 1989, pp. 61-74.

# Performance Analysis of Low Head Hydraulic Air Compressor

Walid Aniss Aissa<sup>1</sup>, Salama Abdel-Hady Mohamed<sup>2</sup>, Kamal Abdel-Fatah Ahmed<sup>3</sup>

<sup>1</sup>Mechanical Engineering Department, Faculty of Engineering at Rabigh, King Abdul-Aziz University, Jeddah, Saudi Arabia; <sup>2</sup>Mechanical Power Department, High Institute of Energy, South Valley University, Aswan, Egypt; <sup>3</sup>Egyptian Electricity Holding Company, Aswan, Egypt.  
Email: walid\_aniss@yahoo.com

Received April 19<sup>th</sup>, 2010; revised May 12<sup>th</sup>, 2010; accepted May 14<sup>th</sup>, 2010.

## ABSTRACT

*Hydraulic Air Compressor (HAC) is a device which converts hydraulic energy to energy of compressed air. A better exploitation of this hydraulic resource is currently investigated. The aim of the current work is to analyze a low head open type HAC in terms of compression ratio and HAC efficiency. The performance of HAC is both experimentally and theoretically investigated for various air admission system parameters (air tube length and diameter), downcomer length and hydraulic head. The results are both presented and discussed. Variation of the mean diameter of air bubbles in the downward flow in the downcomer is both determined and investigated. The losses in the whole system are classified, investigated and its impact on HAC is discussed.*

**Keywords:** *Experimental, Hydraulic Air Compressor, Performance*

## 1. Introduction

A Hydraulic Air Compressor is a device that uses the energy of a descending flow of water to compress air by entraining the air in the water flow as shown in the work by Widden *et al.*, [1].

Shapiro [2] described a thermodynamic analysis of hydraulic air compressor-gas turbine plant. He conducted a comparison between HAC-GT system and reference conventional gas turbine and hydroelectric power plants. He concluded that the novel system will have higher efficiency, lower cost, lower pollution production, and increased output compared to existing hydroelectric stations.

Bidini *et al.*, [3] presented a numerical model of a HAC to perform both an energy analysis of the system and to study its capability of exploiting natural hydraulic sites. They suggested using of isothermal compression in HAC's for an efficient energy conversion in combination with widely regenerated GT plants.

Bidini *et al.*, [4] reported a thermodynamic analysis of HAC-gas turbine energy conversion systems and compared their performance to conventional hydro-electric and gas turbine power plants. They concluded that the performance levels of such systems are higher comparable to those of combined cycle plants. They suggested performing further technical and environmental investiga-

tions.

Nishi [5] investigated replacing the compression process of a regenerative cycle by an isothermal compression process by using a hydraulic air compressor. He stated that by assuming conventional operating conditions and component characteristics, higher thermal efficiency of the new system was proved and that about 1.9 times greater output can be produced by the HAC-GT than by a conventional hydraulic power plant. In addition, he concluded that this system can be applied to improve the performance of existing hydraulic power plants as well as in planning new plants.

Rice and Wood [6] stated that HAC compresses gas at the expense of hydraulic energy by means of entrainment in a downward moving column of liquid with a subsequent separation of the air and liquid at a depth. They presented calculated performance for the HAC using the flow rate and net head combinations typical at small hydropower sites.

French and Widden [7] presented a hydropower system based on siphons in which the pressure of low-head water is converted into air pressure. Their analysis suggested that, with careful design of the flow passages to minimize losses, efficiencies of 70% or more should be achievable. They stated that the economics of the system are likely to be attractive owing to the low capital cost of

the system compared with conventional water-turbine systems. In addition, they stated that a siphon plant is suitable, in single-stage form, for heads up to about 1.7 m and that for higher heads, the system can be used in two or more stages.

The purpose of the present work is to carry out experimental and analytical investigation of low head open type HAC. In the current work, variation of mean diameter of air bubbles in the downward flow in the downcomer is both determined and investigated. The losses in the whole system are classified, investigated and its impact on HAC is discussed. The performance is both experimentally and theoretically investigated for various air admission system parameters, downcomer length and hydraulic head. The results are both presented and discussed.

## 2. Experimental Test Rig and Measuring Instruments

### 2.1 Experimental Test Rig

The High Institute of Energy open-type HAC test rig facility; shown in **Figure 1** is used in the present work. Two (upper and lower) impoundments (tanks) are connected to stilling chamber via two vertical pipes (downcomer and raiser). A certain amount of air is introduced into the water flow through a suitable intake device (air tube). Air is entrained into the water flow by the static pressure differential existing between the air at ambient condition (Section 0) and at the end of the air tube (Section 1). Different air admission device arrangements can be adopted to ensure the formation of two-phase flow at Section 2, which can be considered to coincide with Section 1. The stilling chamber is designed to obtain low flow velocity, thus allowing the air bubbles to separate from the water. Compressed air then gathers in the upper part of the stilling chamber and is supplied to the user. Leaving the chamber, water enters the raiser pipe (Section 5) and, through (Section 6), reaches the final impoundment (Section 7).

#### 2.1.1. Impoundments

##### a) Upper Impoundment

**Figure 1** illustrates schematic drawing and main dimensions of testing arrangement. Upper impoundment is cylindrical tank of 0.54 m diameter and 0.85 m height. The tank is fed by water from filling tank; **Figure 1**, via 2"(0.0508m) piping. A 2" ON/OFF valve (No. 1) is fitted between the upper impoundment and filling tank. In addition, over flow pipes are fitted on the side of the upper impoundment. The filling tank is mounted such that its base is 0.15 m above the upper overflow valve center to keep a constant water level in the upper impoundment. Both the upper impoundment and filling tank are sub-

jected to atmospheric pressure.

##### b) Lower Impoundment

It is a cylindrical tank having 0.54m diameter and 0.85m height. It is connected to the stilling chamber via a 6m pipe (raiser). Two over flow pipes; **Figure 1**, are mounted on the side of the tank at 0.32m and 0.67m from the base of the tank to sustain specific hydraulic head ( $H_y$ ) between the upper and lower impoundments. The hydraulic head between the impoundments is the driving force that ensures both air compression and the overcoming of concentrated and distributed losses. With analogy to the upper impoundment and filling tank, the lower impoundment is subjected to atmospheric pressure.

#### 2.1.2. Downcomer and Raiser

They are two commercial steel cylindrical pipes, each has one inch (0.0254 m) diameter. Longer one; the downcomer, has two portions, first portion is that below the upper impoundment and it has a fixed length of 8 m. The second portion ( $Y_{dc}$ ); **Figure 1**, is inside the upper impoundment and it has a variable length. Values of  $Y_{dc}$  times the downcomer diameter; ( $Y_{dc}/D_{dc}$ ) used in the present work are: 9.84, 11.81, 13.78, 15.75, 17.72, 19.68, 21.65 and 23.62. The shorter pipe; raiser has a fixed length of 6m. Tests are conducted for a fixed length of portion of raiser inside the lower impoundment to downcomer diameter ratio ( $Y_r/D_{dc}$ ) of 12.6. The length of the downcomer to its diameter ratio ( $H_{dc}/D_{dc}$ ) is variable based on the portion of downcomer length inside the upper impoundment ( $Y_{dc}$ ).

#### 2.1.3 Air Admission System

PVC tubes of different diameters ( $D_t$ ) and lengths ( $Y_t$ ); **Figure 1**, are mounted in the upper impoundment. Each air tube must be thoroughly adjusted to be concentric with the downcomer.

The diameters of the air tube to downcomer ratios ( $D_t/D_{dc}$ ) utilized in the present study are 0.55, 0.59, 0.63, 0.67, 0.71 and 0.75 respectively while their lengths to downcomer diameter ratios ( $Y_t/D_{dc}$ ) are 1.59, 2.36, 3.15, 3.94, 4.72 and 5.51 respectively.

Over flow pipes give the ability to change the hydraulic head ( $H_y$ ); **Figure 1**, giving hydraulic head to downcomer diameter ratios ( $H_y/D_{dc}$ ) of 59,65,75,79,81 and 94 respectively.

#### 2.1.4 Stilling Chamber

Settling chamber; **Figure 1**, is an air tight steel tank which dimensions are 0.5m  $\times$  0.5m  $\times$  0.6m. The tank has a Prisbex sheet mounted on its side to indicate the level of water inside the tank. ON/OFF valve (No. 4) is used to release the compressed air gathered in the upper part of the settling chamber via air exit tube having 1/2" (0.0127 m) piping.

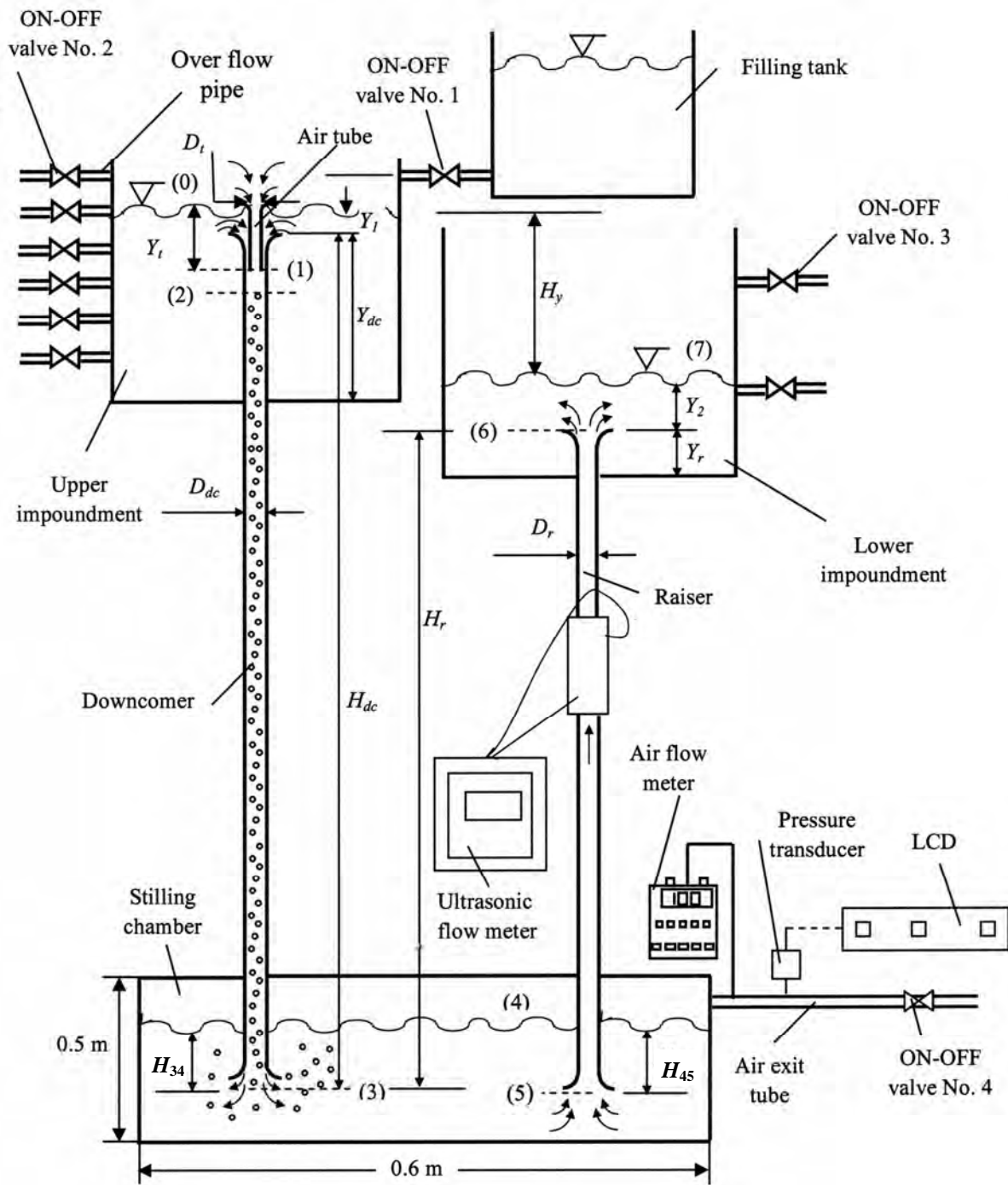


Figure 1. Schematic drawing and main dimensions of testing arrangement

## 2.2 Measuring Instruments

The pressure and flow rate for both air and water are measured; **Figure 1**, to study the HAC performance and the characteristics of mixing process. The main features of the measuring instruments are described in the following section.

### 2.2.1 Flow Rate Measuring Instruments

#### a) Water Flow Meter

The water flow rate is measured and indicated using a transient-time flow meter (Ultrasonic flow meter), **Figure 1**. The flow meter characteristics are specified in **Table 1**.

#### b) Air Flow Meter

The flow rate of the air is measured using air meter unit.

**Table 1. Transient-time flow meter characteristics**

Accuracy	1 - 2 % of indicated flow
Sensitivity	0.015 m/sec
Zero drift	Less than 0.015 m/sec
Repeatability	Less than 0.5 %
Response rate (damping)	From 0.2 sec to 5 min
Flow velocity range	12.2 m/sec
Linearity	0.0009 m/sec

**Table 2. Specifications of air meter unit**

Air meter	Type Model	EXTECH	
		407123	
Measured quantity	Velocity		Temperature
Range	0.2 – 20 m/sec		0 to 50°C
Accuracy	(3% + 1d) rdg or ± (1%+1d) FS whichever is greater		±0.8°C
Resolution	0.1 m/sec		0.1°C
Response time	200 msec		2 minutes

**Table 3. Specifications of Pressure transducer**

Specification	Range	Specification	Range
Measuring range	-1 to 2.5 bar	Accuracy	± 0.75% o.r
Linearity	± 1%, ± 1 digit o.f.r	Operating temp.	0 to 50 °C
Hysteresis	≤ 0.09%		

This unit is designed to measure air velocity, flow rate, temperature, pressure, humidity and heat flow. It may be connected to computer and/or printer for accessing stored data and printing it. The specifications of the air meter, velocity, and temperature measurement are listed in **Table 2**.

### 2.2.2 Pressure Measuring Instrument (Pressure Transducer)

Pressure transducer is used to measure the pressure of compressed air issuing from the stilling chamber through ON/OFF valve No. 4. Specifications of the transducer are listed in **Table 3**. The reading of the pressure transducer is displayed on the amplifier display unit.

## 3. Mathematical Modeling of the Hac

An analytical, one-dimensional approach assuming isothermal flow in HAC which allows the simulation of its operation and evaluation of the complete energy losses and presented in previous work by Bidini *et al.*, [3] is utilized in this study. The plant configuration shown which is incorporated in this study; **Figure 1**, is an open type HAC. Flow in HAC may be represented by the fol-

lowing intervals:

### 3.1 Interval 0-1

The air entrainment process efficiency is described by the air-water mass flowrate ratio;  $\mu$ .

$$\mu = \dot{m}_a / \dot{m}_w \quad (1)$$

Equations (2) and (3) are used for mass and energy conservation equations:

$$\dot{m}_w = \rho_w (A_{dc} - A_t) V_{w1} \quad (2)$$

$$\frac{P_0}{\rho_w} + gH_{01} = \frac{P_1}{\rho_w} + \frac{V_{w1}^2}{2} + K_{01} \left( \frac{V_{w1}^2}{2} \right) \quad (3)$$

The irreversibility for the water flow is given by the inlet losses, represented by the  $K_{01}$  coefficient. Hence, the loss for the water flow can be quantified as

$$Loss_{01w} = \dot{m}_w K_{01} \left( \frac{V_{w1}^2}{2} \right) \quad (4)$$

The energy conservation equation for an isothermal flow is applied to calculate the air flow loss:

$$Loss_{01a} = \dot{m}_a \left[ RT \ln \left( \frac{P_0}{P_1} \right) - \frac{V_{a1}^2}{2} \right] \quad (5)$$

The total energy loss for interval 0-1;  $Loss_{01}$ , is the sum of that of water and air flows in the interval 0-1

$$Loss_{01} = Loss_{01w} + Loss_{01a} \quad (6)$$

### 3.2 Interval 1-2

Interval 1-2 is assumed to be of infinitesimal length; nevertheless its limiting sections are characterized by different physical meanings. The water and air flow cross-sections can then be schematically defined as  $A_w$  and  $A_{dc} - A_w$  respectively. Pressure and velocity at Section 2 can be determined by numerically solving the simultaneous non-linear system of equations for mass and momentum; Equations (7) and (8) respectively.

$$\dot{m}_a = \frac{P_2}{RT} (A_{dc} - A_{w2}) (V_{w2} - V_{r2}) \quad (7)$$

$$P_1 A_t + P_1 (A_{dc} - A_t) - P_2 A_{dc} = \dot{m}_a (V_{w2} - V_{r2}) + \dot{m}_w V_{w2} - \dot{m}_w V_{w1} - \dot{m}_a V_{a1} \quad (8)$$

where,  $V_r$  is the relative velocity between the air bubbles and water. It was stated in previous work by Bidini *et al.*, [3] that experimental measurements suggested an initial value;  $V_{r2}$  which equals 0.244 m/s.

### 3.3 Interval 2-3

The two-phase flow for the generic volume between Sections 2 and 3 is analyzed by means of discretization technique by applying mass and momentum, conservation

equations at small volumes of fluid along the downcomer pipe. Hence, the solution at the generic depth  $z$  is used to determine the pressure and velocity at depth  $z + dz$ , having the incremental values of pressure and water velocity,  $dP$  and  $dV_w$ , as unknown quantities. The model suggested by Bidini *et al.*, [3]; is presented by Equations (9), (10).

$$\begin{aligned} d\dot{m}_a &= d \left[ \frac{P}{RT} (A_{dc} - A_w) (V_w - V_r) \right] \\ &= d \left\{ \frac{P}{RT} \left( A_{dc} - \frac{\dot{m}_w}{\rho_w V_w} \right) \left[ V_w - V_{r2} \left( \frac{P_2}{P} \right)^{\frac{1}{6}} \right] \right\} = 0 \end{aligned} \quad (9)$$

$$\begin{aligned} \dot{m}_w (V_w + dV_w) - \dot{m}_w V_w + \dot{m}_a [(V_w - V_r) + d(V_w - V_r)] \\ - \dot{m}_a (V_w - V_r) = PA_{dc} - (P + dP)A_{dc} + \rho_a (A_{dc} - A_w) g dz \\ + \rho_w A_w g dz - f \frac{V_w^2}{2} \pi \rho_w dz D_{dc} \end{aligned} \quad (10)$$

The variation of bubble-water relative velocity; is:

$$V_r = V_{r2} \left( \frac{P_2}{P} \right)^{\frac{1}{6}} \quad (11)$$

Two kinds of irreversibility are present between Sections 2 and 3; wall friction ( $Loss_{23w}$ ) and friction between water and air bubbles ( $Loss_{23b}$ ) due to the relative velocity;  $V_r$ :

$$Loss_{23w} = \sum_{i=1}^N f \frac{V_{w,i}^3}{8} \rho_w \pi D_{dc} dz$$

&

$$Loss_{23b} = N_b \sum_{i=1}^N C_D \rho_w \pi \frac{D_{b,i}^2}{8} V_{r,i}^3 \quad (12)$$

where,  $N$  is the number of segments determined by:

$$N = H_{23} / dz \quad (13)$$

$N_b$  represents the number of bubbles crossing any downcomer section, which is constant with  $z$  and is calculated as:

$$N_b = dz \frac{\dot{m}_a}{\rho_{a2} (V_{w2} - V_{r2}) \pi D_{b2}^3} \quad (14)$$

The mean diameter of air bubbles at Section 1;  $D_{bi}$  is determined by imposing the instantaneous equilibrium between the drag force and the buoyancy force.

$$D_{bi} = \frac{3V_{r,i}^2 C_D}{4g} \quad (15)$$

where,  $C_D$  is drag coefficient for a sphere [8].

### 3.4 Interval 3-4

The discharge loss occurs at interval 3-4 is calculated as:

$$Loss_{34} = \dot{m}_w K_{34} \left( \frac{V_{w3}^2}{2} \right) \quad (16)$$

### 3.5 Interval 4-5

In the stilling chamber, compressed air bubbles easily diffuse through the water and gather in the upper part of the stilling chamber; with a pressure  $P_4$ , from where air is delivered to the user. The compression ratio;  $\beta$  is defined as

$$\beta = P_4 / P_0 \quad (17)$$

At the raiser entry, an inlet loss is located ( $Loss_{45}$ ), which is defined by

$$Loss_{45} = \dot{m}_w K_{45} \left( \frac{V_{w5}^2}{2} \right) \quad (18)$$

### 3.6 Interval 5-6

The only flow loss along the raiser is due to water-wall friction, and is defined as

$$Loss_{56} = \dot{m}_w f \frac{V_{w5}^2}{2D_{DC}} H_r \quad (19)$$

### 3.7 Interval 6-7

At the end of the raiser, the discharge loss ( $Loss_{67}$ ) is evaluated from

$$Loss_{67} = \dot{m}_w K_{67} \left( \frac{V_{w6}^2}{2} \right) \quad (20)$$

Total losses are the sum of air tube loss;  $Loss_{01a}$ , downcomer water inlet loss;  $Loss_{01w}$ , water-air bubble friction loss along the downcomer;  $Loss_{23b}$ , water-wall friction loss along the downcomer;  $Loss_{23w}$ , downcomer water outlet loss;  $Loss_{34}$ , raiser water inlet loss;  $Loss_{45}$ , water-wall friction loss along the raiser;  $Loss_{56}$ , and raiser water outlet loss;  $Loss_{67}$ .

Hydraulic air compressor efficiency; assuming isothermal compression in HAC [3], is defined as

$$\eta_{HAC} = \mu \frac{RT \ln \beta}{g H_y} \quad (21)$$

## 4. Results and Discussions

**Figures 2 and 3** illustrate values of mean air bubbles diameters computed along the downcomer for specific air tube length, hydraulic head and downcomer length for different air tube diameters and air tube lengths respectively.

**Figure 2** illustrates the variation of mean air bubbles diameter along the downcomer for different air tube diameters for specific air tube length, hydraulic head and downcomer length. It may be remarked from the figure that the mean air bubbles diameter decreases along the downcomer. This may be relied to that as the depth increases; pressure raises hence compresses the air bubbles and decreasing their volume. Consequently, the portion of the downcomer available for the water flow becomes wider, while the velocity progressively decreases. In addition, it may be concluded from the above mentioned

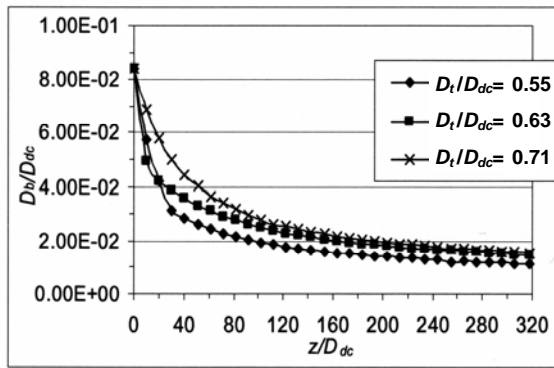


Figure 2. Variation of mean air bubbles diameter along the downcomer for different air tube diameters;  $H_{dc}/D_{dc} = 415.35$ ,  $H_y/D_{dc} = 59$ ,  $Y_t/D_{dc} = 3.94$

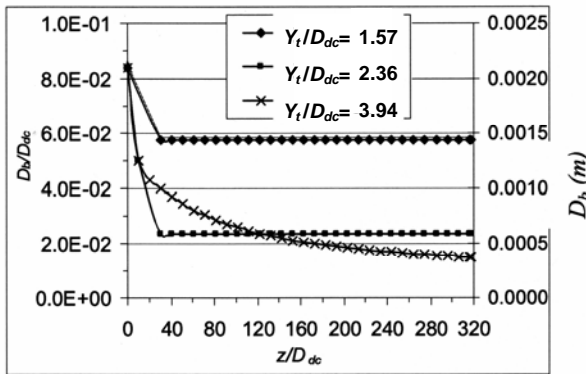


Figure 3. Variation of mean air bubbles diameter along the downcomer for different air tube lengths;  $H_{dc}/D_{dc} = 417.32$ ,  $H_y/D_{dc} = 59$ ,  $D_t/D_{dc} = 0.63$

figure that the mean air bubbles diameter along the downcomer in general increases with increasing air tube diameter. This may be relied as follows, for specific air-mass flow rate, increasing air tube diameter, while keeping other parameters constant, leads to a reduction in the air velocity in the downcomer. In addition, increasing air tube diameter leads to a reduction in the corresponding water area in the downcomer which leads to a subsequent increase in water velocity and hence relative velocity. As it may be observed from Equation (15), the mean air bubbles diameter is proportional to the square of relative velocity. Hence, increasing air tube diameter leads to a corresponding increase in the mean air bubbles diameter. Further, experimental results showed that varying the downcomer length,  $H_{dc}$  has no appreciable effect on the mean air bubbles diameter.

Figure 3 illustrates the variation of the mean air bubbles diameter along the downcomer for different air tube lengths;  $Y_t$  and specific air tube diameter  $D_t$ , hydraulic heads;  $H_y$ , and downcomer length;  $H_{dc}$ . From the above mentioned figure, it may be concluded that the mean air

bubbles diameter along the downcomer in general decreases with increasing the air tube length. This may be relied to the subsequent increase in the pressure along the downcomer due to the increase of air tube length. Results indicated that varying the hydraulic head does not appreciably affect the mean air bubbles diameter.

As it was stated in [3], the performance of HAC shows a marked dependence on the main operational and design parameters. Experimental results proved that the losses are air tube diameter dependent. Figures 4 to 6 present the variation of HAC total losses, air tube loss and downcomer water inlet loss as percentages to total loss respectively for various air tube diameters and specific downcomer length, hydraulic head, and air tube length. It may be remarked from Figures 4-6 that up to specific air tube diameter  $\approx 0.71$  downcomer diameter, both downcomer water inlet loss and air tube loss and hence total loss in general decrease with increasing the air tube diameter. Further increase of air tube diameter leads to an increase in downcomer water inlet loss, air tube loss and total loss. Hence, there is an intermediate range of air tube diameter which has low total loss.

From these figures and forthcoming figures concerning HAC efficiency, it may be concluded that the air tube-to-

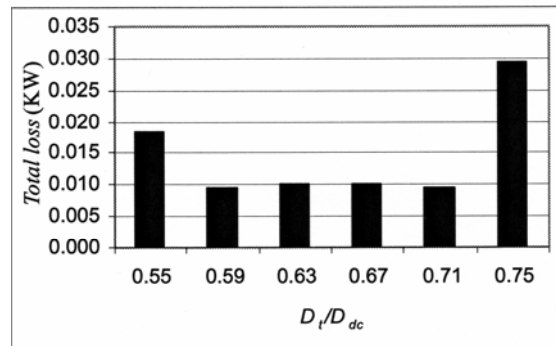


Figure 4. Variation of total loss with air tube diameter;  $H_y/D_{dc} = 59$ ,  $H_{dc}/D_{dc} = 417.32$ ,  $Y_t/D_{dc} = 3.94$

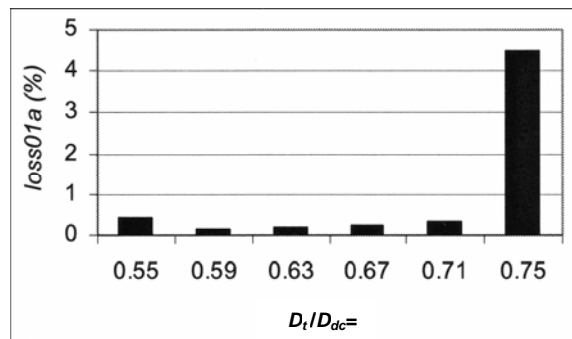


Figure 5. Variation of air tube loss as a percentage to total loss with air tube diameter;  $H_y/D_{dc} = 59$ ,  $H_{dc}/D_{dc} = 417.32$ ,  $Y_t/D_{dc} = 3.94$

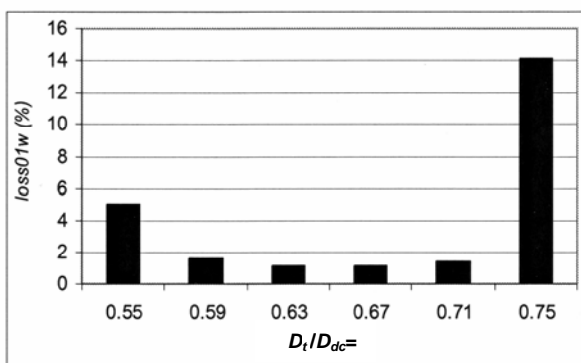


Figure 6. Variation of downcomer water inlet loss as a percentage to total loss with air tube diameter;  $H_y/D_{dc} = 59$ ,  $H_{dc}/D_{dc} = 417.32$ ,  $Y_t/D_{dc} = 3.94$

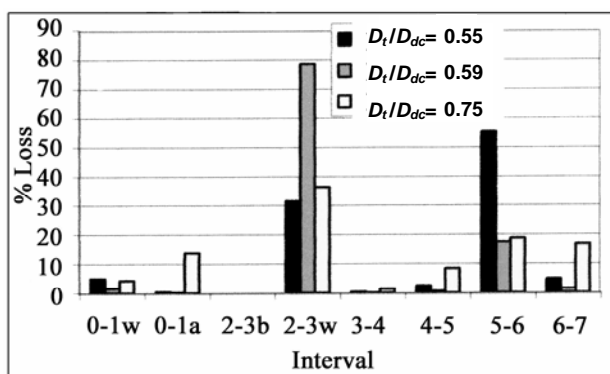


Figure 7. Percentages of loss in various intervals;  $Y_t/D_{dc} = 3.94$ ,  $H_y/D_{dc} = 59$ ,  $H_{dc}/D_{dc} = 417.32$

downcomer diameter ratio of 0.71 corresponds to the highest HAC performance for the current investigation limits.

Figure 7 illustrates the percentages of losses in different intervals for various air tube diameters and specific hydraulic head, air tube length and downcomer length. It may be concluded from the above mentioned figure that while the friction between water and air bubbles due to the relative velocity;  $Loss_{23b}$ , represents a minor portion of the total losses in the HAC, the water-wall friction loss along the downcomer;  $Loss_{23w}$  and the water-wall friction loss along the raiser;  $Loss_{56}$ , represent the major part of the total losses in the HAC. This may be attributed to the friction between water and downcomer or raiser. Experimental results illustrated that the air tube length;  $Y_t$ , the downcomer length;  $H_{dc}$  and hydraulic head;  $H_y$  do not have a remarkable effect on the percentage losses in HAC.

To the best of our knowledge, there are no references that treat the effect of air tube length;  $Y_t$  on HAC performance. Figure 8 illustrates the variation of compression ratio;  $\beta$  with air tube length;  $Y_t$  for sample of air tube diameters;  $D_t$  and specific downcomer length;  $H_{dc}$  and

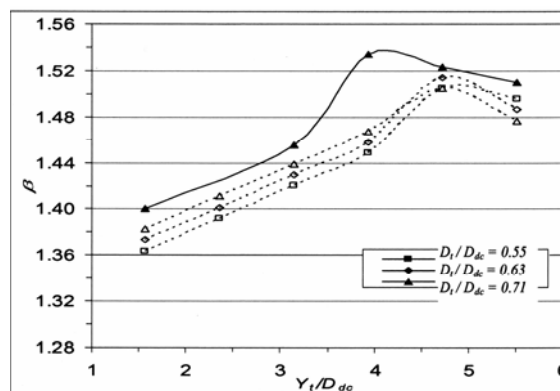


Figure 8. Variation of HAC compression ratio with air tube length;  $H_{dc}/D_{dc} = 417.32$ ,  $H_y/D_{dc} = 59$

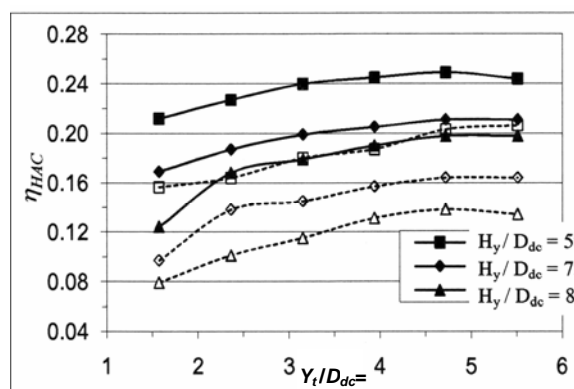


Figure 9. Variation of HAC efficiency with air tube length for various hydraulic heads;  $D_t/D_{dc} = 0.63$ ,  $H_{dc}/D_{dc} = 417.32$

hydraulic head;  $H_y$ . Continuous lines in the whole figures of the current work refer to analytical results, while dashed lines refer to experimental results.

Figure 9 presents the variation of the hydraulic air compressor efficiency;  $\eta_{HAC}$  with air tube length;  $Y_t$  for various hydraulic heads;  $H_y$  and specific air tube diameter;  $D_t$  and downcomer length;  $H_{dc}$ . For short air tube lengths, the static pressure at the air admission end section would be so near to atmospheric that air entrainment would be very difficult, this leads to a low compression ratio and hence low hydraulic air compressor efficiency as it may be observed from Figures 8,9. Herein, experimental results indicated that  $\beta$  and thus  $\eta$  increase with increasing  $Y_t$  until a value equals approximately equals  $4.72 D_{dc}$ . This may be relied as follows, increasing  $Y_t$  leads to an increase in differential pressure across air tube as may be remarked in Equation (3) and a subsequent increase in air mass flowrate and hence compression ratio;  $\beta$ . Beyond that value of  $Y_t$ , a decrease in the air bubbles volume leads to a decrease in air-water mass flowrate ratio and a subsequent decrease in both  $\beta$  and  $\eta_{HAC}$ . However, the peak value of

compression ratio for analytical results corresponds to air tube length equals 3.94 times the downcomer diameter; which is shifted from the corresponding value for experimental results. This may be due to the simplified analytical model utilized in the current work.

It may be concluded from **Figures 10 and 11** that the compression ratio and HAC efficiency slightly increase with increasing downcomer length while holding other parameters constant. As indicated in previous work by Bidini *et al.*, [3],  $\beta$  increases with increasing  $H_{dc}$  and as may be remarked from Equation (21), HAC efficiency increases with increasing the logarithm of compression ratio ( $\beta$ ). This fact may be observed **Figure 10** in which  $\beta$  increases with increase of  $H_{dc}$  until a value of  $H_{dc}$  nearly equals  $417.32 D_{dc}$ . With further increase in  $H_{dc}$  a flat portion or slight decrease in  $\beta$  is remarked. This may be relied to that: the water-bubble friction loss, together with the water-wall friction losses in the downcomer and raiser increase with increasing  $H_{dc}$ , because of the deeper position of the stilling chamber needed to compress the air.

It may be remarked from the results that increasing the air tube diameter up to 0.71 downcomer diameter leads to a subsequent increase in compression ratio. This may be relied to increasing of air tube diameter leads to an increase in air mass flow rate and subsequent increase in

pressure inside stilling chamber and hence increase in compression ratio. With further increase in air diameter, the water velocity increases leading to increase in wall friction loss in the downcomer and subsequent decrease in compression ratio and HAC efficiency.

It may be concluded from the above figures that the efficiency decreases with increasing the hydraulic head when holding the other parameters constant. This may be reasoned using Equation (21) which indicates that the efficiency is inversely proportional to hydraulic head for specific air tube diameter (*i.e.*, air-water mass flow rate ratio;  $\mu$ ). The observed difference between the theoretical efficiencies and those evaluated experimentally in the above figures may be relied to the fact that the efficiency depends on the actual configuration of the air intake system as indicated in previous work by Bidini *et al.*, [3].

**Figure 12** shows the relation between hydraulic air compressor efficiency and compression ratio for various hydraulic heads while holding other parameters constant.

The quiet low efficiency range estimated in the current work; which is in any case lesser than 34 percent, is appreciably low compared to that stated in the literature; 0.50-0.85 [3]. This may be relied to that the air-to-water mass flow rate ratio range ( $0.29 \times 10^{-4}$  to  $1.04 \times 10^{-4}$ ) and hydraulic head ( $\leq 2.4$  m) are appreciably lower than the

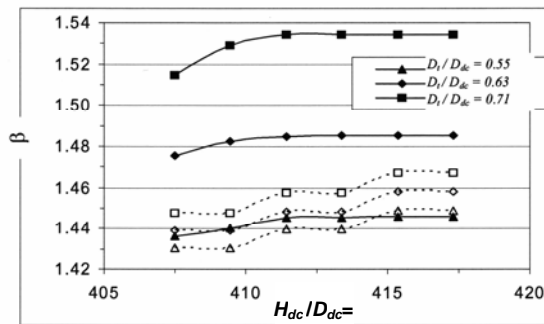


**Figure 10.** Variation of compression ratio with downcomer length;  $Y_t/D_{dc} = 3.94$ ,  $H_y/D_{dc} = 59$

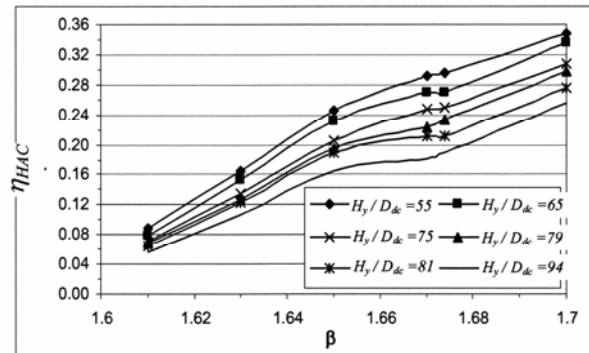


**Figure 12.** Variation of efficiency with compression ratio for various hydraulic heads;  $Y_t/D_{dc} = 3.94$  and  $H_{dc}/D_{dc} = 417.32$

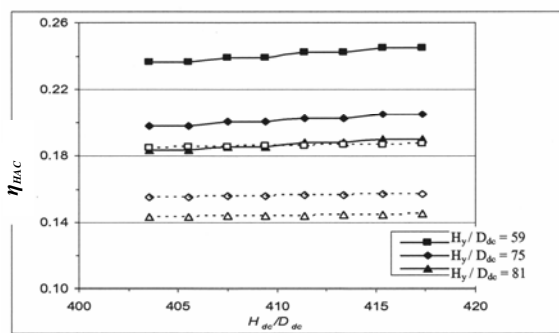


**Figure 11.** Variation of HAC efficiency with downcomer length for various hydraulic heads;  $D_t/D_{dc} = 0.63$ ,  $Y_t/D_{dc} = 3.94$

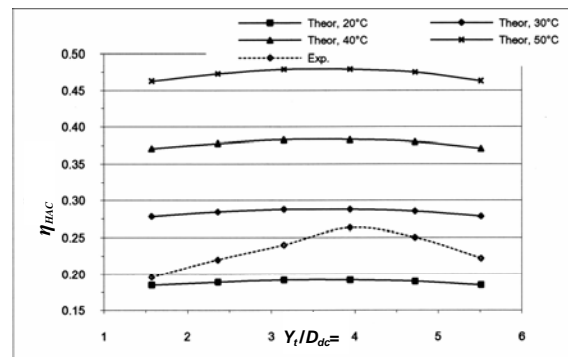


**Figure 13.** Effect of temperature on HAC efficiency  $H_y/D_{dc} = 59$ ,  $D_t/D_{dc} = 0.71$ , and  $H_{dc}/D_{dc} = 417.32$

corresponding values in [3], ( $4 \times 10^{-4}$  to  $8 \times 10^{-4}$ ) and ( $\approx 2.4$  m) respectively.

The range of the hydraulic head used in the current work may be more efficiently used in a siphon type as it was stated in previous work by French and Widden [7] that siphon type is suitable for heads up to 1.7 m.

**Figure 13** illustrates the effect of atmospheric temperature on theoretical hydraulic air compressor efficiency for the range of air tube lengths utilized in the current investigation and comparison with efficiency evaluated experimentally at atmospheric temperature of 30°C for specific air tube diameter, hydraulic head and downcomer length. It may be concluded from Equation (21) and the figure that the efficiency is proportional to the atmospheric temperature.

## 5. Conclusions

In this work, an analytical and experimental investigation of a low head open type HAC is reported to analyze the performance of the system and to investigate the effect of various non-dimensional parameters. The presented results suggest that the mean air bubbles diameter decreases along the downcomer, increases with both increasing air tube diameter and decreasing air tube length and not appreciably affected by the downcomer length,  $H_{dc}$  or hydraulic head;  $H_y$ . It was concluded that the water-wall friction loss along the downcomer;  $Loss_{23w}$  and the water-wall friction loss along the raiser;  $Loss_{56}$ , represent the major portions of the total losses in the HAC. It was concluded that compression ratio increases with increasing air tube length or diameter up to a certain limit (3.94 and 0.71 downcomer diameter respectively) and decreases with further increase in their values. Air tube diameter has the same effect on HAC efficiency. In addition it was found that both the compression ratio and efficiency increase with increasing downcomer length and that beyond a certain limit (417.32 times downcomer diameter), compression ratio curve flattens. Low HAC efficiency reported in the current investigation may be due to the low

values of both hydraulic head and air-water mass flow rate ratio. The range of the hydraulic head used in the current work may be more efficiently utilized in a siphon type which is suitable for heads up to 1.7 m. Further, it is indicated that the hydraulic air compressor efficiency is proportional to the atmospheric temperature.

## REFERENCES

- [1] M. B. Widden, M. J. French and G. A. Aggidis, "Economic Energy from Low-Head Water by Conversion to Air Pressure," *Proceedings of Hydropower 2004 World Class Engineering in a Challenging Environment Symposium*, Lancaster University, London, 2004, pp. 1-10.
- [2] J. L. Shapiro, "The Hydraulic Air Compressor Combustion Turbine," *ASME Cogen-Turbo, IGTI*, Vol. 9, 1994, pp. 291-297.
- [3] G. Bidini, C. N. Grimaldi and L. Postriotti, "Thermodynamic Analysis of Hydraulic Air Compressor-Gas Turbine Power Plants," *Proceedings Institution of Mechanical Engineers*, Vol. 211, 1997, pp. 429-437.
- [4] G. Bidini, C. N. Grimaldi and L. Postriotti, "Performance Analysis of a Hydraulic Air Compressor," *Proceedings Institution of Mechanical Engineers*, Vol. 213, 1999, pp. 191-203.
- [5] A. Nishi, "Highly Efficient Gas Turbine System Using Isothermal Compression," *JSME International Journal*, Vol. 39, No. 3, 1996, pp. 615-620.
- [6] W. Rice and B. D. Wood, "Characteristics of the Hydraulic Air Compressor as a Small Hydro-Power Device," *Small-Hydro-Power-Fluid-Mach ASME Winter Annual Meeting*, Chicago, 1980, pp. 81-87.
- [7] M. J. French and M. B. Widden, "The Exploitation of Low-Head Hydropower by Pressure Interchange with Air, Using Siphons," *Proceedings of IMechE Part A-Journal of Power and Energy*, Vol. 215, No. 2, 2001, pp 223-230.
- [8] R. L. Street, G. Z. Watters and J. K. Vennard, "Elementary Fluid Mechanics," Seventh Edition, J. Willey & Sons, New York, 1996.

## Nomenclature

$A$	Cross sectional area	$m^2$	$\eta$	Efficiency	-
$C_D$	Drag coefficient	-	$\mu$	Air-water mass flowrate ratio	-
$C_P$	Specific heat at constant pressure	J/kg.K	$\rho$	Density	$kg/m^3$
$D$	Diameter	m			
$f$	Friction factor	-			
$g$	Gravitational acceleration	$m/s^2$	HAC	<b>ABBREVIATIONS</b> Hydraulic Air Compressor	
$H$	Difference in water level	m	GT	Gas turbine	
$K$	Local loss coefficient	-			
$\dot{m}$	Mass flow rate	kg/s		<b>Subscripts</b>	
$N$	Number of segments in interval 2-3	-	a	Air	
$P$	Pressure	N/ $m^2$	b	Air bubbles	
$R$	Air gas constant	J/ kg.K	comp	Compression	
$T$	Absolute temperature	K	dc	Downcomer	
$V$	Velocity	m/s	HAC	Hydraulic Air Compressor	
$W$	Work	J	i	Segment counter in interval 2-3 , i =1 to N	
$Y$	Pipe length	m	j	Section j, j = 0,1,2,.....,7	
$z$	Depth	m	r	Raiser, relative	
$Loss$	Loss of power	W	t	Air tube	
			wall	Wall	
	<b>Greek letters</b>		y	Hydraulic	
$\beta$	Compression ratio	-			

# Modeling of Work of Filling Granular Filter with Active Cooling

Alexander D. Rychkov

Institute of Computational Technologies of Siberina Branch of Russian Academy of Sciences, Novosibirsk, Russia.  
Email: [rych@ict.nsc.ru](mailto:rych@ict.nsc.ru)

Received November 24<sup>th</sup>, 2009; revised May 10<sup>th</sup>, 2010; accepted May 12<sup>th</sup>, 2010.

## ABSTRACT

*The solid propellant gas generators having high gas capacity are widely used for fast pressurization of elastic shells of saving devices of different applications. A typical example of such devices are safety system of automobile (airbags). After collision of an automobile with an obstacle the combustion products of gas generator fill the shell during 60 – 100 milliseconds. However the temperature of combustion products even of “low-temperature” fuel compositions of gas generators appears not below 1500K and to reduce of its it is necessary to apply a various types of porous and filling granular filters. There are passive and active granular filters. The passive filter can cool of combustion products as a result of absorption of heat only. The active cooling is evaporation of the granule material and in this case takes a place more intensive cooling of combustion products in the filter. The numerical modeling of cooling process of high-temperature combustion products at their movement in bulk of granular filter of active cooling is investigated. As the material of granules was used the carbonate of magnesium. At its heating takes a place process of gasification and formation of a porous slag shell which sublimates at higher temperature. The physical model of such spherical granule can be presented as the central part consisting of the carbonate magnesium surrounded with the porous slag spherical shell through which gaseous products of gasification of the central part are filtered. The problem of distribution of heat in each granule is Stefan problem when at the given temperature on the surface of sphere there is the front of gasification moving inside of the bulk of material. It is assumed that combustion products are the perfect gas moving in the filter. The upwind difference scheme of the second order of the accuracy with TVD properties was applied to calculation of the movement of gas. The results of calculations at various values of key parameters of the active and passive filters allow to draw a conclusion about enough high efficiency of active cooling filters.*

**Keywords:** *Mathematical Modeling, Granular Filters, Heat-and-Mass Transfer*

## 1. Introduction

The gas generators with a solid-fuel propellant, which possess a high gas output, have gained a widespread acceptance in the devices for a rapid supercharge of elastic shells applied in various life saving devices. The devices for car safety (air bags) are the typical examples of such devices, in which the supercharge of safety cushions protecting the driver and the passengers from traumas in accident situations must occur during 60-100 milliseconds. The temperature of combustion products of even “low-temperature” fuel compositions of such gas generators, however, proves to be above 1500 K, and to reduce it to acceptable values, which do not burn through the material of walls of elastic inflated shells, one uses various porous and filling granular filters. The filling granular filters with a granulated material of the so-called active cooling are sufficiently promising for such purposes. In such filters,

the material of granules may decompose at their heating thereby contributing to a more intense cooling of the combustion products both at the expense of heat absorption at the evaporation of granules and at the expense of mixing of low-temperature gaseous products of the decomposition of granules with high-temperature combustion products of the gas generator. At present, the computations of the performance of such filters are carried out within the framework of engineering approaches based on the use of balance relations closed by various empirical dependencies.

## 2. Physical and Mathematical Models of the Filter Functioning

The magnesium carbonate was considered as the material of granules. A simplified kinetic scheme of such a granule was accepted as a model of the granule destruction.

The magnesium carbonate gasification with the formation of porous shells was assumed to occur at the granule heating, and this process occurred during two stages. The water steam is at first released, and the first slug shell forms according to the scheme:  $4\text{Mg}(\text{CO}_3) \cdot \text{Mg}(\text{OH})_2 \cdot 4\text{H}_2\text{O} \rightarrow 4\text{Mg}(\text{CO}_3) \cdot \text{MgO}(\text{solid}) + 5\text{H}_2\text{O}(\text{steam})$ , then, at a higher temperature, this slug shell decomposes in its turn into a solid residual (the second slug shell) and the carbonic acid:  $4\text{Mg}(\text{CO}_3) \cdot \text{MgO} \rightarrow 5\text{MgO}(\text{solid}) + 4\text{CO}_2(\text{gas})$ .

The following basic assumptions were made at the modeling of processes in the cooling chamber with a pouring active filter:

- The filter represents a porous medium consisting of spherical granules of the same size;
- The gasification of the granule at its heating is governed by a model of the compressing kernel with a solid porous frame. The carbon dioxide and the water steam are the gaseous gasification products;
- The combustion products of a solid-fuel propellant of the gas generator are represented by a chemically non-reactive perfect gas consisting of the mixture of the carbon dioxide (the mass fraction  $Y_{\text{CO}_2} = 0.8$ ) and the water vapors (the mass fraction  $Y_{\text{H}_2\text{O}} = 0.2$ );
- The gaseous medium in the cooling chamber consists of a mixture of the carbon dioxide, water steam, and air, which fills the chamber at the initial moment of time. The gaseous mixture motion is unsteady, axisymmetric, and is governed by the system of the Navier-Stokes equations;
- The filter granules are at rest, the exchanges of the momentum and energy between the gas and granules as well as the mass supply from the granules due to their gasification are considered;
- The alteration of the gaseous phase composition at the expense of a diffusion and transfer of non-reacting mixture components is taken into account.

## 2.1 Mathematical Model of the Granule Destruction

The physical model of a spherical granule of the filter may be presented in the form of a sphere with the central kernel (**Figure 1**) consisting of the magnesium carbonate, which is surrounded by two porous slug shells (1,2), through which the gaseous decomposition products are filtered. The entire granule in its initial state is a kernel. In the process of its heating, one can identify three main stages. The first stage starts from the granule heating at the expense of heat exchange with the carrying gas until the temperature on its surface reaches the first temperature of gasification  $T_g$ . After that, the second stage starts-the formation of the first slug shell (1) and the

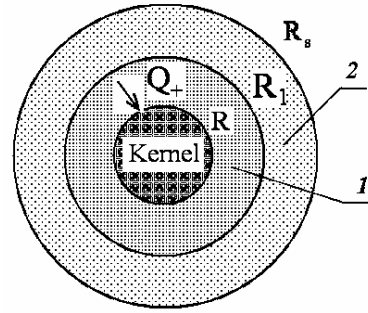


**Figure 1. Scheme of the granule gasification.**

gasification front motion towards the sphere center, if the heat flux  $Q_+$  to the boundary of the granule kernel ( $r = R$ ) exceeds its outflow  $Q_-$  inside the kernel. The velocity of the gasification front motion is determined from the condition  $r_p = (Q_+ - Q_-) / (L_p \rho_p)$ , where  $L_p$ ,  $\rho_p$  are the phase transition heat and the kernel material density, respectively. When the temperature on the granule surface  $r = R_s$  reaches the second gasification temperature  $T_{g1}$  ( $T_{g1} > T_g$ ) the slug shell material also starts to be gasified. A new gasification front  $r = R_1$  arises, which also moves to the sphere center and forms the second slug shell (2). The motion velocity of the second gasification front is determined similarly:  $r_{p1} = (Q_{1+} - Q_{1-}) / (L_{p1} \rho_{p1})$ , where  $Q_{1+}$ ,  $Q_{1-}$ ,  $L_{p1}$ ,  $\rho_{p1}$  are the heat fluxes to the gasification front and from it as well as the phase transition heat and the density of the material of the first slug shell. This is the third stage of the process. The radius of the external shell  $R_s$  remains constant. When describing the gasification process the following main assumptions were made:

- 1) The difference of the actual granule shape (for example, the cylinder) from the spherical shape is taken into account by introducing an equivalent sphere diameter  $d_{eq} = (6V_{gr} / \pi)^{1/3}$ , where  $V_{gr}$  is the granule volume.
- 2) The gaseous decomposition products are in a thermal equilibrium with slug frames. There are no chemical reactions and heat sources.
- 3) The gas pressure in porous medium is constant and is equal to the ambient pressure.
- 4) The porous shells are handled as a continuum with unified thermophysical characteristics inside it, which are averaged for the gaseous and solid phases.

The problem is considered in the one-dimensional unsteady formulation, the heat equation is written in the spherical coordinate system separately for the kernel and porous shells:

- a) The granule kernel ( $0 \leq r \leq R_0$ )

$$C_p \rho_p \frac{\partial T_p}{\partial t} = \frac{1}{r^2} \frac{\partial}{\partial r} \left( r^2 \lambda_p \frac{\partial T_p}{\partial r} \right), \quad (1)$$

b) The spherical layers of porous shells

$$(R_{+0} \leq r \leq R_{-1}, R_{+1} \leq r \leq R_s,)$$

$$\frac{\partial(C\rho)_{av} T_s}{\partial t} + \frac{\partial((m \cdot C)_{av} T_s)}{\partial r} = \frac{1}{r^2} \frac{\partial}{\partial r} \left( r^2 \lambda_{av} \frac{\partial T_s}{\partial r} \right), \quad (2)$$

where the second item on the left-hand side accounts for the heat transfer inside the shell at the expense of gaseous gasification products,  $m = r_p \cdot \varepsilon_p \cdot \rho_p$  for the first shell and  $m = r_{p1} \cdot \varepsilon_{p1} \cdot \rho_{p1} + r_p \cdot \varepsilon_p \cdot \rho_p$  for the second shell,  $\varepsilon_p, \varepsilon_{p1}$  are the mass fractions of gaseous products at the gasification of shells.

The description of the above three process stages reduces to the formulation of various boundary conditions for Equations (1) and (2). At the first stage ( $R = R_s$ ), Equation (1) is solved under the following boundary conditions:  $\frac{\partial T_p}{\partial r} \Big|_{r=0} = 0$ ;  $\lambda_p \frac{\partial T_p}{\partial r} \Big|_{r=R_s} = \frac{Nu \cdot \lambda}{2R_s} (T - T_p)$ ,

where  $T$  is the gaseous phase temperature near the granule surface;  $\lambda, Nu$  are the thermal conductivity coefficient of gas and the Nusselt number, respectively. The problem is solved until the condition  $T_p \Big|_{r=R} = T_g$  is satisfied. At the second stage, Equations (1) and (2) are solved jointly under the following boundary conditions:

$$\frac{\partial T_p}{\partial r} \Big|_{r=0} = 0; \quad T_p \Big|_{r=R-0} = T_s \Big|_{r=R+0} = T_g. \quad (3)$$

The velocity of the motion of the front of the kernel gasification is determined from the condition

$$r_p = (\lambda_{av} \frac{\partial T_s}{\partial r} \Big|_{r=R+0} - \lambda_p \frac{\partial T_p}{\partial r} \Big|_{r=R-0}) / (L_p \rho_p). \quad (4)$$

The new position of the gasification front boundary is found from the solution of equation  $\frac{dR}{dt} = -r_p$ . The boundary condition at  $r = R_s$  are specified depending on whether there is here a gasification of the shell material (the third stage) or there is no gasification. If  $T_s \Big|_{r=R_s} < T_{g1}$  (no gasification), then the following condition is specified:

$$\lambda_{av} \frac{\partial T_s}{\partial r} \Big|_{r=R_s} = \frac{Nu \cdot \lambda}{2R_s} (T - T_s), \quad (5)$$

otherwise the condition  $T_s \Big|_{r=R_s} = T_{g1}$  is specified. If there is gasification here (the third stage) the motion velocity of

the new gasification front is determined from a condition similar to (4), but with its values of thermophysical parameters. According to the accepted model of compressing kernel, the granule radius  $R_s$  is set constant, and the heat-exchange condition (5) is again specified on the granule surface.

The averaged thermophysical parameters of porous shells were determined as follows:  $(C\rho)_{av} = \varepsilon C_{pg} \rho_g + (1 - \varepsilon) C_b \rho_b$ ;  $\lambda_{av} = \varepsilon \lambda_g + (1 - \varepsilon) \lambda_b$ , where  $\varepsilon$  is the mass fraction of gaseous products at the gasification of corresponding shells. Gas parameters in porous shells:

$$\rho_g = \frac{p}{R_0 T_s / M_g}; \quad u_g = \varepsilon \frac{\rho_b r_b}{\rho_g} \left( \frac{R}{R_s} \right)^2; \quad \lambda_g = \frac{\mu_g C_{pg}}{Pr};$$

$r_b, C_b, \lambda_b, \rho_b$  is the motion velocity of the gasification front of the corresponding shell and its thermophysical parameters;  $p$  is the pressure in gaseous phase near the granule surface. The dynamic viscosity coefficient was determined by the Sutherland formula:  $\mu_g = \frac{1.503 \cdot 10^{-6} \cdot T_s^{3/2}}{T_s + 122}$ . A correction to the Nusselt number,

which is related to the presence of a transverse blowing through the surface of the porous shell at its gasification was taken into account within the framework of the so-called "film" model [1]:  $Nu = \frac{Re_j Pr}{\exp(Re_j Pr / Nu_0) - 1}$ ,

where  $Re_j = \frac{\rho_g u_g 2 \cdot R_s}{\mu_g} \Big|_{r=R_s}$ ,  $Nu_0$  is the Nusselt number without considering the blowing ( $Nu_0 = 2$  for the sphere);  $Pr$  is the Prandtl number. In the case when the particle shape differs from the sphere the value of the  $Nu_0$  number is to be determined by comparing the computed results with experiment.

2.2 The Model of Gas-Dynamic Processes

The diagram of a setup for testing the filling granular filters is presented in **Figure 2**.

It consists of a solid-fuel gas generator, from which the high-temperature combustion products enter the cooling chamber filled with the magnesium carbonate granules of the same size. Since the investigation of processes in the cooling chamber was the main objective of the present work, it is sufficient to use the balance (zero-dimensional) mathematical model ( $x_0 \leq x \leq 0$ ) for computing the gas-dynamic parameters in the combustion chamber of the gas generator

$$\frac{dV\rho}{dt} = (G_+ - G_-), \quad G_+ = S_p \rho_p r_b,$$

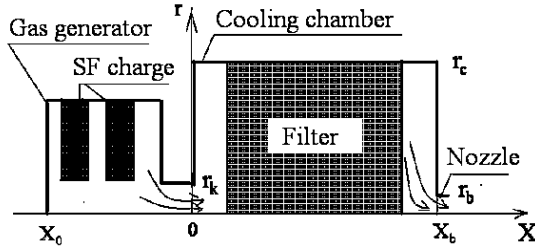


Figure 2. Scheme of the experimental setup

$$G_- = F_k \frac{p}{\sqrt{RT}} \sqrt{\frac{2k}{k-1}} \left[ \left( \frac{p}{p_k} \right)^{-2/k} - \left( \frac{p}{p_k} \right)^{-(k+1)/k} \right]^{1/2} \quad (6)$$

$$\frac{dV\rho E}{dt} = (G_+ Q_+ - G_- (C_p T_- + u^2/2)), \quad E = C_v T + u^2/2$$

where  $S_p$ ,  $\rho_p$ ,  $r_b$  are the total area of the burning surface of the fuel, its density, and the linear combustion velocity;  $V$ ,  $T$ ,  $p$ ,  $\rho$  are the free volume of the combustion chamber, which varies as the solid-fuel propellant burns out, the temperature, the pressure, and the gas density therein;  $k$ ,  $C_v$  are the adiabatic exponent of combustion products and their specific heat under a constant volume;  $E$ ,  $Q_+$  are the specific internal energy and the heat of fuel combustion;  $F_k$ ,  $p_k$  are the area of the outlet section of the combustion chamber and the mean pressure in the cooling chamber near its left wall. The subscript refers to the parameters in the outlet section of the combustion chamber.

Gas flow in the cooling chamber ( $0 \leq x \leq x_b$ ,  $0 \leq r \leq r_c$ ) is governed by the following system of equations:

$$\frac{\partial \rho}{\partial t} + \frac{\partial \rho u}{\partial x} + \frac{1}{r} \frac{\partial}{\partial r} (r \rho v) = J_p + J_{p1}, \quad (7)$$

$$\begin{aligned} & \frac{\partial \rho Y_{H_2O}}{\partial t} + \frac{\partial \rho u Y_{H_2O}}{\partial x} + \frac{1}{r} \frac{\partial}{\partial r} (r \rho v Y_{H_2O}) \\ & = \frac{\partial}{\partial x} \left( \rho D \frac{\partial Y_{H_2O}}{\partial x} \right) + \frac{1}{r} \frac{\partial}{\partial r} \left( r \rho D \frac{\partial Y_{H_2O}}{\partial r} \right) + J_p \end{aligned}, \quad (8)$$

$$\begin{aligned} & \frac{\partial \rho Y_{CO_2}}{\partial t} + \frac{\partial \rho u Y_{CO_2}}{\partial x} + \frac{1}{r} \frac{\partial}{\partial r} (r \rho v Y_{CO_2}) \\ & = \frac{\partial}{\partial x} \left( \rho D \frac{\partial Y_{CO_2}}{\partial x} \right) + \frac{1}{r} \frac{\partial}{\partial r} \left( r \rho D \frac{\partial Y_{CO_2}}{\partial r} \right) + J_{p1} \end{aligned}, \quad (9)$$

$$\begin{aligned} & \frac{\partial \rho Y_A}{\partial t} + \frac{\partial \rho u Y_A}{\partial x} + \frac{1}{r} \frac{\partial}{\partial r} (r \rho v Y_A) \\ & = \frac{\partial}{\partial x} \left( \rho D \frac{\partial Y_A}{\partial x} \right) + \frac{1}{r} \frac{\partial}{\partial r} \left( r \rho D \frac{\partial Y_A}{\partial r} \right), \end{aligned} \quad (10)$$

$$\begin{aligned} & \frac{\partial \rho u}{\partial t} + \frac{\partial \rho u^2}{\partial x} + \frac{1}{r} \frac{\partial}{\partial r} (r \rho u v) + \varepsilon_g \frac{\partial p}{\partial x} \\ & = \frac{\partial}{\partial x} \left( 2 \varepsilon_g \mu \frac{\partial u}{\partial x} \right) + \frac{1}{r} \frac{\partial}{\partial r} \left( r \varepsilon_g \mu \left[ \frac{\partial u}{\partial r} + \frac{\partial v}{\partial x} \right] \right) - \beta u \end{aligned}, \quad (11)$$

$$\begin{aligned} & \frac{\partial \rho v}{\partial t} + \frac{\partial \rho u v}{\partial x} + \frac{1}{r} \frac{\partial}{\partial r} (r \rho v^2) + \varepsilon_g \frac{\partial p}{\partial r} \\ & = \frac{\partial}{\partial x} \left( \varepsilon_g \mu \left[ \frac{\partial v}{\partial x} + \frac{\partial u}{\partial r} \right] \right) + \frac{1}{r} \frac{\partial}{\partial r} \left( 2 r \varepsilon_g \mu \frac{\partial v}{\partial r} \right) - 2 \frac{\varepsilon_g \mu v}{r^2} - \beta v \end{aligned}, \quad (12)$$

$$\begin{aligned} & \frac{\partial \rho E}{\partial t} + \frac{\partial [u(\rho E + \varepsilon_g p)]}{\partial x} + \frac{1}{r} \frac{\partial}{\partial r} r v (\rho E + \varepsilon_g p) \\ & = \frac{\partial}{\partial x} \left( \varepsilon_g \lambda \frac{\partial T}{\partial x} \right) + \frac{1}{r} \frac{\partial}{\partial r} \left( r \varepsilon_g \lambda \frac{\partial T}{\partial r} \right) + \end{aligned} \quad (13)$$

$$\gamma (T_{sg} - T) + (C_{p(H_2O)} J_p + C_{p(CO_2)} J_{p1}) T_{sg},$$

$$p = R_0 \rho_g T \left( \frac{Y_{CO_2}}{M_{CO_2}} + \frac{Y_{H_2O}}{M_{H_2O}} + \frac{Y_A}{M_A} \right), \quad \rho = (1 - \varepsilon) \rho_g,$$

$$\varepsilon = \rho_p / \rho_p^0, \quad \varepsilon_g = 1 - \varepsilon,$$

$$C_p = C_{p(CO_2)} Y_{CO_2} + C_{p(H_2O)} Y_{H_2O} + C_{p(A)} Y_A,$$

$$E = C_v T + (u^2 + v^2) / 2,$$

where  $E$ ,  $\rho_p$ ,  $\rho_p^0$  are the total internal energy, the number and physical densities of particles (granules);  $C_p$ ,  $C_v$ ,  $\lambda$ ,  $D$  are the coefficients of the specific heats, thermal conductivity and diffusion of gas;  $Y_{CO_2}$ ,  $Y_{H_2O}$ ,  $Y_A$ ,  $M_{CO_2}$ ,  $M_{H_2O}$ ,  $M_A$  are the mass fractions of the carbon dioxide, water steam, and air, respectively, and their molecular weights;  $T_{sg}$  is the temperature of the granule surface. Its value is found from the solution of the problem of the heat propagation in the granule (see Subsection 2.1).

The values of extra gas supplies in Equation (7) at the gasification of granules were found from the following expressions:

$$C_D = \begin{cases} c_1 = \frac{24}{Re_p} + \frac{4.4}{\sqrt{Re_p}} + 0.42, & \varepsilon \leq 0.08; \\ c_2 = \frac{4}{3\varepsilon} \left[ 1.75 + \frac{150\varepsilon}{\varepsilon \phi Re_p} \right], & \varepsilon \geq 0.45; \\ \frac{(\varepsilon - 0.08)c_2 + (0.45 - \varepsilon)c_1}{0.37}, & 0.08 < \varepsilon < 0.45, \end{cases} \quad Re_p = \frac{\rho_d |\bar{U}|}{\mu}$$

$$J_p = 4\pi n \varepsilon_p r_p \rho_p R^2, \quad J_{p1} = 4\pi n \varepsilon_{p1} r_{p1} \rho_{p1} R_1^2,$$

where  $n$  is the number of granules per unit volume (it is determined from the filter pouring conditions).

The drag coefficient  $\beta$  is calculated with the aid of a linear combination of the Ergun's formula and the formula for the drag coefficient of a sphere [2]:

where  $\phi$  is the form parameter accounting for the granule shape deviation from the sphere;  $d_p$  is the granule diameter.

The heat-transfer coefficient  $\gamma$  was determined by the formula of the work [3].

$$\gamma = \frac{\pi d_p n}{\phi} \lambda \text{Nu}, \quad \text{Nu} = 0.395 \text{Re}_p^{0.64} \text{Pr}^{0.33}.$$

The boundary conditions were specified for system (7-13) as follows. At the impermeable walls of the cooling chamber, the no-slip conditions and the conditions for heat exchange absence were specified. At  $x=0$  in the inlet section of the chamber, through which the combustion products are supplied from the gas generator ( $r \leq r_k$ , see **Figure 1**):  $\rho u = G_- / F_k$ ,  $\rho v = 0$ ,  $Y_{\text{H}_2\text{O}} = 0.2$ ,  $Y_{\text{CO}_2} = 0.8$ ,  $Y_A = 0$ ,  $T = T_-$ .

In the outlet section of the chamber ( $x = x_b$ ,  $r \leq r_b$ , see Fig. 1), where the outflow of combustion products may occur both in the subsonic and supersonic regime, their flow rate was specified, which was computed from the known gas-dynamic formulas for adiabatic flow

$$\rho u = \frac{p}{\sqrt{RT}} \sqrt{\frac{2k}{k-1}} \left[ \left( \frac{p}{p_{\text{at}}} \right)^{-2/k} - \left( \frac{p}{p_{\text{at}}} \right)^{-(k+1)/k} \right]^{1/2},$$

$$\text{if } \frac{p}{p_{\text{at}}} < \left( \frac{k+1}{2} \right)^{k/(k-1)} \quad (\text{subsonic outflow});$$

$$\rho u = \frac{p\sqrt{k}}{\sqrt{RT}} \left( \frac{2}{k+1} \right)^{\frac{k+1}{2(k-1)}},$$

$$\text{if } \frac{p}{p_{\text{at}}} \geq \left( \frac{k+1}{2} \right)^{k/(k-1)} \quad (\text{supersonic outflow}),$$

where  $p_{\text{at}}$  is the atmospheric pressure;  $k$  is the adiabatic exponent for the mixture of combustion products and gasification products. Its value was computed by averaging over the nozzle section of the quantity  $k = C_p / (C_p - R)$ , where  $R$  is the gas constant of the mixture.

The "mild" boundary conditions were specified here for remaining flow parameters. The cooling chamber was assumed to be filled with air under the atmospheric pressure at the initial moment of time.

The upwind second-order LU difference scheme possessing the TVD properties, which was close to a scheme

described in the work [4], was applied for numerical solution of Equations (7-13). The interaction between the gas and granules was taken into account on the basis of the splitting in terms of physical properties. The difference grid had the size  $200 \times 30$  in the  $(x, r)$  plane, which ensured the computation of flow parameters with the accuracy of about 5%.

### 3. Some Computational Results

The computations were carried out for the following values of the cooling chamber parameters. The cooling chamber diameter is 80 mm; the mass of the filter granules is 0.6 kg. The temperatures of phase transitions for the first and second slug shells are  $T_g = 500$  K and  $T_{g1} = 653$  K, the heats of phase transitions  $L_p = 326$  kJ/kg and  $L_{p1} = 644$  kJ/kg. The mass fractions of the gasification products of granules  $\varepsilon_p = 0.2$ ,  $\varepsilon_{p1} = 0.3$ . The equivalent diameter of the granule  $d_p = 5$  mm. The diameter of the outlet section of the cooling chamber  $d_b = 7$  mm. The temperature of combustion products at the cooling chamber inlet amounted to 2290 K. The value of the adiabatic exponent in the combustion chamber of the gas generator  $k = 1.25$ .

**Figure 3** shows a comparison of computed results with the results of test-bench tests (black circles) in terms of the temperature value in the outlet section of the cooling chamber. The value  $M_g$  [g] is the total mass of the formed gaseous products of the decomposition of filter granules. A fairly satisfactory agreement in the temperature values points to the performance of the proposed physical and mathematical model of the process. The amount of gas supply from the gas generator was insignificant, and the pressure level in the cooling chamber exceeded only slightly the atmospheric pressure level.

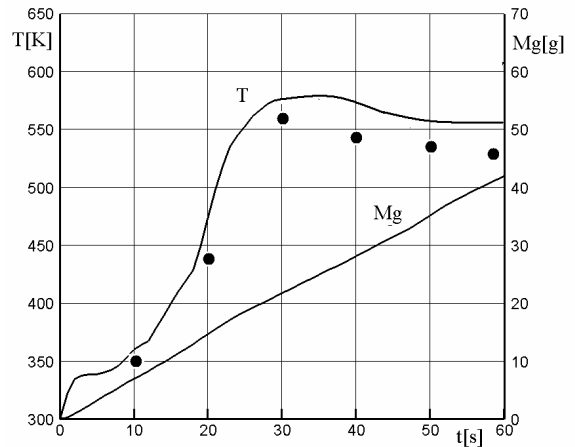


**Figure 3.** Temperature variation at the cooling chamber outlet

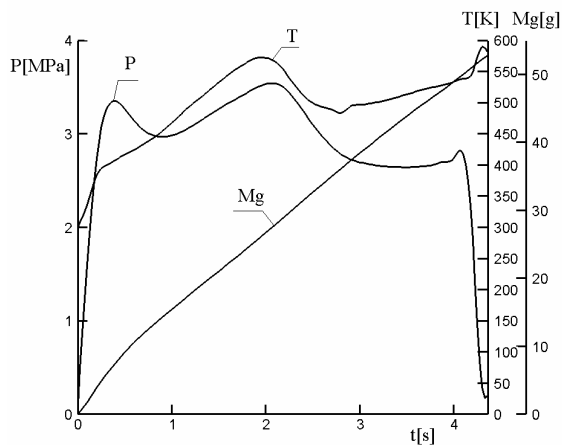


**Figure 4.** The pressure and temperature variation at  $x = 0$  in the cooling chamber

The pressure and temperature behavior at the cooling chamber outlet at a higher value of gas supply from the combustion chamber of the gas generator is shown in **Figure 4**. The pressure drop after the first peak is related to the start of the gas outflow through the outlet section (the nozzle) of the cooling chamber. A further pressure growth is due to an additional gas supply of the gasification products of granules. As the intensity of granules gasification reduces this gas supply decreases, which results in the appearance of the second peak on the pressure curve and in the pressure decrease after it. As the solid-fuel propellant of the gas generator burns out the fraction of decomposition products of filter granules having a lower temperature increases in the gaseous mixture, which maintains the temperature at the cooling chamber outlet at a sufficiently low level.

**Figures 5** and **6** show a comparison of the character of the variation of similar pressure and temperature curves for the active and passive filters. It was assumed in the case of the passive filter that its material (the same magnesium carbonate) is not subjected to destruction. A nearly linear pressure growth in the passive filter after the first peak is due to the use in the gas generator of a solid-fuel propellant with a so-called progressive combustion surface whose size increases with time. In the active filter, the extra gas supply from granules leads already to a nonmonotonous character of the pressure variation whose mean level proves to be higher than in the passive filter (**Figure 5**). This circumstance also leads to a reduction of the work time of the gas generator because the combustion velocity of the solid fuel increases with the pressure growth, and the solid-fuel propellant burns out faster. In the passive filter, the diminution of the temperature of combustion products of the gas generator occurs only at the expense of the heat absorption by the filter granules, which leads to a practically linear temporal dependence of the gas temperature at the cool-

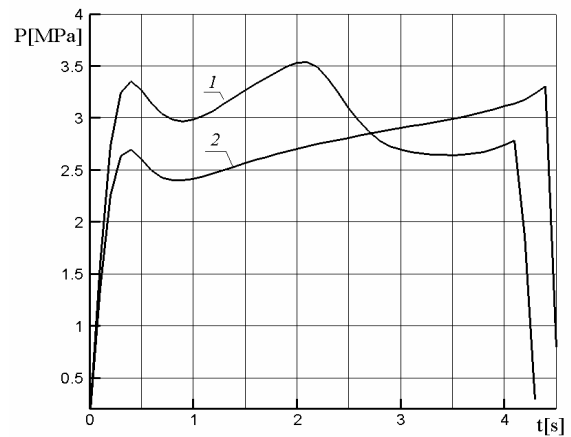


**Figure 5.** Pressure variation in the cooling chamber at  $x = 0$  for the active (1) and passive (2) filters

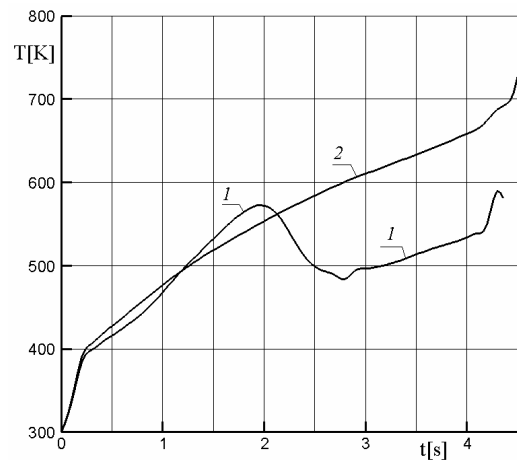


**Figure 6.** Temperature variation at the cooling chamber outlet for the active (1) and passive (2)

ing chamber outlet. In the active filter, the temperature at the chamber outlet proves to be much lower as a result of the mixing of low-temperature products of the decomposition of granules with combustion products (**Figure 6**).

#### 4. Conclusions

1) The developed mathematical model describes sufficiently adequately the process of the cooling of high-temperature combustion products of solid-fuel propellants of the gas generators in the filters of active cooling.

2) Numerical modeling results showed a higher efficiency of cooling of combustion products at the use of active filters in comparison with passive filters.

#### REFERENCES

- [1] E. P. Volkov, L. I. Zaichik and V. A. Pershukov, "Modeling of Solid Fuel Combustion," Nauka, Moscow, 1994.
- [2] L. E. Sternin, "Foundations of Gas Dynamics of Two-Phase

- Flows in Nozzles,” Mashinostroenie, Moscow, 1974.
- [3] M. A. Goldshtik, “Transfer Processes in Granular Layer,” Published by the Institute of Thermophysics of the Siberian Branch of the USSR Academy, *Science*, Novosibirsk, 1984.
- [4] S. Yoon and A. Jameson, “An LU-SSOR Scheme for the Euler and Navier-Stokes Equations,” *AIAA Paper*, 1987, pp. 87-600.

# Green Environment: Decision-Making and Power Utility Optimization towards Smart-Grid Options

Dolores DeGroff

Department of Civil, Environmental and Geomatics Engineering Florida Atlantic University, Boca Raton, USA.  
Email: [degroff@fau.edu](mailto:degroff@fau.edu)

Received February 24<sup>th</sup>, 2010; revised May 11<sup>th</sup>, 2010; accepted May 12<sup>th</sup>, 2010.

## ABSTRACT

*Decision-making toward prudent energy conservation is a primary issue in the power utility management while conceiving green environment. Presented in this paper are relevant considerations and prudent ways of decision-making thereof. Examples are furnished to illustrate the underlying considerations and are discussed using practical examples. Specifically green ambient is considered and the underlying payoff resulting from each combination of strategies adopted (or courses of action taken) by the technology-option participants is evaluated. Game-theoretic pursuits are followed.*

**Keywords:** Green Building, Power Utility Conservation, Payoff-matrix, Game-theoretic Formulations

## 1. Introduction

Green environment is an eco-friendly ambient. In modern civil and environmental engineering point of view, it translates into conceiving a building infrastructure, which is eco-friendly. Such green-centric ambient involves spacial proliferation of green constructions (sustainable buildings) and making the surroundings at large with processes that are environmentally responsible and resource-efficient throughout the life-cycle of the green entities. Making of a green environment starts from siting to design, construction, operation, maintenance, renovation, and deconstruction efforts with eco-friendly features. Relevant approach expands and complements the classical building design concerns of economy, utility, durability, and comfort.

The common denominator in forming green ambient is to impact human health preservation. This is accomplished by: Efficient usage of energy, water, and other resources; protecting occupant health against any eco-related hazards; reducing waste, pollution and environmental degradation and developing a congenial ambient contributing larger employee productivity.

Green-building/environment concept envisages using natural materials that are available locally. Other related topics include sustainable design, green architecture, and energy efficient buildings so as to bring in harmony with the natural features and resources surrounding the site. Among several key steps in designing sustainable buildings and environment, generating on-site renewable energy and optimization of power utility are very impor-

tant. Relevant efforts involve prudent decision-making in the underlying engineering. The focus of this paper is to exemplify related decision-making analyses.

## 2. Green Environment Optimization

The concept of “green” towards sustainable development of environment stems from energy (especially fossil oil) utilization concerns. The crisis and the environment pollution issues of 1970s posed the niche and desire for more energy-efficient and environmentally-friendly construction practices as well as looking at integrated and synergistic designs in new and existing infrastructure.

Associated conservation emphasizes taking advantage of renewable resources, for example, using sunlight through passive solar, active solar and photovoltaic techniques and using plants and trees through green roofs, rain gardens, and for reduction of rainwater run-off. Also, techniques, such as using packed gravel or permeable concrete *in lieu* of conventional concrete or asphalt to enhance replenishment of ground water, are directed to realize a green ambient.

The technological practices in realizing a total green environment are still infantile, but are constantly evolving. Relevant efforts may differ from region-to-region globally but, the diversity is unified on siting plus structural design efficiency, energy efficiency, water efficiency, materials efficiency, indoor environmental quality enhancement, operations and maintenance optimization, and waste and toxics reduction the essence of green building and green environment is an optimization of one

or more of the above considerations. Further, related synergistic design would yield specific and individual green concept technologies that may work together to produce a greater cumulative effect.

### 3. Green Environment: Smart Energy Grid Concept

Largely, on-site renewable energy generation and utilization is recommended in formulating a green ambient. But making a large geography green, in essence would require smart and intelligent power generation, transmission, distribution and utilization efforts. Relevant distributed energy resources technology covers application areas of integration of distributed energy resources and their innovative aggregation mechanisms for participation in the electric system operation. Distributed energy resources for integration encompass distributed generation (including renewable generation such as those derived from solar and local wind sources, and non-renewable, energy-efficient generation resources on or near the loads), storage (including advanced battery-based and non-battery-based storage devices), and demand-side resources (such as smart appliances, electric vehicles (EVs) or plugin hybrid electric vehicles (PHEVs), and electricity-using equipment in industrial or commercial applications engaging in smart grid functions). Smart grid metrics for the technology application areas are:

- Load participating based on grid conditions: fraction of load served by interruptible loads, utility-directed load control, and incentive-based, consumer-directed load control;
- Load served by microgrids: fraction of entire load served by microgrids;
- Grid-connected distributed generation (renewable and non-renewable) and storage: percentage of all generation capacity that is distributed generation and storage;
- EVs and PHEVs: percentage shares of on-road, light-duty vehicles comprised of EVs and PHEVs;
- Grid-responsive, non-generating, demand-side equipment: total load served by smart, grid-responsive equipment (smart appliances, industrial/commercial equipment including motors and drivers).

Considering the underlying transmission and distribution (T&D) infrastructure, technology application areas at the transmission level include substation automation, dynamic limits, relay coordination, and the associated sensing, communication, and coordinated action. Distribution-level application areas include distribution automation (such as feeder-load balancing, capacitor switching, and restoration), enhanced customer participation in demand response, outage management systems, voltage regulation, VAR (volt ampere reactive) control, geographic information systems, data management, and mobile workforce management, and improved power quality to meet the range of customer needs. Further, smart grid metrics for the

T&D technology application areas are: 1) T&D system reliability: duration and frequency of power outages; 2) automation: percentage of substations using automation; 3) advanced metering: percentage of total demand served by advanced metered customers; 4) advanced system measurement: percentage of substations possessing advanced measurement technology; 5) capacity factors: yearly average and peak-generation capacity factor generation and 6) T&D efficiencies: energy conversion efficiency of electricity generation, and electricity T&D efficiency.

Related to the above considerations, addressed in this paper are methods of decision-making in conserving the power/electrical energy toward green ambient creation.

### 4. Decision-Making in Power Conservation

A major issue in smart power grid management under green ambient is to make a prudent decision on exercising efficient power conservation. Pertinent to such issues, the decision has to be made among possible alternatives with all the certainty and uncertainty considerations duly taken into account. That is, decisions made are dictated by a prescribed set of decision criteria. Evolving such criteria and heuristically applying them to the problem is attempted in this paper with relevant examples.

Decision-making is a crucial aspect of any goal-oriented problem. It refers to making the best rational judgment with minimum risk. In engineering the power grid management, it involves prudent managerial steps of saving the energy by minimizing losses. Hence, relevant steps that are involved largely refer to engineering analyses on choosing the right efforts worthy of implementation. Further, this decision-making involves critical aspects of making judgment on the proper choice of equipment and systems (specified by the associated technological merits and engineering advantages) that lead to a tangible green ambient toward sustained energy conservation. In reality, it goes without saying that, decision-making involves both an optimal choice of engineering methods and a pragmatic selection of technology that matches the environment in hand. The engineering aspects of decision-making are aimed at deciding whether it is worthy of trying a particular method of taking into account of all the oddities of implications. Typically, such efforts are based on what is known as the *present worth analysis*. It refers to a decision-process on outcomes of feasible alternatives (with reference to a project proposal) with selection criterion being the extent of "green efficiency". The associated task of prudent decision among the alternatives involved is to foresee results with 1) a maximized result for a given (fixed) input; 2) a minimized input leading to a desired (fixed) output and 3) a maximized difference between the output and the input under the condition that neither the input nor the output is fixed. The corresponding *present worth* (PW) of a contemplated effort is decided on the basis of the life-span of the ambient (say, a green building) specified within a finite pe-

riod of time. This finite time-period is known as the *analysis period*. Within this analysis period, the useful life could be identical in respect of all the possible alternatives indicated for a green project; or, it could be different for each alternative. Another situation may correspond to the analysis period being of infinite extent. Adjunct to PW considerations, the other criteria on decision-making involve other factors, namely, *success rate of the project* and *eco-friendliness*.

#### 4.1 Statistical Decisions

Decision-making is often risky, difficult and complex. This is because such decisions may have to be made mostly with insufficient information. Lack of or sparse information is undesirable but often unavoidable. This condition of insufficient information depicts the “positive entropy” a measure of uncertainty. Such an uncertain state will lead to admitting that, different potential outcomes may be recognized without reasonable projections of their probability of occurrence. This admission portrays the implicit risk in the decision made thereof on the outcomes. *Risk* is the extent of variability among the outcomes associated with a particular strategy pursued in a business. It exists whenever, there is a range of possible outcomes that go with the decision and the statistics of such incomes are known (in terms of the probabilities of the outcomes). In general, efforts that offer higher expected results involve greater risk. Further, the risk is directly linked to the utility. That is, the utility function that measures the extent of satisfaction will respond to the extent of risk involved in a specific strategy pursued. If the utility function is plotted against the risk (for example, dollar expended on a project), there are three possible scenarios:

- 1) If the resulting plot is concave, the utility function is *risk-averse*;
- 2) A convex graph means that the utility function is *risk-seeking*;
- 3) A linear (straight) relation between the utility function versus the risk corresponds to a *risk-neutral* situation. Summarizing.

Further, whenever utility of an exercised effort is greater than the expected utility of the effort, the pursued strategy is risk-averse. When utility of effort exercised is equal to the expected utility of the effort, the pursued strategy is risk-neutral; and, when utility of effort exercised is less than the expected utility of the effort, the pursued strategy is risk-seeking.

#### 4.2 Risk management in Green Environment Efforts

Power utilities are responsible to defend and protect a critical infrastructure against any failure, however momentary. The utilities are also responsible for making prudent investments and focus on minimizing risk. Such responsibilities of the power utility operation can be comprehended via smart grid systems. An impediment, how-

ever, does exist to the widespread adoption of smart grid technology because smart grid technologies have not been extensively proven and the existing utility business model does not provide enough economic rewards for such cutting-edge utilities [1].

Still, many corporations have adopted the smart grid structures and such companies incorporating smart grid technologies have put a unique level of investment in a variety of technologies.

### 5. Decision-Making under Green Environment

A smart grid is an umbrella term that covers modernization of both the transmission and distribution grids. The modernization is directed at a disparate set of goals including facilitating greater competition between providers, enabling greater use of variable energy sources, establishing the automation and monitoring capabilities needed for bulk transmission at cross continent distances, and enabling the use of market forces to drive energy conservation.

Smart meters, one of the smart grid features, serve the energy efficiency goal. The approach is to make it possible for energy suppliers to charge variable electric rates so that charges would reflect the large differences in cost of generating electricity during peak or off peak periods. Such capabilities allow load control switches to control large energy consuming devices such as hot water heaters so that they consume electricity when it is cheaper to produce. That is, to reduce demand during the high cost peak usage periods, communications and metering technologies inform smart devices in the home and business when energy demand is high and track how much electricity is used and when it is used.

Intelligence in distribution grids will enable small producers to generate and sell electricity at the local level using alternative sources such as rooftop-mounted photo voltaic panels, small-scale wind turbines, and micro hydro generators. As such there could be several utilities competing at the local level [1].

By reducing peak demand, a smart-grid can reduce the need for additional transmission lines and power plants that would otherwise be needed to meet the demand [2]. The ability to reduce peak demand *via* smart grid-enabled consumer demand response/load management can defer or reduce the need to build resources that would be unused most of the time. A smart-grid can also defer capital investments by prolonging the life of existing assets through enhanced asset management methodologies that exploit additional condition monitoring and diagnostic information about system components. Thus there are economic benefits to utilities to embrace the smart-grid, and it follows a competitive power utility market will develop from its adoption.

In competitive technology situations, two or more de-

cision-makers are involved. The theory of equality applies to presuming that each decision-maker of a competing technology vendor is as good, intelligent and rational as the decision-makers of other competing units. However, each decision-player is confronted with the odds of other decision-makers' ploys. Thus, the decision-makers are *players*, the conflicts they face are *games* and the rationale of their competition is referred to as the *game theory* [3]. To illustrate the buried concepts of the game theory, it is necessary first to define and explain certain terms of relevance:

*Strategies*: Alternative courses of action taken by game-players.

*Pure strategy*: A player adopting the same alternative at every play.

*Game of strategy*: A game with the best course of action for a player being dependent on what that player's adversaries can do.

*Optimum strategy*: Using one alternative or a mix of alternatives (that is, using different alternatives) for successive plays.

*Payoff matrix*: In two-person games, for example, the rows of the payoff matrix contain the outcomes for one player, and the columns contents of the columns carry the outcomes for the other player.

*Saddle-point*: A saddle-point is identified by an outcome, depicting both the smallest number in its row and the largest number in its column in the payoff matrix. Considering a hypothetical payoff matrix indicated in **Table 1**, its saddle-point can be identified as shown. Note that the table is constructed with reference to three alternatives A(I), A(II), and A(III) and corresponding identified states of nature N1, N2, N3, and N4.

*Value of the game*: It is the return from playing one game depicting the amount that a player nets from the ensuing outcome.

*Mixed strategy*: It is the policy pursued by the players in the absence of the saddle-point. That is, different alternatives are used for a fixed proportion of the plays, but the alternative employed for each play is a random choice from those available.

*Nash equilibrium*: It corresponds to a set of strategies such that none of the players can improve their payoff, given the strategies of the other players.

The success of using game theory largely stays with applying judicious logic consistent with practical impli-

**Table 1. Illustration of a saddle-point in a hypothetical payoff matrix**

	N1	N2	N3	N4
A(I)	(9)	10	11	12
A(II)	1	2	3	4
A(III)	5	6	7	8

(The saddle point (9) is the largest in its column and smallest in itsrow).

cations. The procedure involved includes: Assigning meaningful payoffs, solving the associated matrix, (which is usually large), handling multiple players and accounting for the possibilities of collusion, conciliation, irrationality of players, and nonconformance of traditional game theory principles.

In essence, the game theory applies to competitive decisions under uncertainty. It covers the following versions of game: 1) Zero-sum/two-person game where two opponents are presumed to have the same knowledge of outcomes; and, the winnings of one equates to the losses of the other. 2) Zero-sum/two-person optimal pure (or mixed strategy) that allows selecting a single course of action (or randomly mixed actions) constrained by a set of proportions maintained, leads to the calculation of the value of the game assuring minimum return; 3) Multiple player games and 4) Nonzero-sum games. The last two games are more involved to formulate and solve. However, they carry promising applications in the technoeconomic world.

The following examples pertinent to power utility service are indicated to illustrate the game theory applications and solving approaches. The first example refers to a two player/zero-sum case and the second example is concerned with two player/nonzero-sum problem.

### 5.1 Example 1: A Game-Theoretic Approach to Smart Grid Utility Pricing Issues

Supposed a power utility service provider (PSP) has extended new service in an area where it faces competition from an incumbent local producer (ILP). The PSP finds that the ILP's promotional strategy varies from reduced price/service charges (C1) of electricity during low demand periods, and promoting the promise of no disturbances in power quality and reliability (C2) by designing and deploying its own neighborhood electricity circuit controlled by on-off switches and protected by circuit breakers. In order to competitively attract customers, the PSP also comes out with a plan that comprises of:

- 1) The new service at a rate (I1) but for peak curtailment, hiked rates for electricity used above a predetermined amount;
- 2) deploying in-home displays of power usage (I2); or
- 3) offering the ability to accommodate alternative energy to attract customers who want to go green (I3).

The PSP and the ILP are equally competitive in their promotional efforts but differ in certain aspects of their technology-specified expertise. Taking these facts into account, the marketing department of the PSP has arrived at a payoff matrix depicting the percentage gain (or loss) in net revenue for the different outcomes under the service plans of PSP and ILP as shown in **Table 2**. Suppose it is required to determine the proportion of PSP's efforts (pertinent to I2 and I3) that can be pursued so as to get a advantageous edge on (PSP's) revenue by providing the

**Table 2. Payoff matrix on the service plans of the PSP and ILP in Example 1**

		ILP	
		C1	C2
PSP	I1	- 3 %	- 8 %
	I2	+ 2 %	- 6 %
	I3	- 1 %	+ 5 %

service plans under discussion.

**5.1.1 Solution to Example 1**

*Graphical method:* This method corresponds to entering the data from the payoff matrix with payoffs on the ordinates and mixed strategy on the abscissa. The vertical scale should be chosen such that, it must accommodate the entire range of payoffs involved; and, the horizontal scale extends from 0 to 1.

The subsequent steps are as follows:

1) Determination of the dominance and reduce the pay off matrix to (2 × N) size.

2) Graphical representation of the payoff. (The scales of the graph always represent the player with only two alternatives. The third alternative is removed as a result of dominance criterion). Illustrated in **Figure 1** is the graphical solution under consideration.

3) Determination of the fractional (proportioned) use of alternatives by PSP in a mixed strategy.

4) Evaluation of value of the game to the PSP.

The proportioned (mixed) use of I2 and I3 by PSP can be determined by knowing the coordinates of the point of intersection of the corresponding lines drawn on the graph (**Figure 1**). The coordinates can be either directly read off from the graph or by solving the simultaneous equations of the lines. The equations for the lines can be determined from the geometry as: For I3,  $[y + 6x = 5]$ ; and, for I2,  $[y - 8x = -6]$ . Hence solving them, the point of intersection is (11/14, 4/14). Suppose is the fractional use of I3 and 1) is the fractional use of I2. Now, consider the reduced payoff matrix shown in **Table 3**. In terms of  $\theta$ , it follows that,  $[(+2) \times \theta + (1 - \theta) \times (-1) \equiv 11/14 \equiv (-6 \times \theta + (1 - \theta) \times 5]$ , solving which yields  $\theta = 6/14$ . Hence,  $(1 - \theta) = 8/14$  as indicated on the reduced payoff matrix (Table 3). This leads to the conclusion that, the PSP should adopt 43 % effort on I2 strategy (deploying in-home displays of power usage) and 57% of effort on I3 strategy (ability to accommodate alternative energy).

If such a mixed proportion of efforts is exerted by the PSP, then what is its value of the game? This value refers to maximum advantage (gain) to the PSP, should the ILP follows optimum strategy. It is an *expected value*, EV (for PSP) and can be deduced (using the reduced payoff matrix indicated above) as follows:

$$EV(PSP) = [6/14 \times 11/14 \times (+ 2)] + [6/14 \times 3/14 \times (- 6)]$$

$$+ [8/14 \times 11/14 \times (- 1)] + [8/14 \times 11/14 \times (+ 5)] \cong 1.92 \%$$

The above calculation takes into account the mutually independent strategies of the PSP and the ILP and how their relative (proportionate) efforts weigh the percentages of payoff under possible alternatives are adopted.

Thus, by resorting to the mixed proportion of extending I2 and I3 strategies, the PSP is likely to gain a small revenue growth of about 1.92 % in the presence of the ILP adopting optimal strategy.

**5.2 Nonzero-Sum/Two-Person Game Problem**

The nonzero-sum game refers to situations in which all the game-players are either losers or winners in some respect or other. Typically, winning a war can be cited as an example, in which the reality is that nobody is a winner. The victor may apparently look like a winner, by taking the overall aspects of war; the victor suffers as much as the vanquished. Likewise, in a labor dispute that has been solved, both the workers and the management enjoy the fruit of victory in their own perspective of the gains resulted from bargaining. The game players in this case

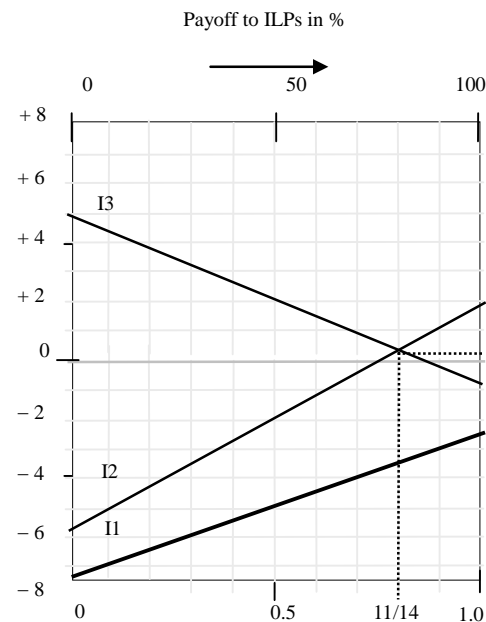


**Figure 1. Graphical solution to the problem. (I1-alternative is not taken into the solution as it has less dominance than the other alternatives)**

**Table 3. Reduced payoff matrix of Table 2**

		ILP		
		C1	C2	
PSP	I2	+2%	-6%	6/14
	I3	-1%	+5%	8/14
		11/14	3/14	

have implicitly colluded (against the consumers) so as to get something advantageous to themselves through bargaining. Such games are typically of nonzero strategies because any conciliatory measure accepted enforces one party to give up one or more of its alternative strategies in favor of the other.

The following example (Example 2) is presented to illustrate the underlying concepts. The nonzero problems in general, however, carry no unique solutions because of the unspecified chances of alternatives being given up by the game-players.

### 5.2.1 Example 2: A Non-Zero Sum Two-Person Game Problem

Cogeneration is the use of a heat engine or a power station to simultaneously generate both electricity and useful heat. Cogeneration captures the by-product heat for domestic or industrial heating purposes. It is most efficient when the heat can be used on site or very close to it. Overall efficiency is reduced when the heat must be transported over longer distances. Suppose an ILP employing smart-grid technology and a utility using cogeneration (CHP) are competing to extend power to industrial customers. The CHP is a competitor to the ILP and tries to attract industry by offering the following alternatives:

C1: Reduced rate based on contract length;

C2: Special discount for an industry agreeing that there will be high demand during peak time.

The ILP also attracts customers by offering the following alternatives:

I1: Special discount for industrial customers operating at night;

I2: Special discount for industries having distributed power available;

I3: ILP already has an existing smart-grid infrastructure for power access to serve some part of the service area in which the cogeneration company has no penetration yet due to technical reasons. I3 is intended to serve exclusively such areas.

Both ILP and the cogeneration utility (CHP) deploy advertisements on their services with equal competence. A market consultant presents the payoff matrix (shown in **Table 4**) on possible gains and losses for each possible outcome. The payoffs indicated represent the net change in revenue over a specific period resulting from competing promotional efforts of the competitors.

Suppose the *utility functions*  $u_C(P)$  and  $u_I(P)$  of the cogeneration-company (CHP) and the ILP *versus* the payoffs

**Table 4. Payoff matrix proposed by market consultant for the problem of Example 2**

		ILP		
		I1	I2	I3
CHP	C1	(-) \$ 1 M	\$ 0	(+) \$ 1 M
	C2	(+) \$ 4 M	(+) \$ 2 M	(-) \$ 3 M

(in millions of dollars) are expressed respectively by the following functional relations based on empirical market considerations:

$$u_C(P) = 0.1 \times P + 0.5$$

$$u_I(P) = -0.0082 \times P^2 - 0.0973 \times P + 0.6998 \quad (1)$$

It is interest to determine and discuss the revenue prospects and the related economy of the two competitors in reference to the services being marketed. Relevant pursuit is as follows:

### 5.2.2 Solution to Example 2

By converting monetary payoffs indicated above into “utility payoffs”, one can solve the associated problem. The underlying consideration is as follows: The CHP is relatively new and franchised to operate in the region under discussion. Its utility for the money can be assumed to directly proportional to the revenue earned or lost. On the contrary, the ILP extends across large regional boundaries but traditionally adopts a conservative management policy. Relevant utility function therefore, relies on the organizational policy and its attribution to one set of alternatives may not be the same for another set of alternatives.

Often, it is difficult to determine the utility index. It is a time-consuming and complex procedure that accounts for managerial perspective on a company’s aspiration level and expected standard of performance. It may involve some generous outlook to gain favor of customers as well as, may impose austerity measures to keep the losses a minimum. Small companies are flushed with ambition and carry the potentials of rapid growth, crash programs and diverse products and/or services. The major objective of management is to earn prestige and reputation so as to remain steady in the market (even at the expense of some tolerable losses). Its planning and engineering personnel will take the chance to play strategic games (or gamble!) in the competitive market. Larger companies, however, try to play the same game.

The utility function should be selected carefully lest the consequences of wrong and misconceived translation of payoff into utility index would lead to the company’s irreversible downfall. The readers may recall recent (1998-2001) IT-market scenario and compare the utility perspectives and market-attitudes of small start-up dot-com companies (with poured-in venture capitals) *versus* those of industries that had years of built-up infrastructure with large outlays that can be expressed in terms of their

**Table 5. Utility payoff matrices of Example 2**

		Relative utility payoffs of CHP			Relative utility payoffs of ILP		
		ILP			ILP		
		I1	I2	I3	I1	I2	I3
CHP	C1	0.4	0.5	0.6	0.8	0.7	0.6
	C2	0.9	0.7	0.2	0.2	0.5	0.9

prominent presence, huge capital (or share worthiness) and mammoth work-force values. Perhaps, there was over enthusiasm (or wrong horses played the wrong horse-play!) on the part of many dotcom industries in projecting utility functions, out-of-proportion to the payoffs involved.

In short, the *utility theory* governs the value that can be attached to an outcome for any alternative and a given future. That value can vary among individuals or from one business to the other. Utility is very much policy-specific and is therefore, ardently unique to any given business or industry. It is a response of the business enterprise to the anticipated risk in a competitive market environment judged from the payoff involved.

In this problem (Example 2), the utility *versus* payoff is specified in terms of utility functions,  $u_c(P)$  and  $u_i(P)$  of the cogeneration company and the ILP respectively as:  $[u_c(P) = 0.1 \times P + 0.5]$  and  $[u_i(P) = -0.0082 \times P^2 - 0.0973 \times P + 0.6998]$ . The payoff denotes the fact that the gain of one competitor is loss to the other for any given alternative. Correspondingly, the larger utility perceived by one competitor amounts to a lesser utility perceived by the competitor (for that alternative). The utility functions indicated in the problem reflects this consideration by having opposite slopes of the functional relations,  $u = f(P)$ .

Using the given utility functions, the payoff matrix can be translated into corresponding utility payoff matrices for the cogeneration-company and the ILP as shown in **Table 5**.

With the utility payoff data (as in **Table 5**), the next step is to construct the (utility) payoff graphs for the cogeneration CHP and the ILP as illustrated in **Figures 2(a)** and **2(b)** respectively. As indicated in Example 1, the dominance criterion allows I2 alternative not to be considered in the evaluation. Further, by solving the equations of the intersecting lines of I1 and I3, the coordinates of the points of intersection in the two graphs are determined (as indicated on **Figure 3**). These coordinate values can be interpreted as follows: Considering the utility payoffs for the cogeneration CHP, the company can expect an average (relative) utility payoff of about 0.51 by resorting to its strategy alternative C1, to an extent of about 78 % of its time and efforts. The next part of exercise is to determine the fractions of (I1 and I3) that can be inferred from the utility graphs of **Figure 2** as decided by the proportions of utility payoff percentages (C1 and C2) set along the *abscissa* of the graphs.

The results (obtained *via* the procedure indicated in Example 2) are tabulated in **Table 6** (in bold faces). These results indicate that, in pursuing the strategy of adopting C1 at 78%, the cogeneration CHP compromises about 0.67 of its value (of the game) be consumed by the ILP, (if the ILP chooses to use about 33% of its time and efforts towards I1 and about 67% towards I3).

Using the results as above, if the ILP decides to make use of maximum strategy for its own utility payoffs, the

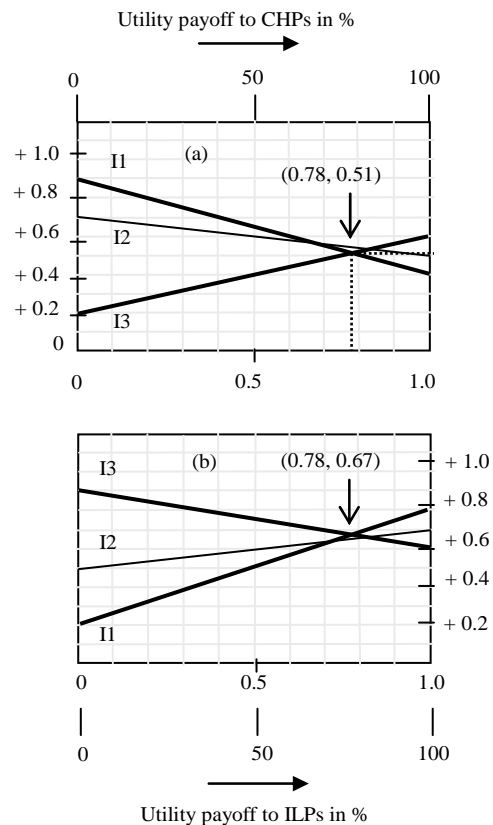


**Figure 2. Utility payoff graphs of: (a) CHP and (b) ILP**

value of the game, namely,  $EV_{(CHP)}$  for the cogeneration CHP will not alter. This would keep both companies pleased and can be verified by the following calculation:

$$EV_{(CHP)} = [0.78 \times 0.44 \times (0.4) + 0.78 \times 0.56 \times (0.6) + 0.22 \times 0.44 \times (0.9) + 0.22 \times 0.56 \times (0.2)] \approx 0.51 \tag{2}$$

Further, the cogeneration company (CHP) will benefit slightly by getting a cash-gain of about \$ 0.11 M in the game envisaged; and the ILP remains satisfied as a result of its high utility payoff (as implied by its utility function). Hence the strategies adopted by both sides would help maintain a *status quo* in the competitive market projected.

For mutually benefiting considerations in the competitive market, pursuance of certain other strategies that are based on compromising, collusive and conciliatory methods is possible. In maintaining the *status quo* as above, both companies may, however, find their approach expensive and difficult to manage. As such, the cogeneration CHP may wish to avoid competitive pursuit, if the ILP agrees to use 70% of its I2 alternative and 30 % of its I3 alternative in its implementations. Such an agreement will allow an average utility index of about,  $[0.70 \times 0.70 + 0.30 \times 0.20 =$

**Table 6. Relative utility payoffs of the CHP and the ILP in Example 2**

		ILP		ILP	
		I1	I3	I1	I3
CHP		<b>0.44</b>	<b>0.56</b>	<b>0.33</b>	<b>0.67</b>
	C1:	0.4	0.6	0.8	0.6
	C2:	0.9	0.2	0.2	0.9
		Relative utility payoff of CHP		Relative utility payoff of ILP	

0.55] for the cogeneration CHP; and, the corresponding utility index for the ILP will be,  $[0.7 \times 0.5 + 0.3 \times 0.9 = 0.62]$ . There is also a compromise solution in which both companies may get equal utility payoff. For example, the ILP can refrain from using its (I1 and I2) alternatives and at the same time the cogeneration CHP should agree to use only its C1 strategy. This will yield a compromising solution of identical utility payoffs (of index equal to 0.6) to both of them. Thus, there are several *ad hoc* solutions feasible in the game-theoretic approach for bargaining

dispositions when nonzero-sum situations are encountered.

## 6. Concluding Remarks

Thus, given a set of technology options, a payoff matrix strategy can be adopted to make right decisions as illustrated in the above examples. The problems indicated refer to a variety of constraints under which optimal payoff solutions are made via difference schemes of criteria-specifications.

## REFERENCES

- [1] "Smart Grid: Enabler of the New Energy Economy," Electricity Advisory Committee, December 2008. <http://www.oe.energy.gov/eac.htm>
- [2] D. Tuite, "For Power Design Opportunities, Try the Smart Grid," *Electronic Design*, Vol. 58, January 2010.
- [3] J. L. Riggs, "Engineering Economics," McGraw-hill Book Company, New York, 1977.

# A Qualitative Perspective on Idempotency Defect of Two Level System Interacting with Laser and Quantized Field

Sayed Abdel-Khalek<sup>1,2</sup>, Mohammed Mohammed Ali Ahmed<sup>1,4</sup>, Waleed Nabeel Razek<sup>3</sup>, Abdel Shafy Obada<sup>4</sup>

<sup>1</sup>Mathematics Department, Faculty of Science, Taif University, Taif, Saudi Arabia; <sup>2</sup>Department of Mathematics, Faculty of Science, Sohag University, Sohag, Egypt; <sup>3</sup>Mathematics Department, Physics Division, National Research Centre, Cairo, Egypt; <sup>4</sup>Mathematics Department, Faculty of Science, Al-Azher University, Nasser City, Cairo, Egypt.  
Email: abotalb2010@yahoo.com

Received March 22<sup>nd</sup>, 2010; revised May 13<sup>th</sup>, 2010; accepted May 13<sup>th</sup>, 2010.

## ABSTRACT

*Entanglement due to the interaction of a two level atom with a laser and quantized field is investigated. The role of the nonlinearity due to these interactions is discussed. It is found that the nonlinearity changes strongly the behavior of the entanglement also the detuning parameters have important role in the structure of the measure of entanglement.*

**Keywords:** Entanglement, Idempotency Defect, Two-Level System, Quantized

## 1. Introduction

Quantum information processing provides different way for manipulating information other than the classical one. This is related to entanglement, which plays an essential role in the quantum information such as quantum computing [1], teleportation [2], cryptography [3], dense coding [4] and entanglement swapping [5]. Thus intensive efforts have been done to understand theoretically and experimentally the entanglement in quantum systems. For instance, the entanglement between two qubits in an arbitrary pure state has been quantified by the concurrence [6] and Peres-Horodecki measure [7]. However, that of the mixed states is quantified by the average concurrence over all possible pure state ensemble decomposition. Additionally, the entropic relations are used in investigating the entanglement in quantum system. In this regard von Neumann entropy (NE) [8], linear entropy (LE) and the Shannon information entropy (SE) [9] have been frequently used in treating entanglement in the quantum systems. The NE [10] and the LE [11] have been applied to the JCM. It is worth mentioning that the SE involves only the diagonal elements of the density matrix and in some cases it can give information similar to that obtained from the NE and LE.

The paper is prepared in the following order: In Section 2 we define the system Hamiltonian. In Section 3, we derive the time evolution operator and density matrix. In

Section 4 we investigate the atomic inversion and idempotency defect (ID). In Section 5 we summarize the main results.

## 2. The System Hamiltonian

The scheme, we are going to discuss exploits the passage of a single atom through a quantized cavity [12]. We wish to underline the relevance of this aspect from an experimental point of view. Preparing and controlling a single atom is certainly much easier to achieve with respect to the case when the manipulation of many atoms is required. In addition, taking into consideration the low efficiency of the atomic state detectors today used in laboratory, conditional measurement procedures involving one atom only instead of many ones, have to be preferred. The dynamics of several Hamiltonian models describing such systems is exactly treatable and, in most cases, testable in the laboratory. The point to be appreciated is indeed that, studying such systems, one has the opportunity to induce entanglement and control its evolution in a multipartite physical system. In this paper: we study a two-level atom injected into a cavity field, where the dipole-allowed transitions between the lower level and the upper levels are nonresonant with the cavity mode. Furthermore, we assume that the interaction including an arbitrary form of nonlinearity of the intensity-dependent coupling. In the rotating wave approximation (RWA), the interaction of the cavity mode with the injected atom is

described by the Hamiltonian ( $\hbar = 1$ ):

$$H = H_A + H_F + H_{AF} + H_{AL}, \quad (1)$$

where  $H_A = \omega_0 S_z$  is the atom Hamiltonian,  $H_F = \omega_C \hat{a}^\dagger \hat{a}$  is the field Hamiltonian,  $H_{AF} = \frac{\xi}{2} (S_+ \hat{a} + \hat{a}^\dagger S_-)$  is the atom-field Hamiltonian, and

$$H_{AL} = \frac{r}{2} (S_+ e^{-i(\omega_L t + \psi_L)} + e^{i(\omega_L t + \psi_L)} S_-)$$

is the atom-laser Hamiltonian.

The atomic transition frequency is denoted by  $\omega_0$ , the frequencies of the cavity and laser fields are denoted by  $\omega_C$  and  $\omega_L$  respectively, and the laser field is assigned by the phase  $\psi_L$ , the operator  $\hat{a}$  ( $\hat{a}^\dagger$ ) is the annihilation (creation) operator of the cavity field and obey the commutation relation  $[\hat{a}, \hat{a}^\dagger] = 1$ ,  $\xi$  and  $r$  are the coupling constants associated with the cavity field and the classically described laser field respectively which are assumed real. The  $S$  operators are the coherence operators for the atom, satisfying the following angular momentum commutation relations  $[S_{ij}, S_{lm}] = S_{im} \delta_{jl} - S_{lj} \delta_{mi}$  where  $i, j, l, m = 1, 2, \dots$

### 3. Time Evolution Operator and Density Matrix

To obtain the time evolution operator, we must eliminate the explicit time dependence of the previous Hamiltonian (1), we use the following unitary operator [13]

$$T(t) = e^{-i(\omega_L t + \psi_L)(S_z + \hat{a}^\dagger \hat{a})}, \quad (2)$$

we redefine the Hamiltonian as :

$$H_1 = T^\dagger(t) H T(t) - iT^\dagger(t) \frac{dT^\dagger(t)}{dt}. \quad (3)$$

Then the Hamiltonian (1) will be in the following form:

$$H_1 = \Delta_C \hat{a}^\dagger \hat{a} + \Delta_L S_z + \frac{\xi}{2} (S_+ \hat{a} + \hat{a}^\dagger S_-) + \frac{r}{2} (S_+ + S_-), \quad (4)$$

where  $\Delta_C = \omega_C - \omega_l$  and  $\Delta_L = \omega_0 - \omega_l$ , if we consider the resonant pumping case  $\omega_0 = \omega_l$  and rearrange the Hamiltonian terms, the Hamiltonian (4) becomes.

$$H_1 = r S'_z + \Delta_C \hat{a}^\dagger \hat{a} + \frac{\xi}{2} (\hat{a}^+ + \hat{a}) S'_z + \frac{\xi}{2} (\hat{a} - \hat{a}^+) (S'_+ + S'_-) \quad (5)$$

The new atomic operators set

$$(S'_z = S_x, S'_+ = S_z + iS_y, S'_- = S_z - iS_y)$$

which obey the angular momentum commutation relations among themselves. The eigenvector of  $S'_z = S_x$  is the dressed states of the atom in the laser field alone and the operators  $S'_+$  and  $S'_-$  are the corresponding raising and

lowering operators.

To associate the third and the fourth terms of  $H_1$  we use the following unitary transformation:

$$\tilde{H} = P^\dagger H_1 P, \quad (6)$$

where  $P$  is an atomic state dependent displacement operator of the cavity field state which is defined as :

$$P = e^{\frac{\lambda}{2\Delta_C} (\hat{a} - \hat{a}^\dagger) S'_z} \quad (7)$$

Then the Hamiltonian (4) takes the following form:

$$\tilde{H} = r S'_z + \Delta_C \hat{a}^\dagger \hat{a} + \frac{\xi}{2} (\hat{a} - \hat{a}^+) (S'_+ v + S'_- v^+) - \frac{\lambda^2}{16\Delta_C}, \quad (8)$$

where

$$v = e^{\frac{\xi}{2\Delta_C} (\hat{a}^\dagger - \hat{a})} = e^{\frac{1}{2} \left( \frac{\xi}{2\Delta_C} \right)^2} \sum_{n=0}^{\infty} \sum_{m=0}^{\infty} \left( \frac{\xi}{2\Delta_C} \right)^{n+m} \frac{(-1)^n}{n!m!} \hat{a}^m \hat{a}^{\dagger n}. \quad (9)$$

We can drop  $\frac{\lambda^2}{16\Delta_C}$  which has no effect in the dynamics of the system.

This Hamiltonian describes a two level system with energy levels separated by  $r$  coupled to a single quantized mode of radiation frequency  $\Delta_C$  and there is an infinite sequence of probe resonance zones in the neighborhood of the Rabi sub harmonic resonances at

$$\Delta_C = \frac{\xi}{m}, m = \pm 1, \pm 2, \dots$$

If we consider of the RWA, the slowly varying terms are identified and retained, in the  $m$ th resonance zone  $S'_+$  has the zero order time dependence  $e^{-i\epsilon t}$  that is approximately canceled by the zero order time dependence  $e^{-i\frac{\Delta_C}{m} t}$  of all field operators of the form  $\hat{a}^{\dagger m} \hat{a}^{n+m}$ , for any  $n$ .

The Hamiltonian for the  $m$ th resonance zone is:

$$H_{eff} = \Delta_C \hat{a}^\dagger \hat{a} + r S'_z + \frac{\xi}{4} (S'_+ f_m + S'_- f_m^\dagger) \quad (10)$$

In this case, we recognize as the  $m$ th-order multiphoton Jaynes Cumming Hamiltonian where we consider

$$f_m = f(n) \hat{a}^m, \quad f(n) = e^{\left( \frac{\xi}{2\Delta_C} \right)^2} \sum_{\ell=0}^{\infty} \left( \frac{\xi}{2\Delta_C} \right)^{2\ell} \frac{(-1)^\ell}{(\ell!)^2} \hat{a}^\ell \hat{a}^{\dagger \ell}$$

destroys  $m$  photons of frequency  $\Delta_C$  where  $H_{eff}$  can be further simplified by means of another rotating wave approximation (RWA), (as discussed in detail in [12-14]).

The time evolution operator is given by:

$$U(t) = T(t) P e^{-iH_{eff} t} P^\dagger T^\dagger(t) = e^{-i\theta(\hat{a}^\dagger \hat{a})} \begin{bmatrix} U_{11} & U_{12} \\ U_{21} & U_{22} \end{bmatrix} e^{i\psi_L(\hat{a}^\dagger \hat{a})}, \quad (11)$$

$$\theta = (\omega_L t + \psi_L)$$

where

$$\begin{aligned}
U_{11} &= \frac{1}{2} e^{i(\psi_L - \theta)} (A + B + D + E), \\
U_{12} &= \frac{1}{2} e^{-i(\psi_L + \theta)} (A - B + D - E), \\
U_{21} &= \frac{1}{2} e^{i(\psi_L + \theta)} (A + B - D - E), \\
U_{22} &= \frac{1}{2} e^{-i(\psi_L - \theta)} (A - B - D + E),
\end{aligned} \quad (12)$$

and

$$\begin{aligned}
A &= G e^{-i\Delta_c \left(n + \frac{m}{2}\right)t} F_1(t) G^+, \\
B &= iG \xi e^{-i\Delta_c \left(n + \frac{m}{2}\right)t} f(m) E_1(t) G, \\
D &= iG \xi e^{-i\Delta_c \left(n - \frac{m}{2}\right)t} f(n) E_2(t) G^+, \\
E &= iG^+ \xi e^{-i\Delta_c \left(n - \frac{m}{2}\right)t} F_2(t) G,
\end{aligned} \quad (13)$$

where

$$F_j = \cos(\mu_j t) - i\delta \frac{\sin(\mu_j t)}{\mu_j}, E_j = -\frac{\sin(\mu_j t)}{\mu_j}, j = 1, 2.$$

Also,

$$\begin{aligned}
\mu_1(n) &= \frac{1}{4} \sqrt{16\delta^2 + (\lambda v_1(n))^2}, \\
\mu_2(n) &= \mu_1(n - m), v_1(n) = L_n^m(\xi^2) \sqrt{\frac{(n+k)!}{n!}},
\end{aligned}$$

where,  $v_2(n) = v_1(n - m)$ ,  $\delta = \frac{1}{2}(\varepsilon - m\Delta_c)$ ,  $G = v^2$  and  $L_n^m(\xi^2)$  is the Laguerre function. At  $t = 0$  the wave function of the system can be written as:

$$|\Psi(0)\rangle = \left[ \cos\left(\frac{\mathcal{G}}{2}\right) |e\rangle + \sin\left(\frac{\mathcal{G}}{2}\right) |g\rangle \right] |\alpha\rangle \quad (14)$$

where  $\mathcal{G}$  is the superposition state parameter

$$|\alpha\rangle = \sum_n \exp\left(-\frac{|\alpha|^2}{2}\right) \frac{\alpha^n}{\sqrt{n!}} |n\rangle, \quad (15)$$

with the mean photon number  $\bar{n} = |\alpha|^2$ , then the wave function at any time  $t > 0$  is given by

$$\begin{aligned}
|\Psi(t)\rangle &= U(t) |\Psi(0)\rangle \\
&= e^{-i(\omega_L + \psi_L)(\hat{a}^\dagger \hat{a})t} \{U_{12} |e, \alpha\rangle + U_{22} |g, \alpha\rangle\}
\end{aligned} \quad (16)$$

In the pure state case it is well known that the density matrix of the atom-field interaction can be written as:

$$\rho(t) = |\Psi(t)\rangle \langle \Psi(t)| \quad (17)$$

In order to analyze what happens to the two level sys-

tems interacting with laser and quantized field, we trace out field variables from the state  $\hat{\rho}(t)$  and get the reduced atomic density matrix of the system given by

$$\begin{aligned}
\rho_A(t) &= \text{tr}_F |\Psi_{AF}(t)\rangle \langle \Psi_{AF}(t)| \\
&= \sum_L \langle L | \rho | L \rangle = \rho_{ee}(t) |e\rangle \langle e| + \rho_{eg}(t) |e\rangle \langle g| \\
&\quad + \rho_{ge}(t) |g\rangle \langle e| + \rho_{gg}(t) |g\rangle \langle g|,
\end{aligned} \quad (18)$$

where

$$\begin{aligned}
\rho_{ee}(t) &= \langle n | e^{-i(\theta n - \psi_L)} U_{12} | \alpha \rangle \langle \alpha | U_{12}^+ e^{i(\theta n - \psi_L)} | n \rangle, \\
\rho_{eg}(t) &= \langle n | e^{-i(\theta n - \psi_L)} U_{12} | \alpha \rangle \langle \alpha | U_{22}^+ e^{i(\theta n - \psi_L)} | n \rangle, \\
\rho_{ge}(t) &= \langle n | e^{-i(\theta n - \psi_L)} U_{22} | \alpha \rangle \langle \alpha | U_{12}^+ e^{i(\theta n - \psi_L)} | n \rangle, \\
\rho_{gg}(t) &= \langle n | e^{-i(\theta n - \psi_L)} U_{22} | \alpha \rangle \langle \alpha | U_{11}^+ e^{i(\theta n - \psi_L)} | n \rangle.
\end{aligned} \quad (19)$$

#### 4. Atomic Inversion and Idempotency Defect

Atomic inversion can be considered as the simplest important quantity. It is defined as the difference between the probability of finding the atom in the excited state and in the ground state, the time dependent atomic inversion in the  $m^{\text{th}}$  resonance ( $\varepsilon = m\Delta_c$ ) is given by:

$$W(t) = \rho_{ee}(t) - \rho_{gg}(t) \quad (20)$$

Finally the idempotency defect as a measure of entanglement is written as:

$$\begin{aligned}
\varepsilon_t^{(j)} &= \text{Tr}_F \{ \rho(t)(1 - \rho(t)) \} \\
&= 1 - \text{Tr}_A (\rho(t))^2 \\
&= 2\rho_{ee}\rho_{gg} - 2|\rho_{eg}|^2
\end{aligned} \quad (21)$$

In many cases of quantum information processing, one requires a state with high purity and large amount of entanglement. Therefore, it is necessary to consider the purity of the state and its relation with entanglement.

Here we use the idempotency defect, defined by linear entropy, as a measure of the degree of purity for a state  $\rho(t)$ , in analogy to what is done for the calculation of the entanglement in terms of von Neumann entropy [15] which has similar behavior in the same cases.

[In all our figures we have plotted the atomic inversion  $W(t)$  and the entanglement ID  $\varepsilon_t^{(j)}$  as a function of the scaled time  $\xi t$  for the case of two-photon processes]. In **Figure 1**, we plot the atomic inversion and ID as a function of the scaled time. It is seen that, when we neglect the Laguerre function term, the atomic inversion shows fast Rabi oscillations, and the periodic behavior of the ID is seen. In this case the usual two-photon features are observed. Once the Laguerre term is considered the general

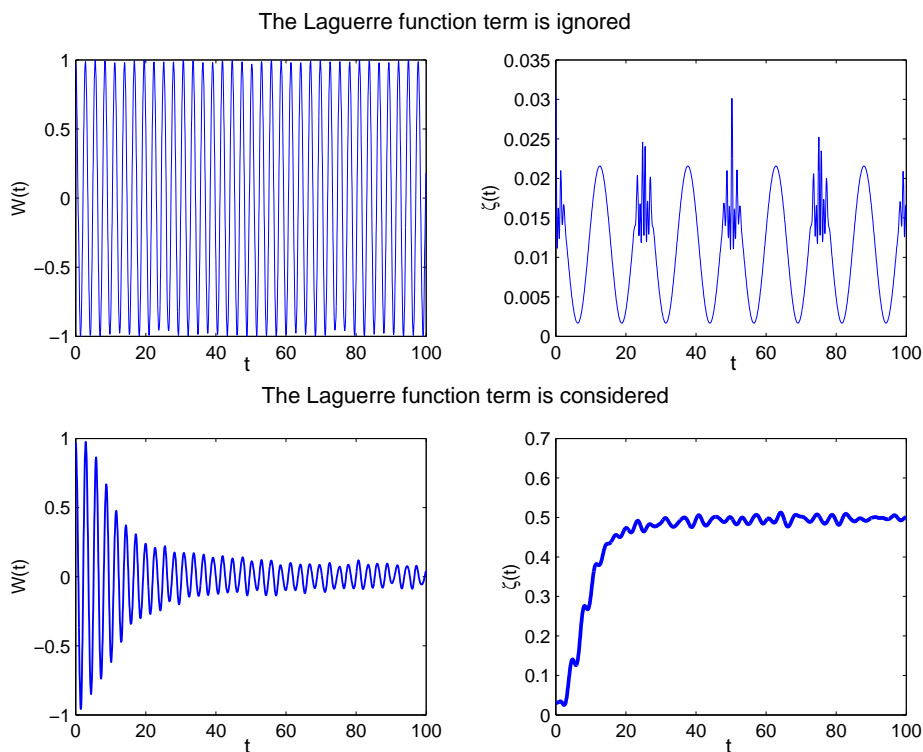


**Figure 1.** The evolution of the (a) atomic inversion and idempotency defect against the scaled time  $\tau t$  for the parameters  $\alpha = 5$ ,  $\xi = 0.5$ ,  $k = 2$  the laser detuning parameter  $\Delta_c = 1$ ,  $\theta = 0$  and  $\delta = 0$

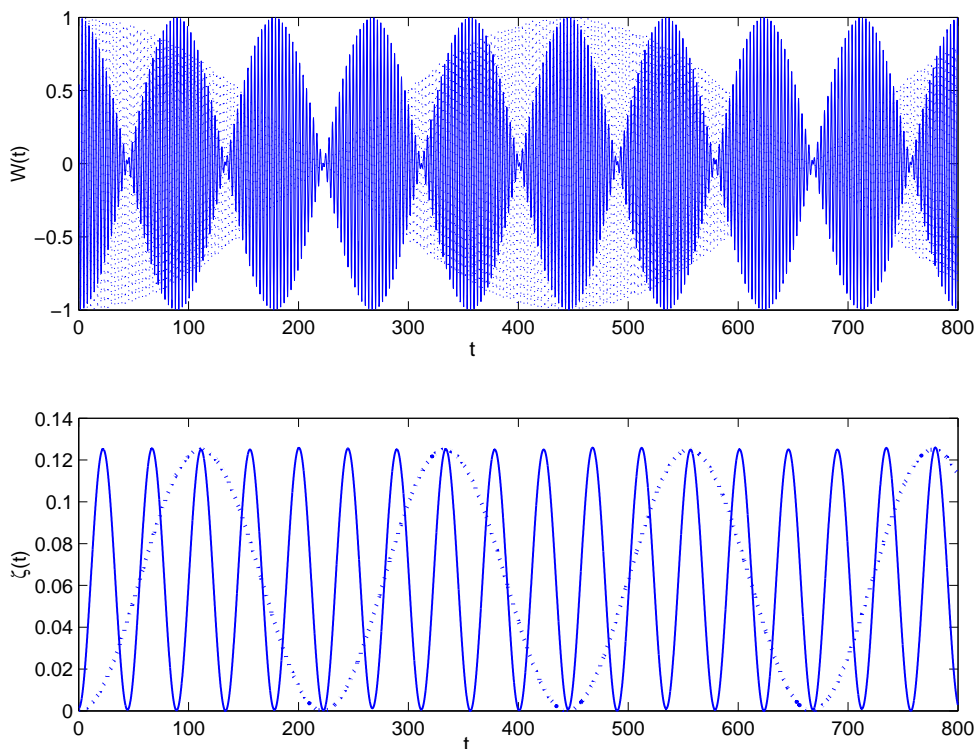


**Figure 2.** The evolution of the (a) atomic inversion and (b) idempotency defect against the scaled time  $\tau t$  for the parameters  $\alpha = 0$ ,  $\xi = 0.02$  (dotted line),  $\xi = 0.1$  (solid line),  $k = 2$  the laser detuning parameter  $\Delta_c = 1$ ,  $\theta = 0$  and  $\delta = 0$

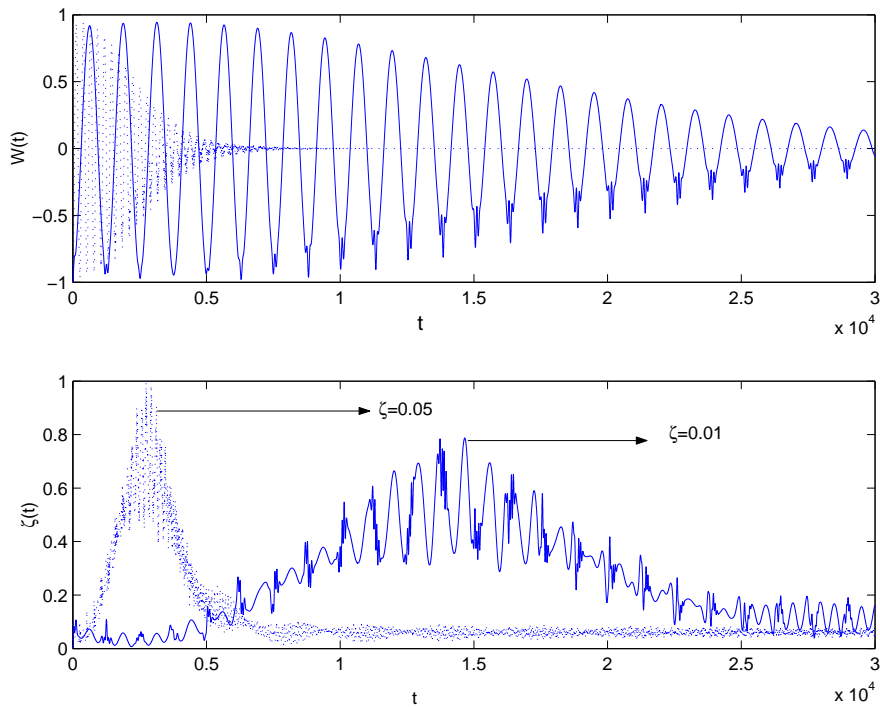


**Figure 3.** The evolution of the (a) atomic inversion and (b) idempotency defect against the scaled time for the parameters  $\alpha = \sqrt{10}$ ,  $\xi = 0.05$  (dotted line),  $\xi = 0.01$  (solid line),  $k = 2$  the laser detuning parameter  $\Delta_c = (2n - 0.5)\pi / t$ ,  $\theta = 0$  and  $\delta = 0$

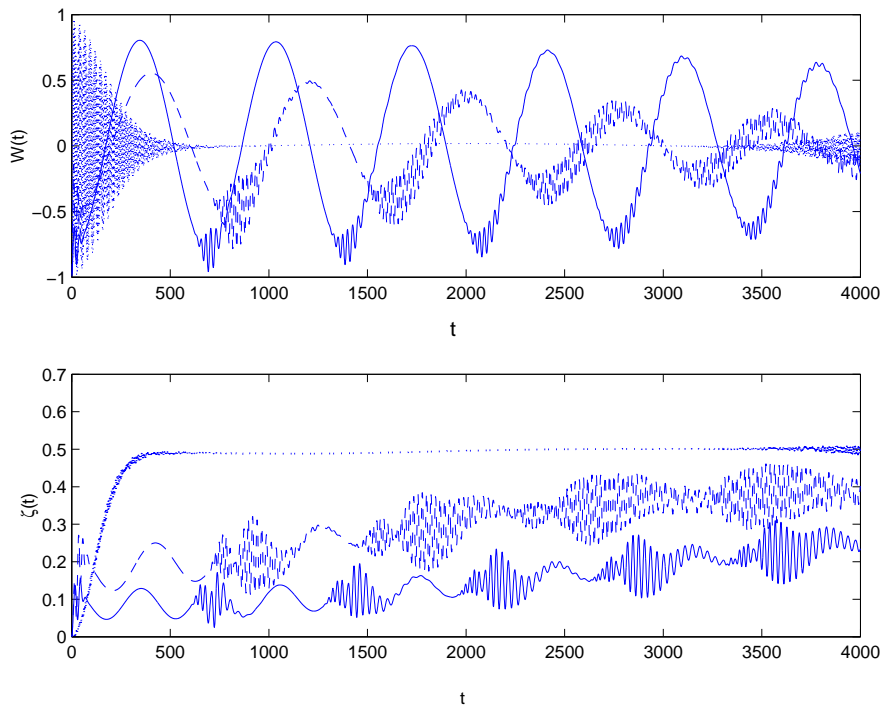


**Figure 4.** The evolution of the (a) atomic inversion and (b) idempotency defect against the scaled time  $rt$  for the parameters  $\alpha = \sqrt{10}$ ,  $k = 2$  the laser detuning parameter  $\Delta_c = 1$ ,  $\theta = 0$  and with different values of the detuning  $\delta = 0$  (solid line),  $\delta = 0.01$  (dashed line),  $\xi = 0.1$  (dotted line)

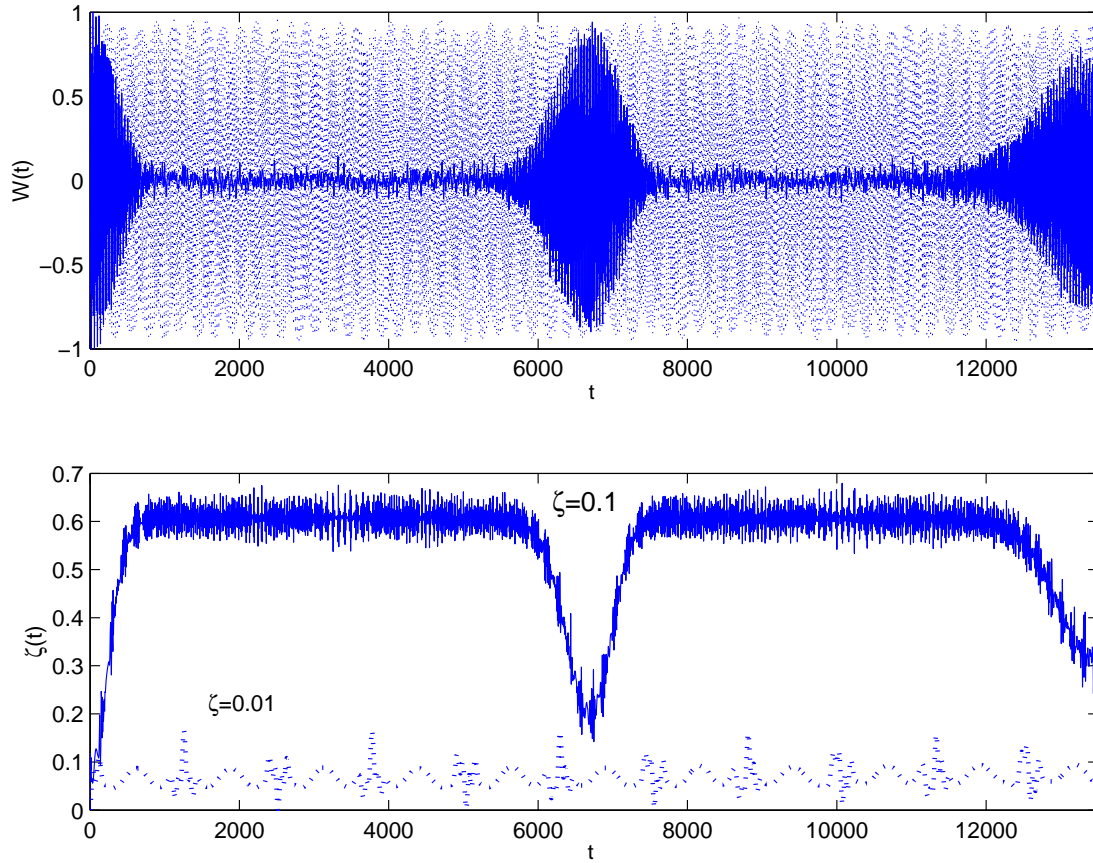


**Figure 5.** The evolution of the (a) Atomic inversion and (b) Idempotency defect against the scaled time,  $rt$  for the parameters  $\alpha = \sqrt{10}$ ,  $\xi = 0.01$  (dotted line),  $\xi = 0.1$  (solid line),  $k = 2$  the laser detuning parameter  $\Delta_c = 1$ ,  $\theta = 0$  and  $\delta = 0.1$

features of both the atomic inversion and ID are washed out, where as the time goes on the atomic inversion shows small amplitude of the oscillations and steady state of the ID (see **Figure 1**). As the time increases further the maximum entangled state can be obtained, where  $W(t) = 0 \Rightarrow \rho_{ee}(t) = \rho_{gg}(t)$  at this moment the entanglement reaches its maximum value. An interesting case is seemed in **Figure 2**, where we have considered small values of the parameter  $\xi$ . In this case the collapse-revival phenomenon is shown. Also, the periodic oscillation occurs each  $60\pi$  for atomic inversion and the zero ID at  $15\pi$  for  $\xi = 0.1$ .

Now we shed the some light on the affect of the different parameters on the both of the atomic inversion and the corresponding ID. For example the effect of the detuning  $\Delta_c$  is considered in **Figure 3**. In this case we see that the amplitude of the value of the detuning increased as the value of the detuning increased. The ID decreases and reaches steady state as  $\Delta_c$  increases further.

On the other hand, the detuning of the quantized field  $\delta$ , plays the opposite role, where the ID shows steady state at maximum instead of lowering its value due to the detuning of the laser field.

As  $\delta$  increases further (say  $\delta = 0.5$ ) we obtain a long

lived entanglement, as to show the fixed value of the ID ( $\xi = 0.5$ ). In **Figure 5**, we see that the collapse-revival phenomenon is clearly seen. Also, a perfect correspondence between the atomic inversion revival and the local maxima corresponds to the collapse periods. Also, we see that the collapse-revival phenomenon is clearly seen. Also, a perfect correspondence between the atomic inversion revival and the local maxima corresponds to the collapse periods. we have plotted the atomic inversion and the corresponding field Idempotency for a state of mean photon number of the coherent field as  $n = 10$ , fixed the detuning parameter  $\Delta_c = 1$  and the parameter  $\delta = 0$  and changed the parameter  $\xi$  with values (0.01 and 0.1), when  $\xi = 0.01$ , oscillated with period equal  $\xi t = 2000\pi$  and  $W(t)$  oscillated with same interval and  $\varepsilon_i^{(j)}$  has a long-lived entanglement in each interval. When  $\xi = 0.01$ , then  $\varepsilon_i^{(j)}$  has a weak oscillation and  $W(t)$  oscillated with a very small interval between maximum and minimum values.

## 5. Conclusions

In the present paper we show that the on idempotency defect can be used to quantify entanglement of a two level

system interacting with laser and quantized field. We obtain the long living entanglement due to the idempotency defects of the field. Our results show that the non-linearity changes strongly the behavior of the entanglement also the detuning parameters have important role in the structure of the measure of entanglement. Also, all the interaction parameters play an important role on the behavior of idempotency defect.

## REFERENCES

- [1] G. Benenti, G. Casati and G. Strini "Principles of Quantum Computation and Information, Vol. 1," *World Scientific*, 2004.
- [2] C. Bennet, G. Brassard, C. Crepeau, R. Jozsa, A. Peres and W. K. Wootters, "Teleporting an Unknown Quantum State via Dual Classical and Einstein-Podolsky-Rosen Channels," *Physical Review Letter*, Vol. 70, No. 13, 1993, pp. 1895-1899 .
- [3] A. Ekert, "Quantum Cryptography Based on Bell's Theorem," *Physical Review Letter*, Vol. 67, No. 6, 1991, pp. 661-663.
- [4] L. Ye and G.-C. Guo, "Scheme for Implementing Quantum Dense Coding in Cavity QED," *Physical Review Letter A*, Vol. 346, No. 5-6, 2005, pp. 330-336.
- [5] O. Glöckl, S. Lorenz, C. Marquardt, J. Heersink, M. Brownnutt, C. Silberhorn, Q. Pan, N. V. Looock, N. Korolkova and G. Leuchs, "Experiment towards Continuous-Variable Entanglement Swapping: Highly Correlated Four-Partite Quantum State," *Physical Review Letter A*, Vol. 68, No. 1, 2003, pp. 012319-012327.
- [6] W. K. Wootters, "Entanglement of Formation of an Arbitrary State of Two Qubits," *Physical Review Letter*, Vol. 80, No. 10, 1998, pp. 2245-2248.
- [7] A. Peres, "Separability Criterion for Density Matrices," *Physical Review Letter*, Vol. 77, No. 8, 1996, pp. 1413-14150.
- [8] J. von Neumann, "Mathematical Foundations of Quantum Mechanics," Princeton University Press, Princeton, 1955.
- [9] C. E. Shannon and W. Weaver, "The Mathematical Theory of Communication," Urbana University Press, Chicago, 1949.
- [10] S. J. D. Phoenix and P. L. Knight, "Fluctuations and Entropy in Models of Quantum Optical Resonance," *Annals of Physics*, Vol. 186, No. 2, pp. 381-407, 1988.
- [11] F. A. A. El-Orany and A.-S. Obada, "On the Evolution of Superposition of Squeezed Displaced Number States with the Multiphoton Jaynes-Cummings Model," *Journal of Optics B: Quantum Semiclass Optics*, Vol. 5, No. 1, 2003, pp. 60-72.
- [12] M. Lewenstein and T. W. Mossberg, "Spectral and Statistical Properties of Strongly Driven Atoms Coupled to Frequency-Dependent Photon Reservoirs," *Physical Review Letter A*, Vol. 37, No. 2048, 1988, pp. 2048-2062.
- [13] C. K. Law and J. H. Eberly, "Response of a Two-Level Atom to a Classical Field and a Quantized Cavity Field of Different Frequencies," *Physical Review Letter A*, Vol. 43, No. 11, 1991, pp. 6337-6344..
- [14] J. H. Eberly and V. D. Popov, "Phase-Dependent Pump-Probe Line-Shape Formulas," *Physical Review Letter A*, Vol. 37, No. 6, 1988, pp. 2012-2016.
- [15] G. M. A. Al-Kader and M. M. A. Ahmad, "On the Interaction of Two-Level Atoms with Squeezed Coherent State," *Chinese Journal of Physical*, Vol. 39, No. 1, 2001, pp. 50-63.
- [16] A. Ekert and P. L. Knight, "Entangled Quantum Systems and the Schmidt Decomposition," *American Journal of Physics*, Vol. 63, No. 5, 1994, pp. 415-423.

# Critical Factors that Affecting Efficiency of Solar Cells

Furkan Dinçer, Mehmet Emin Meral

University of Yuzuncu Yil, Department of Electrical and Electronics Engineering, Van, Turkey.  
Email: [furkandincer@yyu.edu.tr](mailto:furkandincer@yyu.edu.tr), [emeral@yyu.edu.tr](mailto:emeral@yyu.edu.tr)

Received February 17<sup>th</sup>, 2010; revised May 7<sup>th</sup>, 2010; accepted May 8<sup>th</sup>, 2010.

## ABSTRACT

*A solar cell or photovoltaic cell is a device which generates electricity directly from visible light. However, their efficiency is fairly low. So, the solar cell costs expensive according to other energy resources products. Several factors affect solar cell efficiency. This paper presents the most important factors that affecting efficiency of solar cells. These effects are cell temperature, MPPT (maximum power point tracking) and energy conversion efficiency. The changing of these factors improves solar cell efficiency for more reliable applications.*

**Keywords:** Solar Cell, Efficiency, Cell Factor, Cell Temperature

## 1. Introduction

Solar cells have seen remarkable improvements since the first issue of the journal Solar Energy Materials in 1979. The photovoltaic (PV) field has given rise to a global industry capable of producing many gigawatts (GW) of additional installed capacity per year [1].

The problems with energy supply and use are related not only to global warming but also to such environmental concerns as air pollution, acid precipitation, ozone depletion, forest destruction, and radioactive substance emissions. To prevent these effects, some potential solutions have evolved including energy conservation through improved energy efficiency, a reduction in fossil fuel use and an increase in environmentally friendly energy supplies. Among them, the power generation with solar cells system has received great attention in research because it appears to be one of the possible solutions to the environmental problem [2].

Solar Energy is energy that comes from the sun. The energy uses by solar cells that convert sunlight into direct current electricity. Solar cells are composed of various semi conducting materials. Semiconductors are materials, which become electrically conductive when supplied with light or heat, but which operate as insulators at low temperatures.

When photons of light fall on the cell, they transfer their energy to the charge carriers. The electric field across the junction separates photo-generated positive charge carriers (holes) from their negative counterpart (electrons). In this way an electrical current is extracted once the circuit

is closed on an external load.

Several factors affect solar cell efficiency. This paper examines the factors that affecting efficiency of solar cells according to scientific literature. These factors are changing of cell temperature, using the MPPT with solar cell and energy conversion efficiency for solar cell.

## 2. Characterization of Solar Cells

It is quite generally defined as the emergence of an electric voltage between two electrodes attached to a solid or liquid system upon shining light onto this system. Practically all photovoltaic devices incorporate a p-n junction in a semiconductor across which the photovoltage is developed. These devices are also known as solar cells. A cross-section through a typical solar cell is shown in **Figure 1**. The semiconductor material has to be able to absorb a large part of the solar spectrum. Dependent on the absorption properties of the material the light is absorbed in a region more or less close to the surface. When light quanta are absorbed, electron hole pairs are generated and if their recombination is prevented they can reach the junction where they are separated by an electric field [3].

The photoelectric effect was first noted by a French physicist, Edmund Becquerel, in 1839, who found that certain materials would produce small amounts of electric current when exposed to light [4,5]. The theory of the solar cell is the solar effect of semiconductor material. The solar effect is a phenomenon that the semiconductor material absorbs the solar energy, and then the electron-hole excited by the photon separates and produces electro-

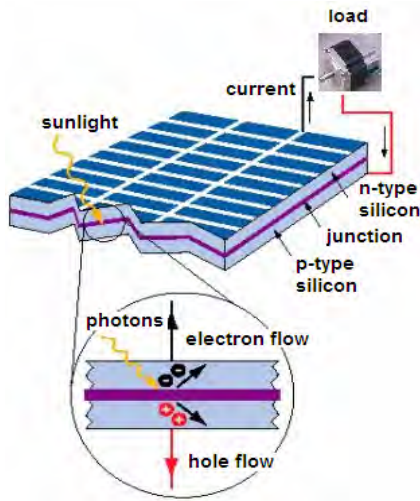


Figure 1. A schematic of the layers of a typical PV cell [4]

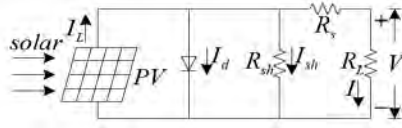


Figure 2. The equivalent circuit of the solar cell [6]

motive force. The  $I$ - $V$  characteristic of the solar cell changes with the sunshine intensity  $S(W/m^2)$  and cell temperature  $t$  ( $^{\circ}C$ ), that is  $I = f(V, S, t)$ . According to the theory of electronics, when the load is pure resistance, the actual equivalent circuit of the solar cell is as **Figure 2** [6].  $I_L$  is current supplied by solar cell.

$$I = I_L - I_0 \left[ \exp\left(\frac{q(V + IR_s)}{AkT}\right) - 1 \right] - \frac{V + IR_s}{R_{SH}} \quad (1)$$

where [6],  $I_d$ , the junction current of the diode

$$I_d = I_0 \left[ \exp\left(\frac{q(V + IR_s)}{AkT}\right) - 1 \right],$$

$I$ , the load current

$I_L$ , the photovoltaic current,

$I_0$ , the reverse saturation current

$q$ , electronic charge,

$k$ , boltzmann constant,

$T$ , absolute temperature,  $A$ , factor of the diode quality

$R_s$ , series resistance,

$R_{SH}$ , parallel resistance

Another important parameter is open circuit voltage  $V_{OC}$ ;

$$V_{OC} = \frac{kT}{q} \ln\left(\frac{I_L}{I_0} + 1\right) \approx \frac{kT}{q} \ln\left(\frac{I_L}{I_0}\right) \quad (2)$$

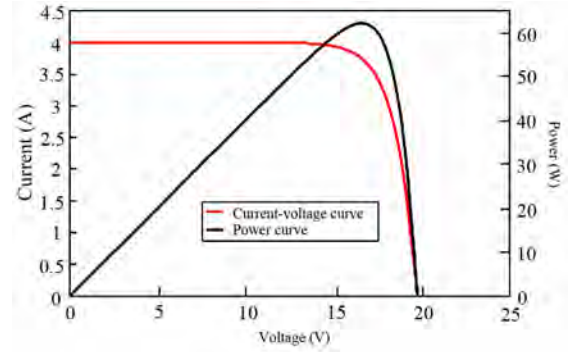


Figure 3. Typical I-V characteristic of a crystalline silicon module with the variation of power [7]

**Figure 3** shows an I-V characteristic together with the power curve, to illustrate the position of the maximum power point [7].

### 3. Solar Cells Efficiency Factors

#### 3.1 Cell Temperature

As temperature increases, the band gap of the intrinsic semiconductor shrinks, and the open circuit voltage ( $V_{OC}$ ) decreases following the p-n junction voltage temperature dependency of seen in the diode factor  $q/kT$ . Solar cells therefore have a negative temperature coefficient of  $V_{OC}$  ( $\beta$ ). Moreover, a lower output power results given the same photocurrent because the charge carriers are liberated at a lower potential. Using the convention introduced with the Fill Factor calculation, a reduction in  $V_{OC}$  results in a smaller theoretical maximum power  $P_{max} = I_{SC} \times V_{OC}$  given the same short-circuit current  $I_{SC}$  [8].

As temperature increases, again the band gap of the intrinsic semiconductor shrinks meaning more incident energy is absorbed because a greater percentage of the incident light has enough energy to raise charge carriers from the valence band to the conduction band. A larger photocurrent results; therefore,  $I_{sc}$  increases for a given insolation, and solar cells have a positive temperature coefficient of  $I_{SC}$  ( $\alpha$ ) [8].

**Figure 4** shows the I-V and P-V characteristics at the constant illumination when the temperature changes [9]. Temperature effects are the result of an inherent characteristic of crystalline silicon cell-based modules. They tend to produce higher voltage as the temperature drops and, conversely, to lose voltage in high temperatures. Any solar panel or system derating calculation must include adjustment for this temperature effect [10].

#### 3.2 Energy Conversion Efficiency

A solar cell's energy conversion efficiency ( $\eta$ , "eta"), is

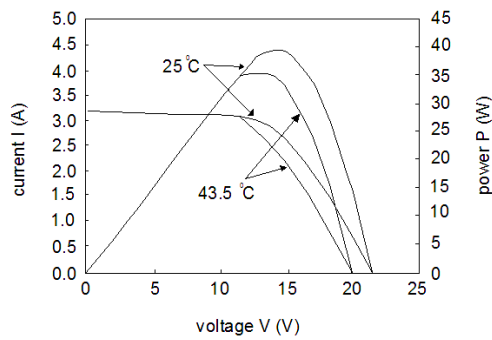


Figure 4. I-V and P-V characteristics of solar cell module [9]

the percentage of power converted (from absorbed light to electrical energy) and collected, when a solar cell is connected to an electrical circuit. This term is calculated using the ratio of the maximum power point,  $P_m$ , divided by the input light irradiance ( $E$ , in  $W/m^2$ ) under standard test conditions and the surface area of the solar cell ( $A_c$  in  $m^2$ ) [11].

$$\eta = \frac{P_m}{E \times A_c} \quad (3)$$

The efficiency of energy conversion is still low, thus requiring large areas for sufficient insulation and raising concern about unfavorable ratios of energies required for cell production versus energy collected [12]. In order to increase the energy conversion efficiency of the solar cell by reducing the reflection of incident light, two methods are widely used. One is reduction of the reflection of incident light with an antireflection coating, and the other is optical confinements of incident light with textured surfaces. They showed that the transformation of the wavelength of light could significantly enhance the spectral sensitivity of a silicon photodiode from the deep UV and through most of the visible region. [13].

The solar module has a different spectral response depending on the kind of the module. Therefore, the change of the spectral irradiance influences the solar power generation [14]. The solar spectrum can be approximated by a black body of 5900 K which results in a very broad spectrum ranging from the ultraviolet to the near infrared. A semiconductor, on the other hand can only convert photons with the energy of the band gap with good efficiency. Photons with lower energy are not absorbed and those with higher energy are reduced to gap energy by thermalization of the photo generated carriers. Therefore, the curve of efficiency versus band gap goes through a maximum as seen from Figure 5 [3].

### 3.3 Maximum Power Point Tracking

Currently, the electricity transformation efficiency of the solar cells is very low that reach about 14%. The efficiency of solar cells should be improved with various methods. One of them is maximum power point tracking

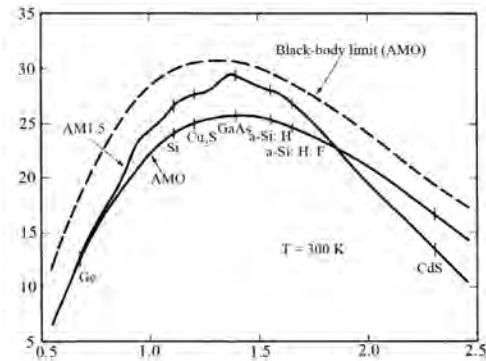


Figure 5. Dependency of the conversion efficiency on the semiconductor band gap [3]

(MPPT) which is an important method. The MPPT operates with DC to DC high efficiency converter that presents an optimal and suitable output power.

The resulting I-V characteristic is shown in Figure 5. The photo generated current  $I_L$  is equal to the current produced by the cell at short circuit ( $V = 0$ ). The open circuit Voltage  $V_{oc}$  (when  $I = 0$ ) can easily be obtained as [15].

No power is generated under short or open circuit. The maximum power P produced by the conversion device is reached at a point on the characteristic. This is shown graphically in Figure 6 where the position of the maximum power point represents the largest area of the rectangle shown. One usually defines the fill-factor  $ff$  by [15].

$$ff = \frac{P_{max}}{V_{oc} I_L} = \frac{V_m I_m}{V_{oc} I_L} \quad (4)$$

where,  $V_m$  and  $I_m$  are the voltage and current at the maximum power point.

When the output voltage of the photovoltaic cell array is very low, the output current changes little as the voltage changes, so the photovoltaic cell array is similar to the constant current source; when the Voltage is over a critical value and keeps rising, the current will fall sharply, now the photovoltaic cell array is similar to the constant volt-

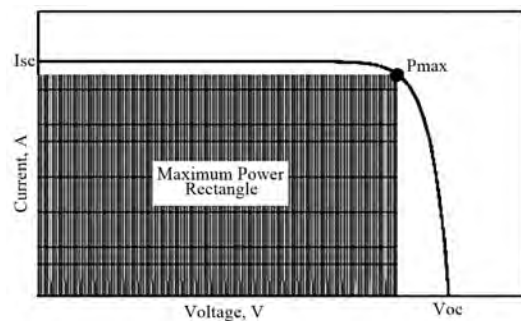


Figure 6. The I-V characteristic of an ideal solar cell [15]

age source. As the output voltage keeps rising, the output power has a maximum power point. The function of the maximum power tracker is to change the equivalent load take by the photovoltaic cell array, and adjust the working point of the photovoltaic cell array, in order that the photovoltaic cell array can work on the maximum power point when the temperature and radiant intensity are both changing [6].

#### 4. Conclusions

This paper examine factors that affecting efficiency of solar cells. These are changing of cell temperature, using the MPPT with solar cell and energy conversion efficiency for solar cell.

Temperature effects are the result of an inherent characteristic of solar cells. They tend to produce higher voltage as the temperature drops and, conversely, to lose voltage in high temperatures. The energy conversion efficiency is increased by reducing the reflection of incident light. The function of the maximum power tracker is to change the equivalent load take by the solar cell array, and adjust the working point of the array, in order to improve the efficiency.

Changing of these factors is very critical for solar cell efficiency. The optimum factors make it possible to get the great benefits of solar electricity at a much lower cost.

#### REFERENCES

- [1] "Reporting Solar Cell Efficiencies in Solar Energy Materials and Solar Cells," *Solar Energy Materials & Solar Cells*, Elsevier Science, 2008.
- [2] R.-J. Wai, W.-H. Wang and C.-Y. Lin, "High-Performance Stand-Alone Photovoltaic Generation System," *Proceedings of IEEE Transactions on Industrial Electronics*, Vol. 55, No. 1, January 2008.
- [3] A. Goetzberger, C. Hebling and H.-W. Schock, "Photovoltaic Materials, History, Status and Outlook," *Materials Science and Engineering*, Vol. 40, 2003, pp. 1-46.
- [4] February 2010. <http://www.rise.org.au/info/Education/SAPS/sps003.html>
- [5] February 2010. <http://science.nasa.gov/headlines/y2002/solarcells.html>
- [6] X.-J. Ma, J.-Y. Wu, Y.-D. Sun and S.-Q. Liu, "The Research on the Algorithm of Maximum Power Point Tracking in Photovoltaic Array of Solar Car," *Vehicle Power and Propulsion Conference, IEEE*, 2009, pp. 1379-1382.
- [7] N. M. Pearsall and R. Hill, "Photovoltaic Modules, Systems and Applications," In: M. D. Archer, and R. Hill, Eds., *Clean Electricity from Photovoltaics*, World Science, Vol. 1, 2002, pp. 1-42.
- [8] February 2010. [http://alumni.media.mit.edu/~nate/AES/PV\\_Theory\\_II.pdf](http://alumni.media.mit.edu/~nate/AES/PV_Theory_II.pdf)
- [9] Y. Suita and S. Tadakuma, "Driving Performances of Solar Energy Powered Vehicle with MPTC," *IEEE*, 2006.
- [10] February 2010. <http://www.altestore.com/howto/Solar-Power-Residential-Mobile-PV/Off-Grid-Solar-Systems/Electrical-Characteristics-of-Solar-Panels-PV-Modules/a87/>
- [11] February 2010. [http://en.wikipedia.org/wiki/Solar\\_cell](http://en.wikipedia.org/wiki/Solar_cell)
- [12] H. J. Queisser and J. H. Werner, "Principles and Technology of Photovoltaic Energy Conversion," *Solid-State and Integrated Circuit Technology*, October 1995, pp. 146-150.
- [13] T. Maruyama, Y. Shinyashiki and S. Osako, "Energy Conversion Efficiency of Solar Cells Coated with Fluorescent Coloring Agent," *Solar Energy Materials & Solar Cells*, Elsevier Science, 1998.
- [14] M. Nishihata, Y. Ishihara and T. Todaka, "Presumption of Solar Power Generation Corresponding to the Change of Solar Spectrum, Photovoltaic Energy Conversion," *Proceedings of the 2006 IEEE 4th World Conference*, Vol. 2, May 2006, pp. 2168-2171.
- [15] S. Capar, "Photovoltaic Power Generation for Polycrystalline Solar Cells and Turning Sunlight into Electricity Thesis," Engineering Physics, University of Gaziantep, July 2005.

# Development and Installation of High Pressure Boilers for Co-Generation Plant in Sugar Industries

Kolar Seenappa Venkatesh<sup>1</sup>, Aashis S. Roy<sup>2</sup>

<sup>1</sup>Institute of Sugar Technology, G.U.P.G. Center, Bidar, India; <sup>2</sup>Department of Materials Science, Gulbarga University, Gulbarga, Karnataka, India.

Email: venkateshgug@gmail.com

Received April 8<sup>th</sup>, 2010; revised May 8<sup>th</sup>, 2010; accepted May 9<sup>th</sup>, 2010.

## ABSTRACT

The sugar cane containing minimum 30% fiber was referred as bagasse and used the generation of power required for the operation of sugar mill. The bagasse is fired in the boiler for producing steam at high pressure, which is extracted through various single high capacity turbines and used in the process. The installation of high pressure boilers and high pressure turbo-generators has provision for the operation of co-generation plant during the off-season also that enhances the power generation from 9 MW to 23 MW. The annual monetary benefits achieved are Rs. 204.13 million and this was based on cost of power sold to the grid @ Rs 2.548 per unit, sugar season of 219 days and off season of 52 days. This required an investment of Rs 820.6 million. The investment had an attractive simple payback period of 48 months.

**Keywords:** High Pressure Boiler, Co-Generation Plant, Sugar Industries, Steam Turbine, Bagasse, Dc Drives.

## 1. Introduction

The Indian sugar industry by its inherent nature can generate surplus power, in contrast to the other industries, which are not only consumers as well as producer of energy. This is mainly due to the 30% of fiber content in the sugar cane used by the sugar mills. This fibre referred to as bagasse, has good fuel value and is used for generation of the energy required for the operation of sugar mill [1]. The bagasse is fired in the boiler for producing steam at high pressure, which is extracted through various back-pressure turbines and used in the process [2]. The simultaneous generation of steam and power commonly referred to as co-generation. Conventionally, the co-generation system was designed to cater to the in house requirements of the sugar mill only. The excess bagasse generated was sold to the outside market [3-5].

In the recent years, with the increasing power 'Demand Supply' gap the generation of power from excess bagasse was found to be attractive. This also offers an excellent opportunity for the sugar mills to generate additional revenue [6-9]. Co-generation option has been adopted in many of the sugar mills, which substantial additional revenue for the mills. This also contributes to serve the national cause in a small way, by bridging the 'Demand supply' gap [10,11].

A 5000 TCD sugar mill in Tamilnadu operating for about 200 days a year had the following equipments:

- Boilers – 2 numbers of 18 TPH, 12 ATA  
2 numbers of 29 TPH, 15 ATA  
1 number of 50 TPH, 15 ATA
- Turbines-1 number 2.5 MW  
1 number 2.0 MW  
1 number 1.5 MW
- Mill drives – 6 numbers 750 BHP steam turbines  
1 number 900 BHP shredder turbine

The plant had an average steam consumption of 52 %. The power requirement of the plant during the sugar-season was met by the internal generation (**Figure 1**) and during the non-season from grid (**Figure 2**) [12,13].

In this paper, we have concentrated to develop and installation of co-generation plant during off-season using high pressure boilers and high pressure turbo-generators.

## 2. Experiment

The plant went in for a commercial co-generation plant. The old boilers and turbine were replaced with high-pressure boilers and a single high capacity turbine.

A provision was also made, for exporting the excess power generated, to the state grid. The mill steam turbines were replaced with DC drives. The details of the new

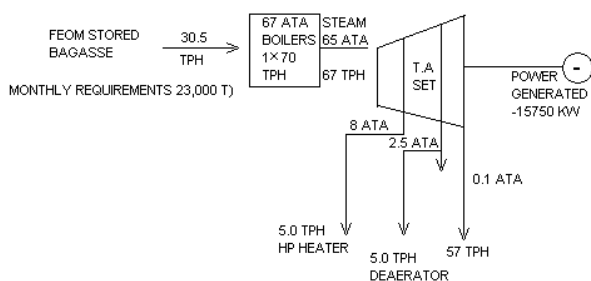


**Figure 1.** Shows that the energy flow diagram of non-sugar season

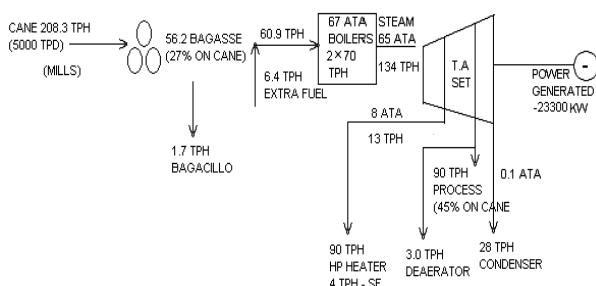


**Figure 2.** Shows that the energy flow diagram of sugar season

boilers, turbines and the steam distribution are as indicated below:

- Boilers – 2 numbers of 70 TPH, 67 ATA Multi fuel fired boilers.
- Turbines – 1 number of 30 MW turbo- alternator set (Extraction cum condensing type).
- Mill drives – 4 numbers of 900 HP DC motors for mills.

2 numbers of 750 HP DC motors for mills;

2 numbers of 1100 kW AC motors for fiber.

The two high capacities pressure boilers and a 30MW turbine were installed in place of the old boilers and smaller turbine. While selecting the turbo generator, it was decided to have the provision for operation of the co-generation plant, during the off-season also. This could be achieved by utilizing the surplus bagasse generated during the season, as well as by purchasing surplus bagasse from other sugar mills and biomass fuels such as groundnut shell, paddy husk, cane trash etc. The shortfall of bagasse during off-season was a problem initially. The purchase of biomass fuels from the nearby areas and the use of lignite solved this problem. The entire project was completed and commissioned in 30 months time.

### 3. Results and Discussions

The installation of high-pressure boilers and high-pressure turbo-generators has enhanced the power generation from 9 MW to 23 MW. Thus, surplus power of 14 MW is

available for exporting to the grid.

The following operating parameters were achieved:

- Typical (average) crushing rate = 5000 TCD;
- Typical power generation;
- During season = 5,18,231 units/day;
- During off season = 2,49,929 units/day;
- Typical power exported to the grid;
- During season = 3,18,892 units/day (13.29 MW/day);
- During off season = 1,97,625 units/ day (8.23 MW/day);
- Typical no. of days of operation = 219 days (season) = 52 days (off season).

The summary of the benefits achieved (expressed as value addition per ton of bagasse fired) is shown in below **Table 1**.

The efficient operation of a co-generation system depends on various factors. This has a direct bearing loss in power generation had the power exported to the grid.

Some of these critical factors affecting the power generation (quantified as loss in generation per day) are as follows:

- 1% drops in bagasse % in cane: 18300 units;
- 1% increase in moisture content in bagasse: 6800 – 10200 units;
- 1% increase in process steam consumption: 4200 units;
- 1% drops in crushing rate: 5000 – 7400 units;
- 1 hour downtime: 20600 units.

The above figures are based on the following operational parameters:

**Table 1.** The details of benefits achieved after implementation of high pressure boiler system

Parameter	Units	Previous status (low pressure boiler system)	Present status (high pressure boiler system)
Bagasse quantity	TPH	1.0	1.0
Steam quantity	TPH	2.1	2.2
Steam pressure	ATA	14	67
Power generation	kW	158	382
Extra power generated	kW	-	224
Steam quantity available for process	TPH	2.1	2.2
Steam pressure available for process	ATA	1.6	2.5
Steam on cane	%	52	45

- Crushing rate: 5000 TCD;
- Steam-bagasse ratio: 1: 2.2;
- NCV of bagasse (50% moisture): 1804 k Cal/Kg;
- Bagasse content in % cane: 27%.

#### 4. Conclusions

The annual monetary benefits achieved are Rs. 204.13 million (based on cost of power sold to the grid @ Rs 2.548 / unit, sugar season of 219 days and off season of 52 days). This required an investment of Rs 820.6 million. The investment had an attractive simple payback period of 48 months.

#### REFERENCES

- [1] P. S. Sankarnaraynan, J. G. Evans and C. Dampdarán, "Energy Efficiency in the Sugar Plant Steam and Power Generation," Avant-Garde, Engineers and Consultants Private Limited, Porur, Vol. 1, 2000, pp. 1-6.
- [2] A. Ataei, "Modification of Co-Generation Plant in a Sugar Cane Factory for Reduction of Power Deficit," *Research Journal of Environmental Science*, Vol. 3, 2009, pp. 619-630.
- [3] L. Lacrosse and S. K. Shakya, "Clean and Efficient Biomass Cogeneration Technology in Asean," *Power-Gen Asia Conference and Exhibition*, 2004, pp. 5-7.
- [4] C. Damodaran, N. Thirumoorthy and P. Parthasarthy, "Energy Audit in Sugar Industry," Avant-Garde, Engineers and Consultants Private Limited, Porur, Vol. 1, 2008, pp. 1-6.
- [5] R. H. Weed and M. L. Wisdom, "Condensate Considerations in the Development of High Pressure Co-Generation Facilities" BetzDearborn Inc., Trevose, 1998.
- [6] Idehara, "Indian Sugar Factories Cogeneration Design Review," Winrock International, Vol. 1, 2004, pp. 1-12
- [7] E. Worrell, R. van Berkel, F. Q. Zhou, C. Menke, R. Schaefer and R. O. Williams "Technology Transfer of Energy Science Technologies in Industry," *A Review of Trends and Policy Issues, Energy Policy*, Vol. 29, 2001, pp. 29-43.
- [8] E. D. Larson and R. H. Williams and M. R. L.V. Leal, "Energy for Sustainable Development," Vol. 1, 2001, p. 11.
- [9] "Consensus on Operating Practices for the Control of Feed Water and Boiler Water Chemistry in Modern Industrial Boilers," ASME, Vol. 1, 1998.
- [10] S. Dunn, "Re: Condensate Contamination Monitors," International Communication, BetzDearborn, 1997.
- [11] V. Kirubakaran., V. Sivaramakrishnan, R. Nalini, T. Sekar, M. Premalatha and P. Subramanian, "A Review on Gasification of Biomass," *Renew Sustain Energy Review*, Vol. 13, 2009, pp. 179-186.
- [12] M. Asadi, "Beet-Sugar Hand Book," First Edition, J. Wiley and Sons, Inc., Vol. 1, 2007.
- [13] B. W. Lamb and R. W. Bilger, "The Combustion of a Wet Cellulosic Fuel Bed," *Sugar Technology Review*, Vol. 4, No. 2, 1977, pp. 89-130.

# A MPCC-NLP Approach for an Electric Power Market Problem

Helena Sofia Rodrigues<sup>1</sup>, Maria Teresa Torres Monteiro<sup>2</sup>, António Ismael Freitas Vaz<sup>2</sup>

<sup>1</sup>School of Business Studies, Viana do Castelo Polytechnic Institute, Valença, Portugal; <sup>2</sup>Department of Production and Systems, University of Minho, Braga, Portugal

Email: sofia.rodrigues@esce.ipvc.pt, {tm, aivaz}@dps.uminho.pt

Received November 21<sup>st</sup>, 2009; revised May 14<sup>th</sup>, 2010; accepted May 14<sup>th</sup>, 2010.

## ABSTRACT

*The electric power market is changing-it has passed from a regulated market, where the government of each country had the control of prices, to a deregulated market economy. Each company competes in order to get more clients and maximize its profits. This market is represented by a Stackelberg game with two firms, leader and follower, and the leader anticipates the reaction of the follower. The problem is formulated as a Mathematical Program with Complementarity Constraints (MPCC). It is shown that the constraint qualifications usually assumed to prove convergence of standard algorithms fail to hold for MPCC. To circumvent this, a reformulation for a nonlinear problem (NLP) is proposed. Numerical tests using the NEOS server platform are presented.*

**Keywords:** Electric Power, Stackelberg Game, Nonlinear Programming, Complementarity Constrained Optimization

## 1. Introduction

The electric power market is in transition. Until recently, the market was regulated by the government of each country, and companies could only sell to a restrict set of consumers.

With the deregularization, electricity industry becomes a liberalized activity where planning and operation scheduling are independent activities which are not constrained by centralized procedures. On the other side, the generator firms take more risk as they become responsible for their decisions.

While in a regulated market the industry goal was to minimize the costs - once the price was fixed-now, it is also to maximize profit. A competition environment is created in order to benefit the consumers through price reduction, but ill effects can occur if the level of concentration in the market grows.

In order to study the interaction of all market participants and to have a better knowledge of the market conditions, firms and governments need suitable decision-support models. The deregularization process is under way in many countries. In 1998, the USA has begun their transition: California, Massachusetts and Rhode Island were the first states, but others will follow them over the next years. Nowadays, America's electric power industry is highly fragmented [1].

In Europe, the process has started in the decade of 80 in

England and Wales. In the last years, the market has been faced with fusions and merges between companies. The directives of European Union for an electric power liberality led up to increasing institutional and physical connections between markets from different countries. Some papers about studies in course, related with German, French and The Netherlands power markets-see [2-6] for more details-have emerged.

According to [7], there are reasons to consider electric power as a special commodity:

All power travels over the same set of power lines, independently of the firm that generated it; this difference is particularly marked when the networks contains loops and there are transmission capacity limits; also electricity has unique physical properties, namely Kirchhoff voltage and current laws.

As the electricity is difficult to store, and the quantity of power must be instantly adjusted to the demand, the companies that lead the market could easily manipulate the price, changing it to higher values, especially in peak consumption periods. The scientific community try to find models to predict how the prices will react to this new market structure.

The organization of this paper is as follows: Section 2 introduces the Stackelberg game and the related concepts and definitions of optimization. In Section 3, it is present the formulation of the electric power problem as well as its transformation from MPCC into a MPCC-NLP prob-

lem and also the data specifying the network for the computational experiments. Finally, the numerical results obtained by a set of solvers are shown and the main conclusions are discussed in the last section.

## 2. Stackelberg Game and Optimization

To simulate the decision making process for defining offered prices in a deregulated environment, it was used the game theory, in particular the Stackelberg game. A parallelism between this economic theory and optimization is also addressed.

### 2.1 Stackelberg Game

In Stackelberg game there are two kinds of players: the leader and the followers. The leader firm has the power to manipulate the prices, production and expansion capacity in order to maximize its own profit and anticipates the reaction of the rest of the player firms. The leader uses the knowledge of the reactions in order to choose its own optimal strategy. The follower decisions are dependent on the leader strategy. The follower does not have the perception how its decisions influence the leader resolution.

Between followers their behaviour act like a noncooperative Nash game, where all players have the same information and no one can increase their own profit through unilateral decisions [8].

A Stackelberg game can be formulated as a bilevel programming problem and therefore we introduce the reader to it in the next subsection.

### 2.2 Bilevel Optimization

#### Definition 1 Bilevel Optimization Problem

A bilevel optimization problem is composed by a first-level problem:

$$\begin{aligned} \min_{x,y} \quad & F_1(x,y) \\ \text{s.t.} \quad & g(x,y) \leq 0 \end{aligned} \quad (1)$$

Where  $y$ , for each value of  $x$ , is the solution of the second-level problem:

$$\begin{aligned} \min_y \quad & F_2(x,y) \\ \text{s.t.} \quad & h(x,y) \leq 0 \end{aligned} \quad (2)$$

with  $x \in \mathbb{R}^{n_x}$ ,  $y \in \mathbb{R}^{n_y}$ ,  $F_1, F_2 : \mathbb{R}^{n_x+n_y} \rightarrow \mathbb{R}$ ,  $g : \mathbb{R}^{n_x+n_y} \rightarrow \mathbb{R}^{m_g}$ ,  $h : \mathbb{R}^{n_x+n_y} \rightarrow \mathbb{R}^{m_h}$ .

The variables  $x[y]$  are called as first [second] level variable,  $g(x,y)$  [ $h(x,y)$ ] are the first [second] level constraints and  $F_1(x,y)$  [ $F_2(x,y)$ ] are the first [second] level objective function.

A typical bilevel problem is an optimization model whose constraints require that certain of its variables ( $x$ ) solve an optimization subproblem that depends parametrically on the remaining variables ( $y$ ).

Regarding with careful attention the structure of the

bilevel problem, it is possible to observe that the first/second level of the bilevel problem corresponds to the leader/followers players on the Stackelberg game.

A bilevel problem is convex if  $F_2$  and  $h$  are convex functions in  $y$  for all values of  $x$  that is to say if the second level problem is convex [9]. The problem studied in this paper is a convex bilevel problem. The great advantage of this property in bilevel optimization is that, under certain conditions, the second level problem can be replaced by their own Karush-Kuhn-Tucker (KKT) conditions, and the resulting problem is one level optimization problem with complementarity constraints.

### 2.3 Mathematical Program with Complementarity Constraints

#### Definition 2 MPCC Problem

Mathematical Program with Complementarity Constraint (MPCC) is defined as:

$$\begin{aligned} \min_z \quad & F(z) \\ \text{s.t.} \quad & c_i(z) = 0, \quad i \in E \\ & c_i(z) \geq 0, \quad i \in I \\ & 0 \leq z_1 \perp z_2 \geq 0 \end{aligned} \quad (3)$$

where  $z = (z_0, z_1, z_2)$ , with the control variable  $z_0 \in \mathbb{R}^n$  and the state  $z_1, z_2 \in \mathbb{R}^p$ ;  $F$  is the objective function,  $c_i, i \in E \cup I$  are the set of equality and inequality constraints, respectively. The sets  $E$  and  $I$  are the finite sets of indices. The objective function  $F$  and the constraints  $c_i, i \in E \cup I$  are assumed twice continuously differentiable. The constraints related to complementarity are defined with the operator  $\perp$  and demand that the product of the two nonnegative quantities must be zero, *i.e.*  $z_{1i}z_{2i} = 0, i \in \{1, \dots, p\}$ .

The concept of complementarity distinguishes an MPCC from a standard nonlinear optimization problem and is a synonymous of equilibrium, reason why this type of problem is so popular in optimization (see [8,10,11] for some applications in the last years).

In engineering, the MPCC problems are being used for contact and structural mechanic problems, namely in robotic [3,12,13], obstacle problems [14], elasto-hydrodynamic lubrication [15,16], process engineering models [17] and traffic network equilibrium [18,19].

Applications in economics include the general equilibrium and game theory from which Nash and Stackelberg game are instances [20-22].

A new field of applications is in ecological problems: the questions related with reduction of greenhouse gas emission rights, coalition formation and international trade in order to negotiate the emission rights between develop and developing countries can be also formulated

as a MPCC problem [23,24].

The MPCC problem is nonsmooth mostly due to the complementarity constraints. The optimal conditions are complex and very difficult to verify. Besides, the feasible set of MPCC is ill-posed since the constraint qualifications - namely, Mangasarian Fromovitz (MFCQ) and Linear Independent (LICQ)-which are commonly assumed to prove convergence of standard nonlinear programming do not hold at any feasible point of the complementarity constraints [25,26]. This implies mostly that the multiplier set is unbounded, the active constraint normal are linearly dependent and the linearizations of the MPCC can become inconsistent arbitrarily close to a solution.

The violation of constraint qualifications has led to a number of specific algorithms for MPCCs, such as branch-and-bound [27], implicit nonsmooth approaches [28], piecewise SQP methods [8] and perturbation and penalization approaches [29]. But the use of specific solvers for MPCC is not a real solution at this time, since these algorithms still need rather strong assumptions to ensure convergence.

The search of new techniques and algorithms in order to solve real problems with large dimension is still an area with intense research. Recently, some authors suggested solving MPCC problem by an interesting way: reformulated it into an equivalent NLP problem. This formulation allows taking advantage of certain NLP algorithms features in order to obtain rapid local convergence. Besides, it works like a challenge for the NLP solver, because it allows testing its reliability and robustness, whereas the MPCC problem has specific irregularities.

A MPCC defined in (3) can be reformulated as an equivalent NLP problem:

**Definition 3** *NLP formulation of the MPCC problem*

$$\begin{aligned} \min_z \quad & F(z) \\ & c_i(z) = 0, \quad i \in E \\ & c_i(z) \geq 0, \quad i \in I \\ \text{s.t.} \quad & z_1 \geq 0 \\ & z_2 \geq 0 \\ & z_1^T z_2 \leq 0 \end{aligned} \quad (4)$$

Recall that the complementarity constraint was replaced by a nonlinear inequality, relaxing the problem. The transformation from a MPCC problem into a NLP problem allows using standard NLP solvers taking to advantage of the convergence properties of these solvers.

One can easily show that the reformulated problem has the same properties that the previous one, including constraint qualifications and second-order conditions, which means that the violation of MFCQ is still a reality. However, in the last few years, some studies show that strong stationarity is equivalent to the KKT conditions of the

MPCC-NLP problem [30,31]. This fact has advantages because strong stationarity is a useful and practical computation characterization, once it is relatively easy to find a stationary point in a NLP solver, under reasonable assumptions.

### 3. The Electric Power Market Problem

The problem described in this paper is based on the model proposed in [32]. It is a competitive power market, formulated as an oligopolistic equilibrium model.

There are a number of generator firms, each owing a given number of units. These make an hourly bid to an Independent System Operator (ISO). The ISO, taking in consideration the network, solves a social welfare maximization problem, announces a dispatch for each bidder and possibly distinct prices at each node. It decides how much power to buy from generators and how much power to distribute to consumers and what prices to charge. All these decisions are made with the optimal power flow (OPF) in mind.

In spite of the fact that the ISO expects the bid to be a reflex of the true costs, the reality is different: the units, generally, increase their own bid, without the knowledge of the outside world, as the **Figure 1** shows. This strategy has as main goal the increase of the units' profit.

The leader generator first decides and takes as input all the perceptions and information that it could have about the market (including predictable bids of the other firms, demand and supply functions) and it maximizes its profit inside a set of spatial price equilibrium constraints and Kirchhoff's voltage and current laws. The followers firms make their own decisions taking into account the leader decision.

#### 3.1 Formulation

In [32] the electric power market was formulated as a bilevel problem. In the first level-the leader level-the parameter related with the bid curve corresponds to the first level variable. In the second level-the follower level - there is a simulation of the conjectures of the market promoted by ISO and can be described as a commodity spatial price equilibrium problem. The model tries to find the optimal bid for each company.

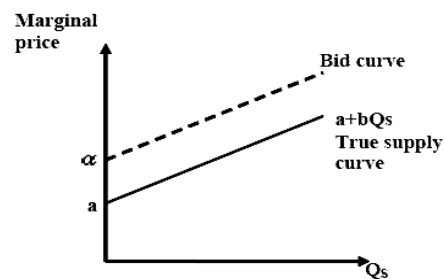


**Figure 1.** Marginal cost and bid curves.

Next we introduce the notation used in the mathematical formulation:

Indices:

$i$	node in the network
$ij$	arc from node $i$ to node $j$
$m$	number of Kirchhoff voltage loops in the network

Sets:

$N$	set of all nodes
$A$	set of all arcs
$S_f$	set of generator nodes under control of leader firm $f$
$P$	set of all generators nodes
$D$	set of all demand nodes
$L$	set of Kirchhoff' voltage loops $m$
$L_m$	set of ordered arcs (clockwise) associated with loop $m$

Recall that, a node can be, simultaneously a generator and a consumer, so  $P$  and  $D$  are not necessarily disjoint and their union could be a proper subset of  $N$ . The uniqueness of the net flow on each arc is ensured by the Kirchhoff's laws in the linearized DC models and, consequently, the number of (independent) loops is  $\#A - \#N + 1$  (where  $\#X$  is the set  $X$  cardinality).

Parameters:

$a_i, b_i$	intercept and slope of supply function (marginal cost) for the generator at node $i \in P$
$c_i, d_i$	intercept and slope of demand function for consumer at node $i \in D$
$\alpha_i, \bar{\alpha}_i$	upper bound of the bid for the unit at node $i \in S_f$
$\bar{Q}_{S_i}$	upper bound of production capacity for the unit at node $i \in P$
$\bar{T}_{ij}$	maximum transmission capacity on arc $ij \in A$
$r_{ij}$	reactance on arc $ij \in A$
$s_{ijm}$	$\pm 1$ corresponding to the orientation of the arc $ij \in A$ in loop $m \in L$ (+1 if $ij$ has the same orientation as the loop $m$ )

First-Level decision variable

$\alpha_i$	bid for the unit at node $i \in P$
------------	------------------------------------

In this model, it is assumed that the generate firms can only manipulate  $\alpha$  (the intercept in the bid function) and not the slope  $b$ , due to market and optimization assumptions.

Let  $\alpha_i$  be fixed for the competitive firms (*i.e.*  $\alpha_i$  fixed  $\forall i \in P \setminus S_f$ ) and variables for the leader firms (*i.e.*  $\alpha_i$  variable  $\forall i \in S_f$ ).

Primal variables in the second-level:

$Q_{S_i}$	vector defined by quantity of power generated by the unit at node $i$ ( $Q_{S_i} = a_i + b_i Q_{S_i}$ if $i \in P$ and $Q_{S_i} = 0$ if $i \notin P$ )
$Q_{D_i}$	quantity of power demanded at node $i$ ( $Q_{D_i} = c_i - d_i Q_{D_i}$ if $i \in D$ and $Q_{D_i} = 0$ if $i \notin D$ )
$T_{ij}$	matrix defined by MW transmitted from node $i$ to node $j$
Dual variables in the second-level	
$\lambda_i$	marginal cost at node $i$
$\mu_i$	marginal value of generation capacity for unit at node $i$
$\theta_{ij}$	marginal value of transmission capacity on arc $ij$
$\gamma_m$	shadow price for Kirchhoff voltage law for loop $m$

Next, it is defined the second-level convex quadratic problem. The objective function is related with the maximization of social welfare:

$$\max \sum_{i \in D} \left( c_i Q_{D_i} - \frac{1}{2} d_i Q_{D_i}^2 \right) - \sum_{i \in P} \left( \alpha_i Q_{S_i} + \frac{1}{2} b_i Q_{S_i}^2 \right) \quad (5)$$

This function reports a solution where the firms maximize their profits and the consumers maximize the utility of the product.

The following constraints report to a spatial price equilibrium plus a constraint due to Kirchhoff voltage law.

- Nonnegative demand variables:

$$Q_{D_i} \geq 0, \quad i \in D \quad (6)$$

- Lower and upper bounds for transmission variables:

$$0 \leq T_{ij} \leq \bar{T}_{ij}, \quad ij \in A \quad (7)$$

- Minimum and maximum capacity of production:

$$0 \leq Q_{S_i} \leq \bar{Q}_{S_i}, \quad i \in P \quad (8)$$

- Conservation constraints:

$$Q_{D_i} - Q_{S_i} + \sum_{j:ij \in A} T_{ij} - \sum_{j:ij \in A} \bar{T}_{ij} = 0 \quad (9)$$

- Kirchhoff voltage law:

$$\sum_{ij \in L_m} s_{ijm} r_{ij} T_{ij} = 0 \quad (10)$$

If in Equation (8), by economic reasons, the minimum production level could not be zero, it is possible to change the lower bound and still use the same model.

The description of the first level of the electric power is complete by taking into account that for the follower firms the bids are already fixed. The determination of the dominant company profit consists in finding a bid vector  $\alpha^f \equiv (\alpha_i : i \in S_f)$ , a vector of supplies  $Q_S$ , a vector of demands  $Q_D$  and a vector of transmission capacities  $T$ , by solving the following maximization problem.

$$\text{Maximize} \quad \pi(\lambda, Q) \equiv \left( \lambda Q - aQ - \frac{b}{2} Q \right) \quad (11)$$

$$s.t. \quad 0 \leq \alpha \leq \bar{\alpha}, \quad \forall i \in S$$

where  $Q_S$ ,  $Q_D$  and  $T$  for each value of  $\alpha \equiv (\alpha : i \in P)$ , are the solution of the second-level problem (5-10).

It is provided in [33] that, for each vector  $\alpha$ , there exists a unique globally optimal solution of the quadratic problem above.

But, solving a bilevel problem is not an easy task. So, the approach is to replace the ISO's lower-level optimization problem by its stationary conditions that results in a system of equilibrium constraints. To write the above information into a vector-matrix notation, it is necessary to introduce two additional matrices.

Let  $\Delta$  be the matrix which give us the information about the pair (node, arc) in the electric network:

$$\Delta_{il} = \begin{cases} 1, & \text{if } l = ij \in A \text{ for some } j \in N \\ -1, & \text{if } l = ij \in A \text{ for some } j \in N \\ 0, & \text{other values} \end{cases} \quad (12)$$

Let  $R$  be the matrix (arc, cycle) related with the reactance coefficients:

$$R_{ijm} = \begin{cases} s_{ijm} r_{ij}, & \text{if } ij \in L_m \\ 0, & \text{otherwise} \end{cases} \quad (13)$$

So, the Karush-Kuhn-Tucker (KKT) optimality conditions of the lower problem are:

$$\begin{aligned} 0 \leq \bar{Q}_S - Q_S & \perp & \mu & \geq 0 \\ 0 \leq Q_S & \perp & -\lambda + \mu + \alpha + \text{diag}(b)Q_S & \geq 0 \\ 0 \leq Q_D & \perp & \lambda - c + \alpha + \text{diag}(d)Q_D & \geq 0 \end{aligned} \quad (14)$$

$$\begin{aligned} 0 \leq \theta & \perp & \bar{T} - T & \geq 0 \\ 0 \leq T & \perp & \Delta^T \lambda + \theta + R\gamma & \geq 0 \\ \lambda \text{ free} & & Q_D - Q_S + \Delta T & = 0 \\ \gamma \text{ free} & & R^T T & = 0 \end{aligned} \quad (14)$$

where  $\mu$ ,  $\theta$ ,  $\lambda$  and  $\gamma$  are the dual variables. The notation  $\text{diag}(w)$  represents the diagonal matrix whose diagonal entries are the components of the vector  $w$ .

Then, the second-level problem (5-10) can be replaced by the KKT conditions (14) and the MPCC problem is obtained by joining (11) and (14).

For computational reasons the objective function needs to be reformulated, since it is neither convex nor concave due to the term  $\lambda_i Q_{S_i}$ . The equivalent objective function for solve the maximization of the leader firm profit is:

$$\begin{aligned} \pi_f(\lambda, Q_S) \equiv & \sum_{i \in D} (c_i Q_{D_i} - d_i Q_{D_i}^2) - \sum_{i \in S_f} \left( a_i Q_{S_i} - \frac{b_i}{2} Q_{S_i}^2 \right) \\ & - \sum_{ij \in A} \theta_{ij} \bar{T}_{ij} - \sum_{i \in P_i, S_f} (\mu_i \bar{Q}_{S_i} + a_i Q_{S_i} - b_i Q_{S_i}^2) \end{aligned} \quad (15)$$

### 3.2 Data

The electric power network includes a circuit with 30 nodes, which 6 are nodes with generators-3 for the leader firm A and the 3 remaining for the follower firm B-and 21 are demand nodes. Connecting the nodes there are 41 arcs and 12 loops. **Figure 2** shows a scheme that provides all the necessary information.

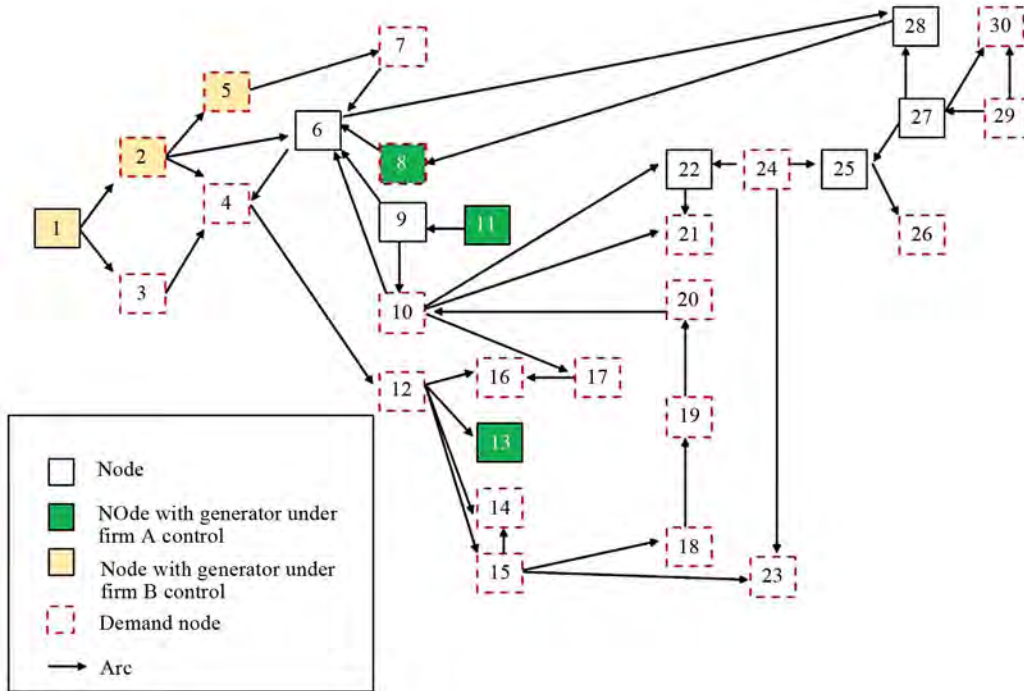


Figure 1. Electric Network

The data related with production, demand, transmission values are based on [7]. The generator cost function, reactance and upper bounds for supply and transmission flows values are also given. As a safety measure of the network the upper bounds values for the transmission capacity are 60% of the values assumed in [8].

To solve the dominant firm A problem it is assumed that the bids for the units of the company B are equals to their marginal costs, which means  $a = a$ .

The demand curve for each customer node is determined by  $P_i = 40 - d_i Q_{D_i}$  where  $d_i$  is chosen so that  $P_i = \$30/MWh$  when  $Q_{D_i}$  equals the value assumed in [34].

The code of this problem is in AMPL language and can be found in the MacMPEC [35] with the name *mon-teiro.mod*. It is a problem with 136 variables, 201 constraints where 62 of them are complementarity constraints.

To solve the problem, the MPCC-NLP approach was used, meaning that all complementarity constraints were reformulated as nonlinear constraints according the definition (4).

#### 4. Computational Results and Conclusions

To solve the electric power problem it were used three nonlinear solvers that have distinct characteristics.

Lancelot [36] is a standard Fortran 77 package for large scale nonlinear optimization, developed by Conn, Gould and Toint. The software uses an augmented Lagrangian approach and combines a trust region approach adapted to handle the bound constraints.

Loqo [37] was developed by Vanderbei and is a software for solving smooth constrained optimization problems. It is based on an infeasible primal-dual interior point

method applied to a sequence of quadratic approximations. It uses line search to induce global convergence and the Hessian is exact.

The Snopt, developed by Gill, Murray and Saunders, is a software package for solving large-scale linear and nonlinear programs. The functions used should be smooth but not necessary convex and it is especially effective for problems whose functions and gradients are expensive to evaluate.

The NEOS Server [38] platform was used to interface with the selected solvers. NEOS (Network Enabled Optimization System) is an optimization service that is available through the Internet. It is a large set of software packages considered as the state of the art in optimization.

The numerical results obtained by the used NLP solvers are presented in **Table 1** where the objective functions together with the first level variables are shown.

Curiously, although it has been reached an identical value for all solvers for the objective function, the same didn't happen for the bid variable, which take us to believe for the existence of the several local maximum points.

For the second-level variables the values are also different, as the **Tables 2** and **3** expose.

There are some demand nodes that practically do not receive electric power. This may be explained for two reasons: economical ones because it is possible that the transportation of the energy for these places are too expensive and by the existence of large demander nodes close to the generator units that absorbed all the power

**Table 1. Objective function and bid results**

Solver	Profit function ( $\pi$ )	Bid ( $\alpha^f$ )
LANCELOT	37.53	(35.83, 40, 29.80)
LOQO	37.53	(35.83, 36.09, 20)
SNOPT	37.53	(35.83, 39.99, 0)

**Table 2. Demanded power**

Node	Lancelot	Loqo	Snopt	Node	Lancelot	Loqo	Snopt
2	44.98	44.98	44.98	17	0	-1.37e-14	0
3	2.55	2.55	2.55	18	0	-4.54e-15	-2.28e-26
4	6.87	6.87	6.87	19	0	-4.55e-15	2.94e-13
5	41.04	41.04	41.04	20	0	-4.71e-15	-5.98e-26
7	0	-1.43e-14	0	21	0	0	0
8	10.01	10.01	10.01	23	0	-6.42	2.96e-13
10	0	-1.26e-14	8.08e-28	24	0	0	0
12	0	-1.41e-14	1.09	26	0	0	0
14	0	1.35e-14	0	29	0	0	0
15	0	-5.71e-15	-2.96e-13	30	0	0	0
16	1.32e-05	-4.32e-15	5.11e-13				

**Table 3. Generated power**

Node	1	2	5	8	11	13
Lancelot	44.30	10.09	41.04	10.01	1.29e-5	0
Loqo	44.31	10.09	41.04	10.01	1.60e-14	0
Snopt	44.31	10.09	41.04	10.01	-2-16e-13	0

produced.

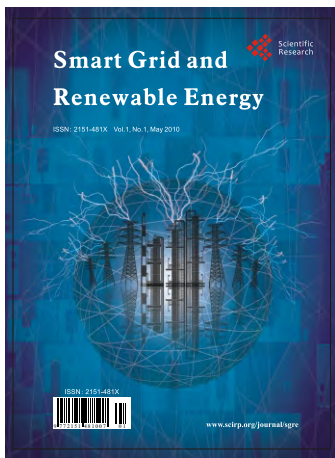
It has been shown that MPCC-NLP approach should be considered to solve real problems.

As future work it is proposed the study of this problem developed as a nash model, where both firms compete at the same level and with the same market information.

## REFERENCES

- [1] M. Willrich, "Electricity Transmission Policy for America: Enabling a Smart Grid, End to End," *The Electricity Journal*, Vol. 22, No. 10, 2009, pp. 77-82.
- [2] "Third Benchmarking Report on the Implementation of the Internal Electricity and Gas Markets," Tech Republic 1, Commission Draft Staff Paper, March 2004.
- [3] B. F. Hobbs and F. A. M. Rijkers, "Strategic Generation with Conjectured Transmission Price Responses in a Mixed Transmission Pricing System," *IEEE Transactions on Power Systems*, Vol. 19, No. 2, 2004, pp. 707-779.
- [4] Y. Smeers, "How Well Can Measure Market Power in Restructured Electricity Systems," Tech Republic, University Catholique De Louvain, November 2004.
- [5] S. A. Gabriel and F. U. Leuthold, "Solving Discretely-Constrained MPEC Problems with Applications in Electric Power Markets," *Energy Economics*, Vol. 32, No. 1, 2010, pp. 3-14.
- [6] M. Crappe, "Electric Power Systems," Wiley-ISTE, 2009.
- [7] C. B. Metzler, "Complementarity Models of Competitive Oligopolistic Electric Power Generation Markets," Master's Thesis, The Johns Hopkins University, 2000.
- [8] Z.-Q. Luo, J.-S. Pang and D. Ralph, "Mathematical Programs with Equilibrium Constraints," Cambridge University Press, Cambridge, 1996.
- [9] L. N. Vicente and P. H. Calamai, "Bilevel and Multilevel Programming: a Bibliography Review," *Journal of Global Optimization*, Vol. 5, No. 3, 1994, pp. 291-306.
- [10] S. Dempe, "Annotated Bibliography on Bilevel Programming and Mathematical Programs with Equilibrium Constraints," *Optimization*, Vol. 52, No. 3, 2003, pp. 333-359.
- [11] M. C. Ferris and J. S. Pang, "Engineering and Economic applications of Complementarity Problems," *SIAM Review*, Vol. 39, No. 4, 1997, pp. 669-713.
- [12] M. F. Ferris and F. Tin-Loi, "Limit Analysis of Frictional Block Assemblies as a Mathematical Program with Complementarity Constraints," *International Journal of Mechanical Sciences*, Vol. 43, No. 1, 2001, pp. 209-224.
- [13] J. S. Pang, "Complementarity Problems," In: R. Horst and P. Pardalos, Eds., *Handbook in Global Optimization*, K. A. Publishers, Boston, 1994.
- [14] J. F. Rodrigues, "Obstacle Problems in Mathematics Physics," Elsevier Publishing Company, Amsterdam, 1987.
- [15] M. C. Ferris and F. Tin-Loi, "On the Solution of a Minimum Weight Elastoplastic Problem Involving Displacement and Complementarity Constraints," *Computer Methods in Applied Mechanics and Engineering*, Vol. 174, No. 1-2, 1999, pp. 107-120.
- [16] K. P. Oh and P. K. Goenka, "The Elastohydrodynamic Solution of Journal Bearings under Dynamic Loading," *Transactions of American Society of Mechanical Engineers*, Vol. 107, No. 3, 1985, pp. 389-395.
- [17] A. U. Raghunathan and L. T. Biegler, "Mathematical Programs with Equilibrium Constraints (Mpecs) in Process Engineering," Tech Republic, CMU Chemical Engineering, November 2002.
- [18] O. Drissi-Kaitouni and J. Lundgren, "Bilevel Origin-Destination Matrix Estimation Using a Descent Approach," Tech Republic, Linköping Institute of Technology, Department of Mathematics, Sweden, 1992.
- [19] M. Stohr, "Nonsmooth Trust Region Methods and their Applications to Mathematical Programs with Equilibrium Constraints," Shaker Verlag, Aachen, 2000.
- [20] C. Ballard, D. Fullerton, J. B. Shoven and J. Whalley, "A General Equilibrium Model for Tax Policy Evaluation," National Bureau of Economic Research Monograph, Chicago, 1985.
- [21] H. Ehtamo and T. Raivio, "On Applied Nonlinear and Bilevel Programming for Pursuit-Evasion Games," *Journal of Optimization Theory and Applications*, Vol. 108, No. 1, 2001, pp. 65-96.
- [22] J. V. Outrata, "On Necessary Optimal Conditions for Stackelberg Problems," *Journal of Optimization Theory and Applications*, Vol. 76, No. 2, 1993, pp. 305-320.
- [23] J. C. Carbone, C. Helm and T. F. Rutherford, "Coalition formation and International Trade in Greenhouse Gas Emission Rights," MIMEO, *the Sixth Annual Conference on Global Economic Analysis*, Scheveningen, The Hague, The Netherlands, June 12-14 2003.
- [24] G. Hibino, M. Kainuma and Y. Matsuoka, "Two-Level Mathematical Programming for Analysing Subsidy Options to Reduce Greenhouse-Gas Emissions," Tech Republic, Laxenburg, 1996.
- [25] M. Kocvara and J. V. Outrata, "Optimization Problems with Equilibrium Constraints and their Numerical Solution," *Mathematical Programs, Series B*, Vol. 101, No. 1, 2004, pp. 119-149.
- [26] H. S. Rodrigues and M. T. Monteiro, "Solving Mathematical Program with Complementarity Constraints (MPCC) with Nonlinear Solvers," *Recent Advances in Optimization, Lectures Notes in Economics and Mathematical Systems*, Springer, Berlin, Part 4, 2006, pp. 415-424.
- [27] J. F. Bard, "Convex Two-Level Optimization," *Mathematical Programming*, Vol. 40, No. 1, 1988, pp. 15-27.
- [28] J. Outrata, M. Kocvara and J. Zowe, "Nonsmooth Approach to Optimization Problems with Equilibrium Constraints," Kluwer Academic Publishers, Dordrecht, 1998.
- [29] M. C. Ferris, S. P. Dirkse and A. Meeraus, "Mathematical Programs with Equilibrium Constraints: Automatic Reformulation and Solution via Constrained Optimization," Tech Republic, Oxford University Computing Laboratory, July 2002.
- [30] H. Scheel and S. Scholtes, "Mathematical Programs with

- Complementarity Constraints: Stationarity, Optimality and Sensitivity,” *Mathematics of Operations Research*, Vol. 25, No. 1, 2000, pp. 1-22.
- [31] S. Scholtes, “Convergence Properties of a Regularization Scheme for Mathematical Programs with Complementarity Constraints,” *SIAM Journal Optimization*, Vol. 11, No. 4, 2001, pp. 918-936.
- [32] B. F. Hobbs, C. B. Metzler and J.-S. Pang, “Strategic Gaming Analysis for Electric Power Systems: An MPEC Approach,” *IEEE Transactions on Power Systems*, Vol. 15, No. 2, 2000, pp. 638-645.
- [33] V. Krishna and V. C. Ramesh, “Intelligent agents in Negotiations in Market Games, Part 2: Application,” *IEEE Transactions on Power Systems*, Vol. 13, No. 3, 1998, pp. 1109-1114.
- [34] O. Als a and B. Scott, “Optimal Load Flow with Steady-State Security,” *IEEE Transactions on Power Systems*, Vol. 93, No. 3, 1973, pp. 745-751.
- [35] S. Leyffer, *Macmpec*, 2010. <http://www.mcs.nl.gov/leyffer/macmpec>
- [36] Lancelot, 2010. <http://www.numerical.rl.ac.uk/lancelot/blurb.html>
- [37] H. Benson, A. Sen, D. Shano and R. Vanderbei, “Interior-Point Algorithms Penalty Methods and Equilibrium Problems,” Tech Republic, Operations Research and Financial Engineering Princeton University, October 2003.
- [38] NEOS, 2010. <http://www-neos.mcs.ang.gov/neos>



## Call for Papers

# Smart Grid and Renewable Energy (SGRE)

ISSN 2151-481X (Print) ISSN 2151-4844 (Online)

<http://www.scirp.org/journal/sgre>

SGRE is an international refereed journal dedicated to the latest advancement of **Smart Grid and Renewable Energy**. The goal of this journal is to keep a record of the state-of-the-art research and promote the research work in these fast moving areas.

### Editors-in-Chief

**Prof. Yuanzhang Sun**  
**Prof. Victor Sreeram**

Wuhan University, China  
University of Western Australia, Australia

### Editorial Advisory Board

**Prof. Ryuichi Yokoyama**  
**Dr. Xiaoxin Zhou**  
**Dr. Yusheng Xue**  
**Prof. Qingquan Chen**

Tokyo Metropolitan University, Japan  
Chinese Society of Electrical Engineering, China  
State Power Corporation, China  
University of Hong Kong, China

### Editorial Board

- **Dr. Katerina Ioakeimidi**
- **Dr. Seongsoo Hong**
- **Dr. Gholam Hossein**
- **Dr. Herbert Iu**
- **Prof. Bouzid Mena**
- **Prof. Igor Yu. Denisyuk**
- **Dr. Pierluigi Siano**
- **Prof. Satyesh Chandra Roy**
- **Dr. Daniel Garrain**
- **Prof. Jaekeun Lee**
- **Prof. Bingru Yang**
- **Prof. Chunxiang Li**
- **Dr. Peter Simon Sapaty**
- **Prof. Maode Ma**
- **Prof. Igor I. Strakovsky**

Stanford University, USA  
Seoul National University, Korea (South)  
Research Institute for Astronomy and Astrophysics of Maragha, Iran  
The University of Western Australia, Australia  
Fluorotronics, Inc., USA  
Saint-Petersburg State University of Information Technologies, Russia  
University of Salerno, Italy  
Calcutta University, India  
Spanish Ministry of Science and Innovation, Spain  
Pusan National University, Korea (South)  
University of Science and Technology Beijing, China  
Shanghai University, China  
National Academy of Sciences of Ukraine, Ukraine  
Nanyang Technological University, Singapore  
The George Washington University, USA

### Subject Coverage

This journal invites original research and review papers that address the following issues in **Smart Grid and Renewable Energy**. Topics of interest include, but are not limited to:

- ★ Bio-energy technologies, process and utilization
- ★ Concept and structure frame of smart grid
- ★ Development of smart grid
- ★ Environmental-friendly technologies for power generation
- ★ Geothermal and tidal wave energy
- ★ Hydropower technologies and applications
- ★ Information and smart meter reading
- ★ Integrated energy and communications
- ★ New technologies and design for energy efficiency
- ★ New technologies for minimizing CO<sub>2</sub> generation
- ★ Photovoltaic for solar power applications
- ★ Power system analysis and optimization
- ★ Wind power generation and utilization

We are also interested in short papers (letters) that clearly address a specific problem, and short survey or position papers that sketch the results or problems on a specific topic. Authors of selected short papers would be invited to write a regular paper on the same topic for future issues of the **SGRE**.

### Notes for Intending Authors

Submitted papers should not have been previously published nor be currently under consideration for publication elsewhere. Paper submission will be handled electronically through the website. All papers are refereed through a peer review process. For more details about the submissions, please access the website.

### Website and E-Mail

<http://www.scirp.org/journal/sgre> E-mail: [sgre@scirp.org](mailto:sgre@scirp.org)

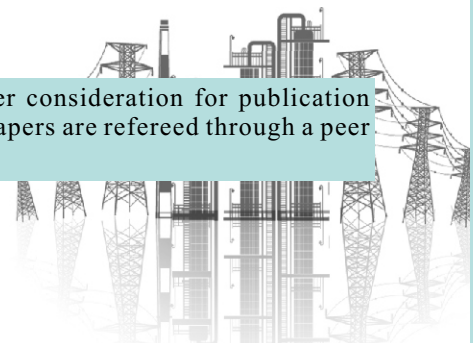


## TABLE OF CONTENTS

**Volume 1 Number 1**

**May 2010**

<b>Design of a Photo-Voltaic System to Enhance Network Dynamic Stability</b> G. J. Li, Y. Z. Sun, Q. Wang, S. S. Choi, S. Y. Ruan.....	1
<b>Control System Design of CSI Applied in the Battery Pack Testing System</b> L. X. Zhang, W. Kang, R. G. Wang.....	7
<b>Performance Analysis of Low Head Hydraulic Air Compressor</b> W. A. Aissa, S. Abdel-Hady, K. A. Ahmed.....	15
<b>Modeling of Work of Filling Granular Filter with Active Cooling</b> A. D. Rychkov.....	25
<b>Green Environment: Decision-Making and Power Utility Optimization towards Smart-Grid Options</b> D. DeGroff.....	32
<b>A Qualitative Perspective on Idempotency Defect of Two Level System Interacting with Laser and Quantized Field</b> S. Abdel-Khalek, M. M. A. Ahmed, W. N. A. Razeq, A. S. F. Obada.....	40
<b>Critical Factors that Affecting Efficiency of Solar Cells</b> F. Dinçer, M. Emin Meral.....	47
<b>Development and Installation of High Pressure Boilers for Co-Generation Plant in Sugar Industries</b> K. S. Venkatesh, A. S. Roy.....	51
<b>A MPCC-NLP Approach for an Electric Power Market Problem</b> H. S. Rodrigues, M. T. T. Monteiro, I. Vaz.....	54